



ISSN 1028-8546

Volume XVII, Number 3

Section: En

October, 2011

Azerbaijan Journal of Physics

Fizika

www.physics.gov.az



G.M. Abdullayev Institute of Physics
Azerbaijan National Academy of Sciences
Department of Physical, Mathematical and Technical Sciences

Azerbaijan Journal of Physics

Fizika

*G.M.Abdullayev Institute of Physics
Azerbaijan National Academy of Sciences
Department of Physical, Mathematical and Technical Sciences*

HONORARY EDITORS

Arif PASHAYEV

Mahmud KERIMOV

EDITORS-IN-CHIEF

Arif HASHIMOV
Chingiz QAJAR

SENIOR EDITOR

Talat MEHDIYEV

INTERNATIONAL REVIEW BOARD

Ivan Scherbakov, Russia
Kerim Allahverdiyev, Turkey
Mehmet Öndr Yetiş, Turkey
Gennadii Jablonskii, Buelorussia
Rafael Imamov, Russia
Vladimir Man'ko, Russia
Eldar Salayev, Azerbaijan
Dieter Hochheimer, USA
Victor L'vov, Israel
Vyacheslav Tuzlukov, South Korea
Majid Ebrahim-Zadeh, Spain

Firudin Hashimzadeh, Azerbaijan
Anatoly Boreysho, Russia
Mikhail Khalin, Russia
Hasan Bidadi, Tebriz, East Azerbaijan, Iran
Natiq Atakishiyev, Mexico
Maksud Aliyev, Azerbaijan
Bahram Askerov, Azerbaijan
Vali Huseynov, Azerbaijan
Javad Abidinov, Azerbaijan
Bagadur Tagiyev, Azerbaijan
Tayar Djafarov, Azerbaijan

Talat Mehdiyev, Azerbaijan
Nazim Mamedov, Azerbaijan
Emil Guseynov, Azerbaijan
Ayaz Bayramov, Azerbaijan
Tofiq Mammadov, Azerbaijan
Salima Mehdiyeva, Azerbaijan
Shakir Naqiyev, Azerbaijan
Rauf Guseynov, Azerbaijan
Almuk Abbasov, Azerbaijan
Yusif Asadov, Azerbaijan

TECHNICAL EDITORIAL BOARD

senior secretary Elmira Akhundova, Nazli Guseynova, Sakina Aliyeva,
Nigar Akhundova, Elshana Tarlanova

PUBLISHING OFFICE

33 H.Javid ave, AZ-1143, Baku
ANAS, G.M.Abdullayev Institute of Physics

Tel.: (99412) 439-51-63, 439-32-23
Fax: (99412) 447-04-56
E-mail: joph@physics.ab.az; jophphysics@gmail.com
Internet: www.physics.gov.az/index1.html

It is authorized for printing: 09.30.2011

Published at: **"ŞƏRQ-QƏRB "**
17 Ashug Alesger str., Baku
Typographer :Aziz Gulaliyev

Sent for printing on: __ 10.2011
Printing approved on: __ 10.2011
Physical binding: _____

Number of copies: _____200
Order: _____

SOLUTION OF GENERALIZATION OF PRINCIPAL CHIRAL FIELD PROBLEM

M.A. MUKHTAROV

*Institute of Mathematics and Mechanics
370602, Baku, F. Agayev str., 9, Azerbaijan*

New solutions of the principal chiral field problem with moving poles are constructed by means of MATHEMATICA software algorithm and discrete symmetry transformations for the algebra $SL(2, C)$.

Keywords: mathematica, algorithm, integrable model, group, chiral field.

PACS: 530.1:51-72

1. INTRODUCTION

Over the last few years self-dual Yang-Mills equation has attracted a fair amount of attention. It has been shown [1-8] that a large number of one, two and (1+2)-dimensional integrable models such as Korteweg-de Vries, N-waves, Ernst, Kadomtsev-Petviashvili, Toda lattice, nonlinear Schrodinger equations and many others can be obtained from the four-dimensional self-dual Yang-Mills equation by symmetry reduction and by imposing the constraints on Yang-Mills potentials.

The universality of the self-dual Yang-Mills (SDYM) model as an integrable system has been confirmed in the paper [9] where the general scheme of the reduction of the Belavin-Zakharov Lax pair for self-duality [10] has been represented over an arbitrary subgroup from the conformal group of transformations of R_4 -space. As the result of this reduction one has the Lax pair representation for the corresponding differential equations of a lower dimension.

The problem of constructing of the instanton solutions in the explicit form for semisimple Lie algebra, rank of which is greater than two, remains also important for the present time.

The method of integration of SDYM [11] is based on homogeneous Hilbert (Riemannian) problem (HHP) techniques. By means of the same method it was constructed the large class of solutions of the principal chiral field problem with moving poles (PCFMP) [12]. Being reduction of SDYM, the principal field model is investigated in [13] and solutions were obtained their by means of discrete symmetry transformations.

In the present paper we show how MATHEMATICA algorithm is effective in constructing of the solutions at every step of the procedure.

2. PRINCIPLE CHIRAL FIELD PROBLEM WITH MOVING POLES

The system of principle chiral field problem with moving poles

$$(\xi - \bar{\xi})f_{\xi\bar{\xi}} = [f_{\xi}, f_{\bar{\xi}}] \quad (2.1)$$

can be obtained from the system of self-duality equation

$$W_{z\bar{z}} + W_{y\bar{y}} + [W_z, W_y] = 0 \quad (2.2)$$

by means of substitution

$$\xi = r + it, \quad \bar{\xi} = -r + it,$$

$$r = \sqrt{y\bar{y} + \left(\frac{z - \bar{z}}{2}\right)^2},$$

$$it = \frac{z - \bar{z}}{2}$$

Here, the functions f, W take value in the corresponding semisimple algebra, sub-index denotes differentiation.

$$\text{Let } f = f^0 H + f^+ X^+ + f^- X^- ,$$

where H, X^{\pm} are generators of algebra A_1 ,

$$[X^+, X^-] = H, \quad [H, X^{\pm}] = \pm 2X^{\pm}.$$

Then the system (2.1) for the components f^0, f^{\pm} takes the following form

$$\begin{aligned} (\xi - \bar{\xi})f_{\xi\bar{\xi}}^+ &= 2(f_{\xi}^0 f_{\bar{\xi}}^+ - f_{\bar{\xi}}^0 f_{\xi}^+) \\ (\xi - \bar{\xi})f_{\xi\bar{\xi}}^0 &= f_{\xi}^+ f_{\bar{\xi}}^- - f_{\bar{\xi}}^+ f_{\xi}^- \\ (\xi - \bar{\xi})f_{\xi\bar{\xi}}^- &= -2(f_{\xi}^0 f_{\bar{\xi}}^- - f_{\bar{\xi}}^0 f_{\xi}^-) \end{aligned} \quad (2.3)$$

The discrete symmetry transformation in this case takes the form:

$$\begin{aligned}
 F^- &= \frac{I}{f^+} \\
 \frac{\partial F^0}{\partial \xi} &= (f^0 - F^0 + \xi) \frac{\partial \ln f^+}{\partial \xi} - \frac{\partial f^0}{\partial \xi} \\
 \frac{\partial F^0}{\partial \bar{\xi}} &= (f^0 - F^0 + \bar{\xi}) \frac{\partial \ln f^+}{\partial \bar{\xi}} - \frac{\partial f^0}{\partial \bar{\xi}} \\
 \frac{\partial F^+}{\partial \xi} &= (f^0 - F^0 + \xi)^2 \frac{\partial \ln f^+}{\partial \xi} - 2f^+ (f^0 - F^0 + \xi) \frac{\partial \ln f^0}{\partial \xi} - (f^+)^2 \frac{\partial f^-}{\partial \xi} \\
 \frac{\partial F^+}{\partial \bar{\xi}} &= (f^0 - F^0 + \bar{\xi})^2 \frac{\partial \ln f^+}{\partial \bar{\xi}} - 2f^+ (f^0 - F^0 + \bar{\xi}) \frac{\partial \ln f^0}{\partial \bar{\xi}} - (f^+)^2 \frac{\partial f^-}{\partial \bar{\xi}}
 \end{aligned} \tag{2.4}$$

These transformations imply that if $f = (f^+, f^0, f^-)$ is a solution of (2.3), then so is $F = (F^+, F^0, F^-)$.

Now we construct some exact solutions of the eq. (2.3).

Let the initial solution has the following form:

$f^- = 0$, $f^0 = \frac{p}{2}(\xi + \bar{\xi})$, f^+ where p is an arbitrary parameter.

From eqs.(2.3) for f^+ we have the following equation

$$(\xi - \bar{\xi})f_{\xi\bar{\xi}}^+ = p(f_{\xi\xi}^+ - f_{\xi\xi}^+) \tag{2.5}$$

For $p = -1$ the eq. (2.5) is equivalent to the Laplace equation

$$(\xi - \bar{\xi})f_{\xi\bar{\xi}}^+ = 0, \quad f^+ = \left(\frac{\xi - \bar{\xi}}{\varphi + \bar{\phi}} \right)^{-1}$$

where $\varphi, \bar{\phi}$ are arbitrary functions of independent variables $\xi, \bar{\xi}$ respectively.

Substituting f^+ into the formulas (2.4) and integrating we have

$$\begin{aligned}
 F^- &= \frac{\xi - \bar{\xi}}{\varphi + \bar{\phi}}, \quad F^0 = \frac{\xi - \bar{\xi}}{2} \frac{\varphi - \bar{\phi}}{\varphi + \bar{\phi}}, \\
 F^+ &= (\xi - \bar{\xi}) \frac{\varphi \bar{\phi}}{\varphi + \bar{\phi}}
 \end{aligned} \tag{2.6}$$

This solution coincides with solution (6) of [12] which is obtained by HHP.

For the $p = 1$ the eq. (4.5) is reduced to the Laplace equation on function ω defined by

$$\begin{aligned}
 \frac{f_{\xi}^+}{(\xi - \bar{\xi})^2} &= \omega_{\xi}, \quad \frac{f_{\bar{\xi}}^+}{(\xi - \bar{\xi})^2} = \omega_{\bar{\xi}}, \\
 [(\xi - \bar{\xi})\omega]_{\xi\bar{\xi}} &= 0, \quad \omega = \left(\frac{\xi - \bar{\xi}}{\varphi + \bar{\phi}} \right)^{-1}
 \end{aligned} \tag{2.7}$$

Integration of eq. (2.7) gives

$$f^+ = (\xi - \bar{\xi})(\varphi - \bar{\phi}) - 2 \int^{\xi} \varphi d\xi' - 2 \int^{\bar{\xi}} \varphi d\bar{\xi}'$$

For $p = \frac{1}{2}$ we have

$$\begin{aligned}
 f^+ &= \int_L C^+(\lambda) \sqrt{(\lambda - \xi)(\lambda - \bar{\xi})} d\lambda - \\
 &\quad - \int_L C^-(\lambda) / \sqrt{(\lambda - \xi)(\lambda - \bar{\xi})} d\lambda
 \end{aligned}$$

where $C^{\pm}(\lambda)$ are arbitrary functions of arguments λ in the complex plane, L represents an arbitrary circle. Elements F^{\pm} are defined by means of first order differential equations.

3. DISCRETE SYMMETRY TRANSFORMATION

Following Leznov [14], for the case of a semisimple Lie algebra and for an element f being a solution of (2.1), the following statement takes place:

There exists such an element S taking values in a gauge group that

$$\begin{aligned}
 S^{-1} \frac{\partial S}{\partial \xi} &= \frac{I}{\tilde{f}_-} \left[\frac{\partial \tilde{f}}{\partial \xi}, X_M \right] - \xi \frac{\partial}{\partial \xi} \frac{I}{\tilde{f}_-} X_M \\
 S^{-1} \frac{\partial S}{\partial \bar{\xi}} &= \frac{I}{\tilde{f}_-} \left[\frac{\partial \tilde{f}}{\partial \bar{\xi}}, X_M \right] + \bar{\xi} \frac{\partial}{\partial \bar{\xi}} \frac{I}{\tilde{f}_-} X_M
 \end{aligned} \tag{3.1}$$

Here X_N is the element of the algebra corresponding to its maximal root divided by its norm, i.e.,

$$[X_M^+, X^-] = H, [H, X^\pm] = \pm 2X^\pm, \quad ,$$

– \tilde{f}_- – is the coefficient function in the decomposition of \tilde{f} of the element corresponding to the minimal root of the algebra, $\tilde{f} = \sigma f \sigma^{-1}$ and where σ is an automorphism of the algebra, changing the positive and negative roots.

In the case of algebra $SL(2, \mathbb{C})$ we'll consider the case of three dimensional representation of algebra and the following form of $\sigma = \begin{pmatrix} 0 & 1 \\ -1 & 0 \end{pmatrix}$.

The discrete symmetry transformation, producing new solutions from the known ones, is as follows:

$$\begin{aligned} \frac{\partial F}{\partial \xi} &= S \frac{\partial \tilde{f}}{\partial \xi} S^{-1} - \xi \frac{\partial S}{\partial \xi} S^{-1} \\ \frac{\partial F}{\partial \bar{\xi}} &= S \frac{\partial \tilde{f}}{\partial \bar{\xi}} S^{-1} - \bar{\xi} \frac{\partial S}{\partial \bar{\xi}} S^{-1} \end{aligned}, \quad (3.2)$$

If we take the initial solution of (2.1) in the form of upper triangular matrix : $f = \tau H + \alpha X^+$, we have

$$\tau_{\xi\bar{\xi}} = 0, \quad (\xi - \bar{\xi})\alpha_{\xi\bar{\xi}} = \alpha_\xi - \alpha_{\bar{\xi}} \quad (3.3)$$

The result of integration of eq.(3.3) can be expressed in terms of chains of solutions of the following system of linear equations

$$\begin{aligned} \alpha[n+1]_\xi &= \xi \alpha[n]_\xi + \alpha[n] \\ \alpha[n+1]_{\bar{\xi}} &= \bar{\xi} \alpha[n]_{\bar{\xi}} + \alpha[n] \end{aligned} \quad (3.4)$$

The discrete symmetry transformation allows carrying out the recurrent procedure of finding the solutions of (2.1) in terms of chains (3.4) starting from the 0-step (3.3). The result of integration is as follows

$$\begin{aligned} f_n^- &= \frac{Det_{n-1}(\alpha)}{Det_n(\alpha)}, \quad f_n^0 = \tau + \frac{Det_n(\alpha)}{Det_n(\alpha)}, \\ f_n^+ &= \frac{Det_{n+1}(\alpha)}{Det_n(\alpha)}, \end{aligned} \quad (3.5)$$

where $Det_n(\alpha)$ are the minors of the order n of the following matrix:

$$\alpha = \begin{pmatrix} \alpha[0] & \alpha[1] & \alpha[2] & \dots \\ \alpha[1] & \alpha[2] & \alpha[3] & \dots \\ \alpha[2] & \alpha[3] & \alpha[4] & \dots \\ \dots & \dots & \dots & \dots \end{pmatrix}$$

Here $Det_n(\alpha)$ denotes that in the last row of the corresponding matrix the indices of $\alpha[i]$ are increased by one.

4. MATHEMATICA ALGORITHM

The induction to get the result (3.5) has not been proven yet. But the Mathematica software helps to get the solution at any step of the induction procedure. Below one can find the program for the first two steps in obtaining solutions.

$$In(1) := X^+ = \begin{pmatrix} 0 & 1 \\ 0 & 0 \end{pmatrix}; \quad X^- = \begin{pmatrix} 0 & 0 \\ 1 & 0 \end{pmatrix};$$

$$h = \begin{pmatrix} 1 & 0 \\ 0 & -1 \end{pmatrix}; \quad w = \begin{pmatrix} 0 & 1 \\ -1 & 0 \end{pmatrix};$$

$$G_0 = MatrixExp[MatrixExp[rh]];$$

$$S_1 = MatrixExp[s[1] X^+] MatrixExp[s_0[1] h];$$

$$G_1 = S_1 . w . G_0;$$

$$G_1$$

$$\begin{aligned} Out(4) &:= \{ \{ -e^{r-s_0[1]} s[1], \\ &e^{-r+s_0[1]} - e^{-r-s_0[1]} ns[1] \}, \\ &\{ -e^{r-s_0[1]}, -e^{-r-s_0[1]} n \} \} \end{aligned}$$

$$In(5) := G_1 = FullSimplify[G_1 /. s[1] \rightarrow \alpha[1] / .$$

$$n \rightarrow \alpha[-1] / . s_0[1] \rightarrow Log[\alpha[1]]]$$

$$Out(5) := \{ \{ \frac{e^r \alpha[1]}{\alpha[0]}, \frac{e^{-r} (\alpha[0]^2 - \alpha[-1] \alpha[1])}{\alpha[0]} \},$$

$$\{ -\frac{e^r}{\alpha[0]}, -\frac{e^{-r} \alpha[-1]}{\alpha[0]} \} \}$$

$$In(6) := \beta[1] = G_1[[2,1]] / G_1[[2,2]];$$

$$\alpha[1] = G_1[[1,2]] / G_1[[2,2]];$$

$$t[1] = -Log[G_1[[2,2]]];$$

$$FullSimplify[\alpha[1]]$$

$$Out(8) := -\frac{\alpha[0]^2}{\alpha[-1]} + \alpha[1]$$

$$In(9) := FullSimplify[t[1]]$$

$$Out(9) := -Log[\frac{e^{-r} \alpha[-1]}{\alpha[0]}]$$

$$In(10) := \beta[1] = G_1[[2,1]] / G_1[[2,2]];$$

$$Out(10) := \frac{e^{2r}}{\alpha[0]}$$

$$In(11) := s_0[2] = \text{Log} \left[\frac{\text{Det} \begin{bmatrix} \alpha[0] & \alpha[1] \\ \alpha[1] & \alpha[2] \end{bmatrix}}{\alpha[0]} \right];$$

$$s[2] = \frac{\alpha[0] \text{Det} \begin{bmatrix} \alpha[0] & \alpha[2] \\ \alpha[1] & \alpha[3] \end{bmatrix} - \alpha[1] \text{Det} \begin{bmatrix} \alpha[0] & \alpha[1] \\ \alpha[1] & \alpha[2] \end{bmatrix}}{\alpha[0]^2};$$

$$S_2 = \text{MatrixExp}[s[2] X^+] \text{MatrixExp}[s_0[2] h];$$

$$G_2 = S_2 . w . G_1; \quad \beta[2] = G_2[[2,1]] / G_2[[2,2]]; \quad \alpha[2] = G_2[[1,2]] / G_2[[2,2]]; \quad t[2] = -\text{Log}[G_2[[2,2]]];$$

$$\alpha[2] = G_2[[1,2]] / G_2[[2,2]]; \quad t[2] = -\text{Log}[G_2[[2,2]]];$$

$$t[2] = -\text{Log}[G_2[[2,2]]];$$

$$\text{FullSimplify}[\beta[2]]$$

$$\text{Out}(11) := \frac{e^{2r} \alpha[1]}{-\alpha[0]^2 + \alpha[1] \alpha[-1]}$$

$$\text{FullSimplify}[t[2]]$$

$$\text{Out}(12) := -\text{Log} \frac{e^{-r} (\alpha[0]^2 - \alpha[1] \alpha[-1])}{\alpha[1]^2 - \alpha[2] \alpha[0]}$$

$$\text{FullSimplify}[\alpha[2]]$$

$$\text{Out}(12) := \frac{\alpha[1]^3 - 2\alpha[0] \alpha[1] \alpha[2] + \alpha[-1] \alpha[2]^2}{\alpha[0]^2 - \alpha[1] \alpha[-1]} + \alpha[3]$$

The last expression is nothing more than

$$\alpha[2] = \frac{\text{Det} \begin{pmatrix} \alpha[-1] & \alpha[0] & \alpha[1] \\ \alpha[0] & \alpha[1] & \alpha[2] \\ \alpha[1] & \alpha[2] & \alpha[3] \end{pmatrix}}{\text{Det} \begin{pmatrix} \alpha[-1] & \alpha[0] \\ \alpha[0] & \alpha[1] \end{pmatrix}}$$

-
- [1] R.S. Ward, *Phil. Trans. R. Soc. Lond.*A315, 451 (1985); *Lect. Notes Phys.*, 1987, 280, 106; *Lond. Math. Soc. Lect. Notes Ser.*, 1990, 156, 246.
- [2] L.J. Mason and G.A. J.Sparling. *Phys. Lett.*, 1989, A137, 29; *J. Geom. and Phys.*, 1992, 8, 243.
- [3] S. Chakravarty, M.J. Ablowitz and P.A. Clarkson. *Phys. Rev. Lett.*, 1990, 1085.
- [4] I. Bakas and D.A. Depireux. *Mod. Phys. Lett.*, 1991, A6, 399.
- [5] M.J. Ablowitz, S. Chakravarty and L.A. Takhtajan. *Comm. Math. Phys.*, 1993, 158, 1289.
- [6] T.A. Ivanova and A.D. Popov. *Phys. Lett.*, 1992, A170, 293.
- [7] L.J. Mason and N.M.J. Woodhouse. *Nonlinearity* 1, 1988, 73; 1993, 6, 569.
- [8] M. Kovalyov, M. Legare and L. Gagnon. *J. Math. Phys.*, 1993, 34, 3425.
- [9] M. Legare and A.D. Popov. *Pis'ma Zh. Eksp. Teor. Fiz.*, 1994, 59, 845.
- [10] A.A. Belavin and V.E. Zakharov. *Phys. Lett.*, 1978, B73, 53.
- [11] A.N. Leznov and M.A. Mukhtarov. *J. Math. Phys.*, 1987, 28 (11), 2574; *Prepr. IHEP*, 1987, 87-90. *Prepr. ICTP 163*, Trieste, Italy, 1990; *J. Sov. Lazer Research*, 13 (4), 284, 1992.
- [12] Aliev B.N and A.N. Leznov. *Acta Appl. Math.*, 28, 201 (1992)
- [13] A.N. Leznov, M.A. Mukhtarov and W.J. Zakrzewski. *Tr. J. of Physics* 1995, 19, 416.
- [14] A.N. Leznov, *Prepr. IHEP*, 1991, 91-145

Received: 26.07.2011

VIBRATIONAL FREQUENCIES AND STRUCTURAL INVESTIGATION OF $[M(CN)_4]^{2-}$ (M = Cd, Hg AND Zn) IONS

GÜRKAN KEŞAN¹, CEMAL PARLAK², TOMÁŠ POLÍVKA¹, MUSTAFA ŞENYEL³

¹*Institute of Physical Biology, University of South Bohemia,*

Zamek 136,373 33 Nove Hradý, Czech Republic

²*Department of Physics, Dumlupınar University, Kütahya, 43100, Turkey*

³*Department of Physics, Science Faculty, Anadolu University, Eskişehir, 26470, Turkey*

E-mail: cparlak20@gmail.com, Tel.: +90 (274) 265 20 51 / 3116, Fax: +90 (274) 265 20 56

The normal mode frequencies and corresponding vibrational assignments of tetracyanometallate (II) ions ($[M(CN)_4]^{2-}$, M = Cd, Hg and Zn) have been theoretically examined by means of standard quantum chemical techniques. All normal modes have been successfully assigned to one of six types of motion (symmetric C≡N stretching, asymmetric C≡N stretching, symmetric M-C stretching, M-C≡N bending, M-C stretching + M-C≡N bending and C-M-C bending) utilizing the T_d symmetry of $M(CN)_4^{2-}$. Calculations have been performed at the Becke-3-Lee-Yang-Parr (B3LYP) density functional method using the Lanl2dz effective core basis set. Furthermore, reliable vibrational assignments have made on the basis of potential energy distribution (PED) calculated and the thermodynamics functions, highest occupied and lowest unoccupied molecular orbitals (HOMO and LUMO) of the title ions have been predicted together with their infrared intensities and Raman activities. Theoretical results have been successfully compared against available experimental data.

Keywords: Vibrational spectra, tetracyanocadmate, tetracyanomercurate, tetracyanozincate.

PACS: 31.15. E, 33.20.Ea, 33.20.Tp

1. INTRODUCTION

Tetracyanocadmate (II), tetracyanomercurate (II) and tetracyanozincate (II) ions are very important coordination compounds for inorganic chemistry and have been frequently used as bridging groups in various metal complexes [1-6]. Experimental data of the geometric parameters and vibrational spectra of $[M(CN)_4]^{2-}$ (M = Cd, Hg and Zn) ions exist in the literature [4, 7-9]. The B3LYP density functional model exhibits good performance on electron affinities, excellent performance on bond energies and reasonably good performance on vibrational frequencies and geometries of inorganic or ion compounds [10] as well as organic and neutral compounds [11]. The Lanl (Los Alamos National Laboratory) basis sets, also known as Lanl2dz (Lanl-2-double zeta) and developed by Hay and Wadt [12-14], have been widely used in quantum chemistry, particularly in the study of compounds containing heavy elements.

The goal of present study is to aid in making assignments to the fundamental normal modes of $[M(CN)_4]^{2-}$ (M = Cd, Hg and Zn) and in clarifying the experimental data available for these ions. In this study, the vibrational spectra of $[M(CN)_4]^{2-}$ ions are performed using the DFT/B3LYP method with Lanl2dz basis set and compared to available experimental data. Geometric parameters, thermodynamic properties, atomic charges and HOMO-LUMO molecular orbitals were also calculated for these ions with same level.

2. CALCULATION

For the vibrational calculations, molecular structures of tetracyanocadmate (II), tetracyanomercurate (II) and tetracyanozincate (II) ions were first optimized by B3LYP model with Lanl2dz basis set. The optimized geometric structure concerning to the minimum on the potential energy surface was provided by solving self-consistent

field (SCF) equation iteratively. The absence of imaginary frequencies confirmed that the optimized structure is a local minimum. After the optimization, the vibrational frequencies of $M(CN)_4^{2-}$ (M = Cd, Hg and Zn) ions were calculated using the same method and the basis set under the keyword Freq = Raman and then scaled to generate the corrected frequencies. Correction factors for selected regions or vibrational modes were calculated using $\sum (v^{exp} / v^{calc}) / n$ [10, 15]. The thermodynamics properties, HOMO and LUMO energies and Mulliken charges of related ions were also provided by B3LYP/Lanl2dz level. The calculation utilized the T_d symmetry of $[M(CN)_4]^{2-}$ (Figure 1) was performed using the Gaussian 09.A.1 program package [16]. Each of the vibrational modes was assigned by means of visual inspection using the GaussView 5.0.8 [17]. Gausssum 2.2.5 program was also used for visualization of the structure and simulated vibrational spectra [18].

3. RESULTS AND DISCUSSION

The optimized geometrical parameters of $[M(CN)_4]^{2-}$ calculated by DFT/B3LYP method with Lanl2dz basis set show that depending on the title ionic radii of the compounds, M – C bond lengths are different. According to the experimental geometric parameters, M-C distances are 2.08 Å [19], 2.27 Å - 2.30 Å [7, 4] and 2.18 Å - 2.22 Å [1, 7] for Zn, Cd and Hg, respectively. The calculated distances of the M-C bond for B3LYP/Lanl2dz model are about 2.14 Å, 2.30 Å and 2.32 Å, respectively. We see that the theoretical Hg-C bond is the longest of the three M-C bonds for the Lanl2dz basis set whereas the experimental Cd-C bond is the longest although cadmium lies between zinc and mercury in the periodic table.

Several thermodynamics parameters, capacity, zero point energy, entropy etc., calculated by DFT/B3LYP method Lanl2dz basis set are presented in Table 1. The

$[\text{Zn}(\text{CN})_4]^{2-}$ ion is more stable than the others. The variation in the Zero Point Vibrational Energy, ZPVE, seems to be insignificant. The total energy and change in total entropy of $[\text{M}(\text{CN})_4]^{2-}$ are at room temperature.

Table 1.
The thermodynamic parameters of $[\text{M}(\text{CN})_4]^{2-}$ (M = Cd, Hg and Zn) calculated by B3LYP/Lan12dz level.

Parameters	$\text{Cd}(\text{CN})_4^{2-}$	$\text{Hg}(\text{CN})_4^{2-}$	$\text{Zn}(\text{CN})_4^{2-}$
Optimizational global minimum energy, (Hartress)	-419.439	-414.080	-436.985
Thermal total energy, (kcal/mol)	24.783	24.683	25.110
Heat capacity, (kcal/mol k)	0.037	0.037	0.036
Entropy, (kcal/mol k)			
<i>Total</i>	0.116	0.119	0.110
<i>Translational</i>	0.042	0.043	0.041
<i>Rotational</i>	0.037	0.031	0.030
<i>Vibrational</i>	0.031	0.045	0.038
Vibrational energy, (kcal/mol)	23.006	22.905	23.332
Zero point vibrational energy, (kcal/mol)	16.781	16.494	17.571
Rotational constants (GHz)	0.7904	0.7630	0.8949
Dipol moment (Debye)	0.0019	0.0016	0.0012

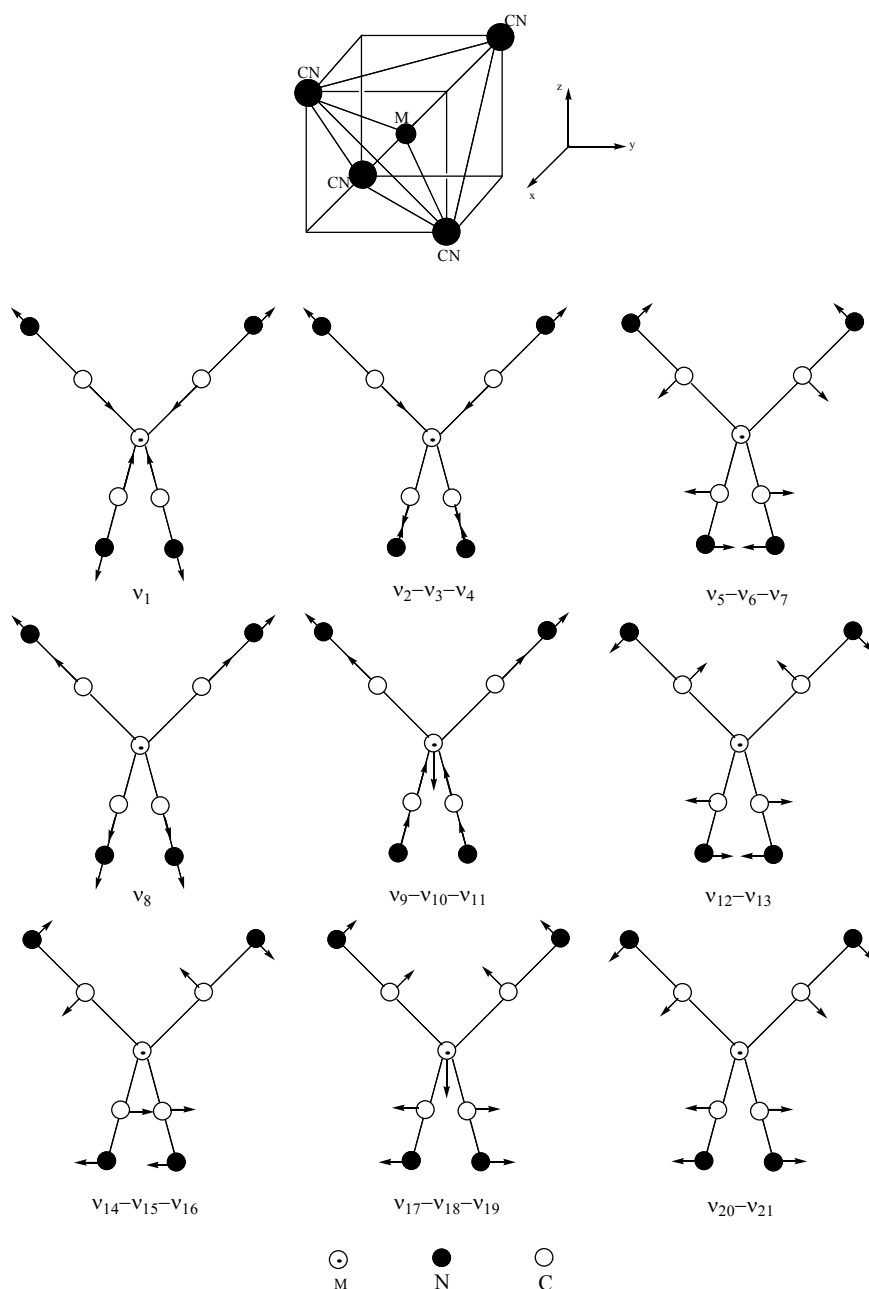


Fig. 1. Structure and normal modes of $[M(CN)_4]^{2-}$ ($M = Cd, Hg$ and Zn).

Table 1.

Normal modes of $[Cd(CN)_4]^{2-}$ ion calculated at the B3LYP/Lanl2dz level.

Symmetry / Mode	Calculated Frequency	IR Intensity ^a	Raman Activity ^b	Assignment	Experimental Frequency ^c	Corrected Frequency ^e	PED ^f
A_1 / ν_1	2113	0	120.61	CN s-stretching	2149	2149	ν NC (92)
F_2 / ν_2	2112	6.85	39.28	CN a-stretching	2145	2145	ν NC (95)
F_2 / ν_3	2112	6.83	39.59	CN a-stretching	-	2145	ν NC (85)
F_2 / ν_4	2112	6.84	39.46	CN a-stretching	-	2145	ν NC (94)
E / ν_5	265	0	1.41	CdCN bending	258 ^d	253	ν CdC (14) + δ NCCd (38)
E / ν_6	265	0	1.41	CdCN bending	-	253	ν CdC (16) + δ NCCd (11) + τ NCCCd (36)
E / ν_7	265	0	1.42	CdCN bending	-	253	δ NCCd (34) + τ NCCCd (15)
A_1 / ν_8	263	0	7.06	CdC s-stretching	324	324	ν CdC (97)
F_2 / ν_9	256	90.55	2.57	CdC stretching + CdCN bending	316	284	ν CdC (68)
F_2 / ν_{10}	256	91.48	2.50	CdC stretching + CdCN bending	-	284	ν CdC (72)
F_2 / ν_{11}	256	85.63	2.57	CdC stretching + CdCN bending	-	284	ν CdC (68)
F_2 / ν_{12}	255	1.71	9.15	CdC stretching + CdCN bending	250	282	δ NCCd (16) + δ CCCCd (10) + τ NCCCd (34)
F_2 / ν_{13}	255	0.85	9.53	CdC stretching + CdCN bending	-	282	δ NCCd (34) + τ NCCCd (30)
F_1 / ν_{14}	208	0	0	CdCN bending	194	198	δ NCCd (69) + τ NCCCd (26)
F_1 / ν_{15}	208	0	0	CdCN bending	-	198	δ NCCd (79) + τ NCCCd (11)
F_1 / ν_{16}	208	0	0	CdCN bending	-	198	δ NCCd (82) + τ NCCCd (14)
F_2 / ν_{17}	71	28.49	2.42	CCdC bending	61	71	δ CCCd (17) + τ CCCCd (47)
F_2 / ν_{18}	71	28.47	2.42	CCdC bending	-	71	δ CCCd (36) + τ CCCCd (29)
F_2 / ν_{19}	71	28.59	2.41	CCdC bending	-	71	δ CCCd (32) + τ CCCCd (33)
E / ν_{20}	56	0	5.10	CCdC bending	64 ^d	56	δ CCCd (68)
E / ν_{21}	56	0	5.09	CCdC bending	-	56	δ CCCd (36) + τ CCCCd (29)

^a Units of IR intensity are km/mol. ^b Units of Raman scattering activity are $\text{\AA}^4/\text{amu}$. ^c Reference [7]. ^d Calculated frequencies of E mode of this ion by Jones [7]. ^e Raw calculated frequencies multiplied by the correction factors in Table 5. ^f PED data are taken from VEDA4. s; symmetric, a; asymmetric. ν , δ and τ denote stretching, bending and torsion, respectively.

Table 2.

Normal modes of $[Hg(CN)_4]^{2-}$ ion calculated at the B3LYP/Lanl2dz level.

Symmetry / Mode	Calculated Frequency	IR Intensity ^a	Raman Activity ^b	Assignment	Experimental Frequency ^c	Corrected Frequency ^e	PED ^f
A_1 / ν_1	2112	0	123.41	CN s-stretching	2149	2149	ν NC (98)
F_2 / ν_2	2111	8.39	45.18	CN a-stretching	2146	2146	ν NC (98)
F_2 / ν_3	2111	8.38	45.31	CN a-stretching	-	2146	ν NC (98)
F_2 / ν_4	2111	8.39	45.25	CN a-stretching	-	2146	ν NC (78)
E / ν_5	258	0	5.62	HgCN bending	245 ^d	238	ν HgC (22) + δ NCHg (32) + δ CCHg (20)
E / ν_6	258	0	5.61	HgCN bending	-	238	ν HgC (31) + δ NCHg (32)
E / ν_7	258	0	5.61	HgCN bending	-	238	ν HgC (22) + δ NCHg (17) + τ NCHgC (16) + δ CCHg (20)
A_1 / ν_8	256	0	12.84	HgC s-stretching	335	335	ν HgC (99)
F_2 / ν_9	243	81.75	2.97	HgC stretching + HgCN bending	330	293	δ NCHg (16) + δ CHgC (12) + τ NCHgC (43)
F_2 / ν_{10}	243	81.70	2.97	HgC stretching + HgCN bending	-	293	δ NCHg (40) + δ CHgC (15) + τ NCHgC (16)
F_2 / ν_{11}	243	81.75	2.97	HgC stretching + HgCN bending	-	293	ν HgC (50)
F_2 / ν_{12}	223	0.57	7.45	HgC stretching + HgCN bending	235	269	ν HgC (62)
F_2 / ν_{13}	223	0.58	7.44	HgC stretching + HgCN bending	-	269	ν HgC (65)
F_1 / ν_{14}	201	0	0	HgCN bending	180	185	δ NCHg (55) + τ NCHgC (33)
F_1 / ν_{15}	201	0	0	HgCN bending	-	185	δ NCHg (46) + τ NCHgC (29)
F_1 / ν_{16}	201	0	0	HgCN bending	-	185	δ NCHg (28) + NCHgC (67)
F_2 / ν_{17}	63	34.90	2.58	CHgC bending	54	65	δ CHgC (13) + τ CCCHg (56)
F_2 / ν_{18}	63	34.90	2.58	CHgC bending	-	65	δ CHgC (54)
F_2 / ν_{19}	63	34.89	2.58	CHgC bending	-	65	δ CHgC (11) + τ CCCHg (54)
E / ν_{20}	52	0	6.22	CHgC bending	63 ^d	54	δ CHgC (73)
E / ν_{21}	52	0	6.23	CHgC bending	-	54	δ CHgC (55) + τ CCCHg (16)

^a Units of IR intensity are km/mol. ^b Units of Raman scattering activity are Å⁴/amu. ^c Reference [7]. ^d Calculated frequencies of E mode of this ion by Jones [7]. ^e Raw calculated frequencies multiplied by the correction factors in Table 5. ^e PED data are taken from VEDA4. s; symmetric, a; asymmetric. v, δ and τ denote stretching, bending and torsion, respectively.

Each of the title ions consists of 9 atoms, so it has 21 normal mode frequencies and belongs to the T_d point group. Within this point group, vibrational modes belong to the symmetry species A₁, A₂, E, F₁ and F₂ and are distributed as 2A₁, 2E, F₁ and 4F₂. On the basis of the symmetry properties of the dipole moment and polarisability operator, it can easily be seen that the A₁ and E modes are only Raman active whereas the F₂ mode is both IR and Raman active. Fig. 1. demonstrates normal modes for these ions. Crystal structures of K₂M(CN)₄ (M = Cd, Hg and Zn) salts were determined and they were found to be cubic with space group O_h [20]. The [M(CN)₄]²⁻ ions within these salts are situated on special positions of point group T_d and, thus, the site group is the same as the isolated ion point group [21]. Therefore, we have used vibrational spectra of these salts [7] as references for related ions. The calculated vibrational frequencies of [M(CN)₄]²⁻ ions at B3LYP with Lanl2dz basis set are given in Tables 2-4, together with related experimental data, for comparison.

The correction factors are obtained by taking the average of the ratios between the computed and experimental frequencies for all modes of a particular motion type [10, 15]. The computed correction factors for the B3LYP/Lanl2dz are presented in Table 5. These correction factors have been used to generate the corrected frequencies in the last column of Tables 2-4. Bytheway and Wong performed similar calculations using the B3LYP/Lanl2dz on a set of 50 inorganic molecules. Their correction factor was within 1 % 1.00 [15]. Additionally, Check et. al's correction factors were 1.167 and 1.065 of B3LYP method for Lanl2dz and Lanl2dvpd basis sets on a set of 36 metal halide molecules [10]. It can be seen from Table 5 that average correction factors of [M(CN)₄]²⁻ (M = Cd, Hg and Zn) ions in this study are found as 1.0544, 1.0843 and 1.0541, respectively. Average of these three values is 1.0643. Determined correction factors in this study are in good agreement with previously reported values [10, 15].

Table 3.

Normal modes of [Zn(CN)₄]²⁻ ion calculated at the B3LYP/Lanl2dz level.

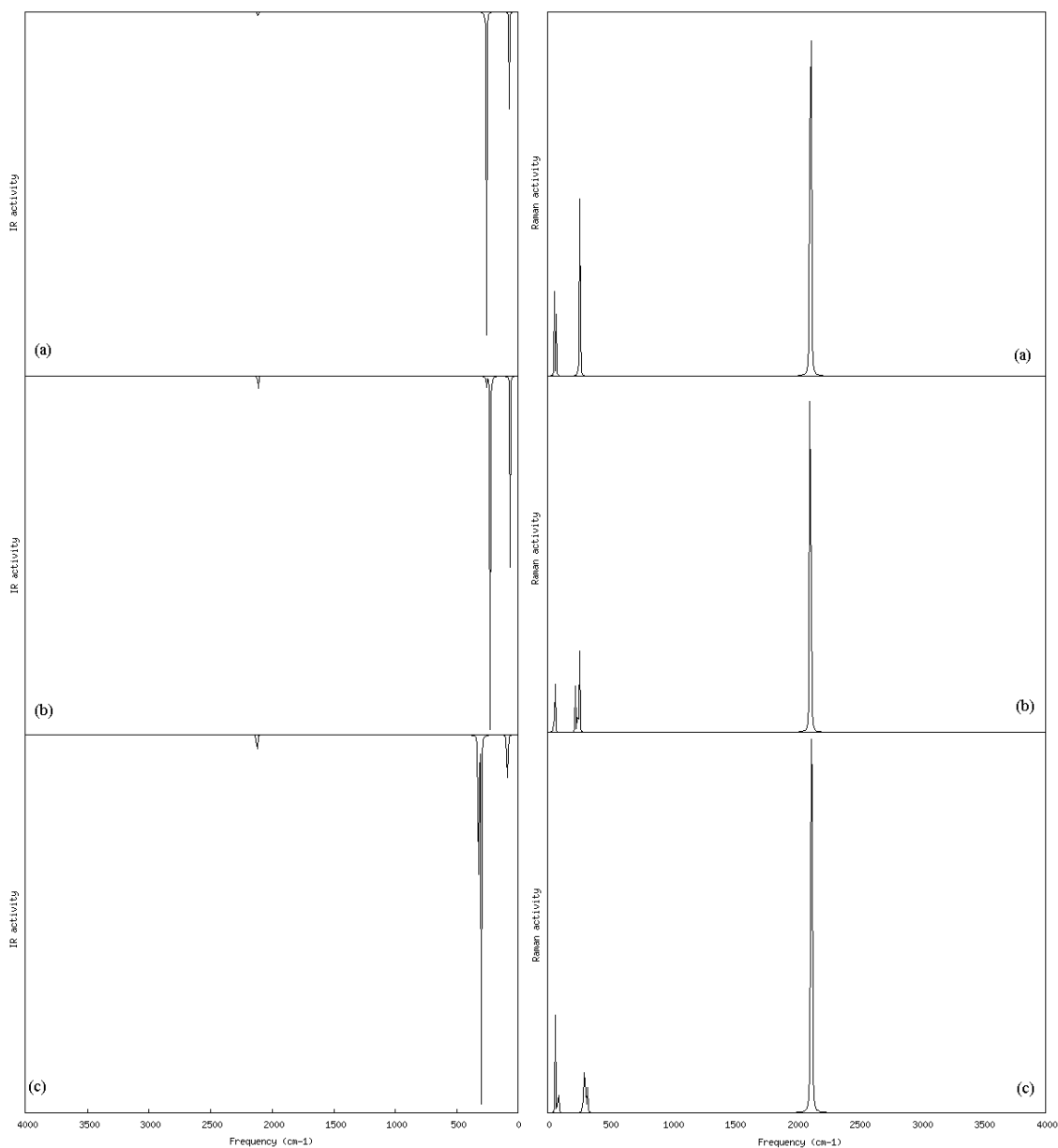
Symmetry / Mode	Calculated Frequency	IR Intensity ^a	Raman Activity ^b	Assignment	Experimental Frequency ^c	Corrected Frequency ^e	PED
A ₁ / v ₁	2121	0	136.63	CN s-stretching	2157	2157	v NC (98)
F ₂ / v ₂	2120	7.75	37.28	CN a-stretching	2152	2152	v NC (98)
F ₂ / v ₃	2120	7.75	37.28	CN a-stretching	-	2152	v NC (96)
F ₂ / v ₄	2120	7.75	37.27	CN a-stretching	-	2152	v NC (89)
E / v ₅	318	0	2.58	ZnCN bending	330 ^d	322	δ NCZn (48) + τ CCCZn (23)
E / v ₆	318	0	2.58	ZnCN bending	-	322	δ CZnC (27) + τ NCZnC (26)
E / v ₇	318	0	2.58	ZnCN bending	-	322	δ NCZn (11) + τ NCZnC (20) + τ CCCZn (23)
A ₁ / v ₈	300	0	10.11	ZnCN s-stretching	342	342	δ NCZn (33) + v NC (13) + τ NCZnC (29)
F ₂ / v ₉	296	48.94	0.06	ZnC stretching + ZnCN bending	359	343	δ NCZn (27) + δ CZnC (14) + τ NCZnC (34)
F ₂ / v ₁₀	296	49.32	0.07	ZnC stretching + ZnCN bending	-	343	v ZnC (81)
F ₂ / v ₁₁	296	49.37	0.07	ZnC stretching + ZnCN bending	-	343	v ZnC (74)
F ₂ / v ₁₂	285	0.01	5.19	ZnC stretching + ZnCN bending	315	330	v ZnC (85)
F ₂ / v ₁₃	285	0.02	5.15	ZnC stretching + ZnCN bending	-	330	v ZnC (98)
F ₁ / v ₁₄	233	0	0	ZnCN bending	230	236	δ NCZn (95)
F ₁ / v ₁₅	233	0	0	ZnCN bending	-	236	δ NCZn (67) + τ NCZnC (22)
F ₁ / v ₁₆	233	0	0	ZnCN bending	-	236	δ NCZn (73) + τ NCZnC (16)
F ₂ / v ₁₇	85	21.26	2.51	CZnC bending	71	83	δ CZnC (14) + τ NCZnC (10) + τ CCCZn (45)
F ₂ / v ₁₈	85	21.26	2.51	CZnC bending	-	83	δ CCZn (13) + τ CCCZn (58)
F ₂ / v ₁₉	85	21.24	2.51	CZnC bending	-	83	δ CZnC (56)
E / v ₂₀	63	0	4.93	CZnC bending	71 ^d	62	δ CZnC (51) + τ CCCZn (14)
E / v ₂₁	63	0	4.92	CZnC bending	-	62	δ CZnC (67)

^a Units of IR intensity are km/mol. ^b Units of Raman scattering activity are Å⁴/amu. ^c Reference [7]. ^d Calculated frequencies of E mode of this ion by Jones [7]. ^e Raw calculated frequencies multiplied by the correction factors in Table 5. ^e PED data are taken from VEDA4. s is symmetric, a is asymmetric. v, δ and τ denote stretching, bending and torsion, respectively.

Table 5.

Correction factors for the normal modes of $[M(CN)_4]^{2-}$ ions.

Band motion	B3LYP/ Lanl2dz		
	$Cd(CN)_4^{2-}$	$Hg(CN)_4^{2-}$	$Zn(CN)_4^{2-}$
$C\equiv N$ s-stretching	1.0170	1.0175	1.0170
$C\equiv N$ a-stretching	1.0156	1.0166	1.0151
M-C s-stretching	1.2319	1.3086	1.1400
M-C $\equiv N$ bending	0.9532	0.9226	1.0124
M-C stretching + M-C $\equiv N$ bending	1.1074	1.2059	1.1591
C-M-C bending	1.0011	1.0343	0.9812
Average	1.0544	1.0843	1.0541

Fig. 2. Infrared and Raman spectra of $[M(CN)_4]^{2-}$ (M = Cd (a), Hg (b) and Zn (c)).

The biggest difference between the experimental and corrected wavenumbers is 32 cm^{-1} for $Cd(CN)_4^{2-}$, 37 cm^{-1} for $Hg(CN)_4^{2-}$ and 16 cm^{-1} for $Zn(CN)_4^{2-}$. In order to make a comparison between the experimental and theoretical wavenumbers, the correlation graphics have been computed and the correlation values with

B3LYP/Lanl2dz model are found to be 0.99962 for $Cd(CN)_4^{2-}$, 0.99953 for $Hg(CN)_4^{2-}$ and 0.99986 for $Zn(CN)_4^{2-}$. It can be seen that the B3LYP/Lanl2dz results of $Zn(CN)_4^{2-}$ ion are better than the others. Furthermore, we have calculated root mean square deviation (RMSD) which is a frequently used measure of the differences

between values predicted by a model and actually observed from the thing being modeled. RMSD is given by

$$RMSD = \sqrt{\sum_i^N (\lambda w_i^{th} - w_i^{exp})^2 / N}$$

where N is the total number of vibrational modes, λ is scaling factor, w^{th} and w^{exp} are the theoretical and experimental frequencies (cm^{-1}), respectively [15]. In this study, RMSD value has been obtained as about 15.8 cm^{-1} for $[\text{Cd}(\text{CN})_4]^{2-}$, 17.6 cm^{-1} for $[\text{Hg}(\text{CN})_4]^{2-}$ and 9.5 cm^{-1} for $[\text{Zn}(\text{CN})_6]^{2-}$. The calculated Infrared and Raman spectra of the title ions are given in Figure 2.

Table 6 presents the Mulliken charge distribution of $[\text{M}(\text{CN})_4]^{2-}$ ($\text{M} = \text{Cd}, \text{Hg}$ and Zn) ions at the B3LYP/Lanl2dz level of theory. Regarding the calculations, there is a considerable positive charge on metal atoms (0.4396, 0.3172 and 0.4408 for Cd, Hg and Zn, respectively) with a corresponding negative charge on each carbon and nitrogen atom. This suggests that these ions are held together in part by electrostatic forces.

Table 6.

Mulliken charge distribution for $[\text{M}(\text{CN})_4]^{2-}$ ($\text{M} = \text{Cd}, \text{Hg}$ and Zn).

Atom	B3LYP/Lanl2dz		
	$\text{Cd}(\text{CN})_4^{2-}$	$\text{Hg}(\text{CN})_4^{2-}$	$\text{Zn}(\text{CN})_4^{2-}$
Cd	0.4396	-	-
Hg	-	0.3172	-
Zn	-	-	0.4408
C	-0.3817	-0.3597	-0.3499
N	-0.2282	-0.2196	-0.2603

The HOMO and LUMO orbitals are the main orbital take part in chemical stability. The HOMO describes the ability to donate an electron and LUMO as an electron acceptor. The absorption of the electronic transition is defined from the ground to the first excited state. In other words, the transitions can be described from HOMO to LUMO. The HOMO is located over C atoms in $[\text{M}(\text{CN})_4]^{2-}$ ions whereas the LUMO is dominated for N and M atoms. The atomic compositions of the frontier molecular orbital and their orbital energies are shown in fig. 3.

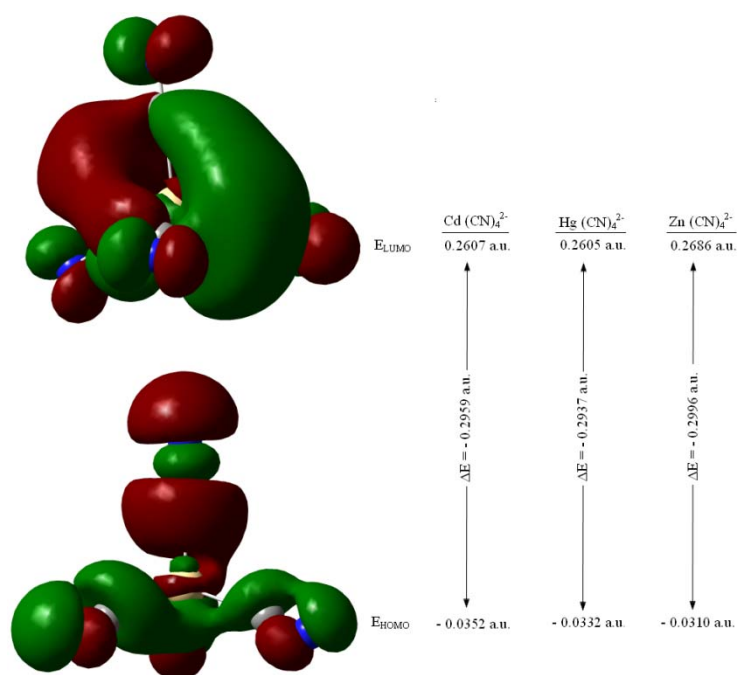


Fig. 3. Atomic orbital compositions of the frontier molecular orbital for $[\text{M}(\text{CN})_4]^{2-}$ ($\text{M} = \text{Cd}, \text{Hg}$ and Zn).

4. CONCLUSION

In present investigation, molecular structure, vibrational frequencies, thermodynamics parameters and HOMO-LUMO orbitals have been studied using DFT/B3LYP method with Lanl2dz basis set. Comparing the computed vibrational frequencies with experimental

spectra available in the literature, a set of scaling factors is derived which is in good agreement with literature. The $[\text{Zn}(\text{CN})_4]^{2-}$ ion is more stable than others. According to the RMSD, the results of Lanl2dz effective core basis set for Zn metal are better than Cd and Hg transition metals.

[1] K.F. Mok, V. Mckee and W. Robinson. "Structure of a dipotassium tetracyanomercurate(II) salt with dibenzo-18-crown-6" Acta Cryst. C 43, 1987, 2093-2096.

[2] Y. Guo, R. Weiss, R. Boese, M. Eppe. "Synthesis, structural characterization and thermochemical reactivity of tris(ethylenediamine)zinc tetracyanozincate, a precursor for nanoscale ZnO" Thermochim. Acta 446, 2006, 101-105.

- [3] T. Iwamoto, S. Nishikiori, T. Kitazawa and H. Yuge. "Mineralomimetic chemistry as a modern aspect of co-ordination chemistry" J. Chem. Soc. Dalton Trans. 22, 1997, 4127-4136.
- [4] H. Yuge and T. Iwamoto. "Crystal structures of catena- [dilatocadmium (II) tetra- μ -cyanocadmium (II)] host clathrates: Diamminecadmium (II) tetracyanocadmium (II)-benzene (1/2), diamminecadmium (II) tetracyanocadmium (II) - aniline (1/2), ethylenediaminecadmium (II) tetracyanocadmium (II) - aniline (1/2), and a novel type bis (aniline) cadmium (II) tetracyanocadmium (II) - aniline (2/1)" J. Incl. Phenom. 14, 1992, 217-235.
- [5] K. Nakamoto. "Infrared and Raman spectra of inorganic and coordination compounds" Wiley, New York, 1986.
- [6] C. Parlak, Ö. Alver, M. Şenyel. "Vibrational spectroscopic study on some Hofmann-T_d type clathrates: Ni(4-Phenylpyridine)₂M(CN)₄·2G (M=Cd or Hg, G=1,4-dioxane)" Spectrochimica Acta A, 78, 2011, 1487-1491.
- [7] L.H. Jones. "Vibrational spectrum and structure of metal cyanide complexes in the solid state-V: K₂Zn(CN)₄, K₂Cd(CN)₄ and K₂Hg(CN)₄" Spectrochim. Acta 17, 1961, 188-200.
- [8] B. Ziegler and D.Babel. "The crystal-structure of the cyano spinel K₂Cd(CN)₄" Z. Naturforsch. 46 B, 1991, 47-49.
- [9] P.N. Gerlach and B.M. Powell. "Crystal-structures and phase-transition of the cyanospinel K₂Hg(CN)₄" J. Chem. Phys. 85, 1986, 6004-6009.
- [10] C. E. Check, T. O. Faust, J. M. Bailey, B. J. Wright, T. M. Gilbert, L. S. Sunderlin. Journal of Physical Chemistry A, "Addition of Polarization and Diffuse Functions to the LANL2DZ Basis Set for P-Block Elements" 105, 2001, 8111-8116.
- [11] C. Parlak. "Theoretical and experimental vibrational spectroscopic study of 4-(1-Pyrrolidiny) piperidine" Journal of Molecular Structure, 966, 2010, 1-7.
- [12] P.J. Hay, W.R. Wadt. "Ab initio effective core potentials for molecular calculations. Potentials for the transition metal atoms Sc to Hg" J. Chem. Phys., 82, 1985, 270-283.
- [13] W.R. Wadt, P.J. Hay. "Ab initio effective core potentials for molecular calculations. Potentials for main group elements Na to Bi" J. Chem. Phys., 82, 1985, 284-295.
- [14] P.J. Hay, W.R. Wadt. "Ab initio effective core potentials for molecular calculations. Potentials for K to Au including the outermost core orbitals" J. Chem. Phys., 82, 1985, 299-310.
- [15] I. Bytheway, M. W. Wong. "The prediction of vibrational frequencies of inorganic molecules using density functional theory" Chem. Phys. Lett., 282, 1998, 219-226.
- [16] M. J. Frisch, G. W. Trucks, H. B. Schlegel, G. E. Scuseria, M. A. Robb, J. R. Cheeseman, G. Scalmani, V. Barone, B. Mennucci, G. A. Petersson, H. Nakatsuji, M. Caricato, X. Li, H. P. Hratchian, A. F. Izmaylov, J. Bloino, G. Zheng, J. L. Sonnenberg, M. Hada, M. Ehara, K. Toyota, R. Fukuda, J. Hasegawa, M. Ishida, T. Nakajima, Y. Honda, O. Kitao, H. Nakai, T. Vreven, J. A. Montgomery, Jr., J. E. Peralta, F. Ogliaro, M. Bearpark, J. J. Heyd, E. Brothers, K. N. Kudin, V. N. Staroverov, R. Kobayashi, J. Normand, K. Raghavachari, A. Rendell, J. C. Burant, S. S. Iyengar, J. Tomasi, M. Cossi, N. Rega, J. M. Millam, M. Klene, J. E. Knox, J. B. Cross, V. Bakken, C. Adamo, J. Jaramillo, R. Gomperts, R. E. Stratmann, O. Yazyev, A. J. Austin, R. Cammi, C. Pomelli, J. W. Ochterski, R. L. Martin, K. Morokuma, V.G. Zakrzewski, G. A. Voth, P. Salvador, J. J. Dannenberg, S. Dapprich, A. D. Daniels, Ö. Farkas, J. B. Foresman, J. V. Ortiz, J. Cioslowski and D. J. Fox. Gaussian 09, Revision A.1, Gaussian Inc., Wallingford CT, 2009.
- [17] R.D. Dennington, T. A. Keith, J. M. Millam, GaussView 5.0.8, Gaussian Inc., 2008.
- [18] N.M. O'Boyle, A.L. Tenderholt, K.M. Langner. J. "cclib: A library for package-independent computational chemistry algorithms" Comp. Chem. 29, 2008, 839-845.
- [19] L. Pauling. Nature of the Chemical Bond, p 179, Cornell University Press, Ithaca, New York, 1945.
- [20] R.G. Dickinson, "The crystal structures of complex cyanides of potassium with zinc, cadmium and mercury" J. Am. Chem. Soc. 44, 1922, 774-784.
- [21] R.S. Halford. "Motions of molecules in condensed systems: I. selection rules, relative intensities, and orientation effects for Raman and infrared spectra" J. Chem. Phys. 14, 1946, 8-15.

Received: 14.09.2011

ZnO NANORODS BY SIMPLIFIED SPRAY PYROLYSIS

SERDAR AYDIN^{1*}, GÜVEN TURGUT¹, MEHMET YILMAZ^{1,2}
AND MEHMET ERTUĞRUL³¹*K. K. Education Faculty, Department of Physics, Ataturk University, Erzurum 25240, Turkey*²*Art and Science Faculty, Department of Physics, Bingöl University, Bingöl 12000, Turkey*³*Engineering Faculty, Department of Electricity and Electronic, Ataturk University, Erzurum 25240, Turkey***Corresponding author, Tel; 904422314011, fax; 904423360955**E-mail: serdar@atauni.edu.tr*

ZnO layers were deposited by a simple and cost-effective spray pyrolysis using zinc chloride aqueous solutions on glass substrates at 600°C. The structural properties of nanorods were characterized by X-ray diffraction (XRD), scanning electron microscopy (SEM). XRD studies showed that the films were polycrystalline and were preferentially oriented along (002) direction. Other orientations observed were (102), (103) and (004). The standard and the calculated from XRD data lattice constants are in harmony. Also, it was observed that the deposited films are of ZnO with hexagonal structure and the surfaces of the films are found to be nonhomogeneous with hexagonal shaped rods.

Keywords: ZnO, nanostructure, simplified spray pyrolysis.**PACS:** 73.61Ey; 85.40Ux; 61.82Rx

INTRODUCTION

Nanostructured materials have attracted considerable interest in recent years due to their potential application in nanoscale electronic and optoelectronic devices. ZnO nanostructures have potential applications in solar cells, gas sensors, short-wavelength light-emitting and field effect devices, schottky diodes, coating materials etc. (Devoda et al. 2007) due to its excellent properties such as wide and direct band-gap of 3.3 eV and a high exciton binding energy of 60meV (Sawada et al. 2002; Choopun et al. 1999; Li et al. 2000; Guo et al. 2000)

ZnO nanostructures have been prepared various experimental techniques such as a thermal vapor transport method (Cai et al. 2011), spray pyrolysis (Dedova et al. 2007; Krunks et al. 2008), chemical vapour deposition (CVD), electrochemical deposition (He et al. 2010), pulsed laser deposition (PLD) (Valerini et al. 2008), sol-gel (Bahadur et al. 2007) etc. Among these techniques, spray pyrolysis is a simple, convenient and low-cost technique for large area coatings (Ravichandran & Philominathan 2008), ease of adding doping materials, reproducibility, high growth rate and mass production capability for uniform large area coatings (Serin et al. 2006). In this study, a further simplified and low cost spray pyrolysis technique using a perfume atomizer (generally used for cosmetics) is employed for the fabrication of ZnO nanostructure.

In conventional spray method, usually a carrier gas such as O₂, N₂ or air is used for spraying the precursor solution. But, in the a simplified and inexpensive spray technique using perfume atomizer atomization is based on hydraulic pressure without using any carrier gas, enhanced wettability between the sprayed microparticles and the previously deposited layers, intermittent spraying and fine atomization. Perfume atomizers avoid deposition of large droplets, which often takes place in conventional spray pyrolysis depositions, enhanced wettability between sprayed microparticles and the previously deposited layers (Ravichandran & Philominathan 2008;

Ravichandran et al. 2009; Ravichandran & Philominathan 2009).

EXPERIMENTAL

An aqueous solution (0.1 M) of ZnCl₂ was used to deposit ZnO films. The solution was stirred magnetically for 1 h, which was followed by an magnetic stirring for 30 min. The clear precursor solution thus obtained was sprayed onto the pre-heated at 600°C glass substrates were cleaned ultrasonically with organic solvents (dimension 1×1 ×0,1 mm³) using a perfume atomizer. The temperature of the substrates was monitored by employing a temperature controller with a chromel-alumel thermocouple. The nozzle to substrate distance was optimized as 40cm. The intermittent spray cycle followed in this study is a two-step procedure: a spray for 1 s and an interval for 10 s. The spray interval enables the substrates to attain the required temperature before the start of the next spray. After the deposition, coated substrates were allowed to naturally cool down to room temperature.

The structural characterization of the films prepared was carried out by X-ray diffraction (XRD) measurements using a Rigaku D/Max-IIIC diffractometer with CuK α radiation ($\lambda=1.5418$ Å), at 30 kV, 10 mA. Surface morphology was examined by a TESCAN VegaII LSU model SEM.

RESULTS AND DISCUSSION

The XRD patterns of the films deposited were shown in figure 1. XRD images showed that the films were polycrystalline and were preferentially oriented along (002) direction. Other orientations observed were (102), (103) and (004). The observed 'd' values were presented in Table 1 and these values were compared with the standard ones from JPDFS card no: 36-1451. The matching of the observed and standard 'd' values confirms that the deposited films are of ZnO with hexagonal structure.

The lattice constants of ZnO with hexagonal structure 'a' and 'c' was determined by relation (Ravichandran & Philominathan 2008).

$$\frac{1}{d^2} = \frac{4}{3} \left(\frac{h^2 + k^2 + hk}{a^2} \right) + \left(\frac{l^2}{c^2} \right)$$

where 'd' is the interplaner distance and (hkl) miller indices, respectively.

The standard and calculated lattice constants were given in Table 1. The calculated 'a' and 'c' values agree with JPCDS card no: 36-1451. As seen from Table 1, the standard and the calculated lattice constants are in harmony.

Fig. 2 shows the SEM images of the ZnO films. From the SEM image, the surfaces of the films are found to be nonhomogeneous with hexagonal shaped rods. The hexagonal shaped rods were oriented in different directions and this conclusion is in compliance with the XRD results.

Table 1.

Structural parameters of the ZnO

(hkl)	(hkl)	Standard d(Å)	Calculated d(Å)	Standart Lattice constants (Å)		Calculated Lattice constants (Å)	
				a	c	a	c
002	(002)	2,6033	2,6240	3,250	5,207	3,251	5,207
102	(102)	1,9111	1,9203				
103	(103)	1,4771	1,4820				
004	(004)	1,3017	1,3051				

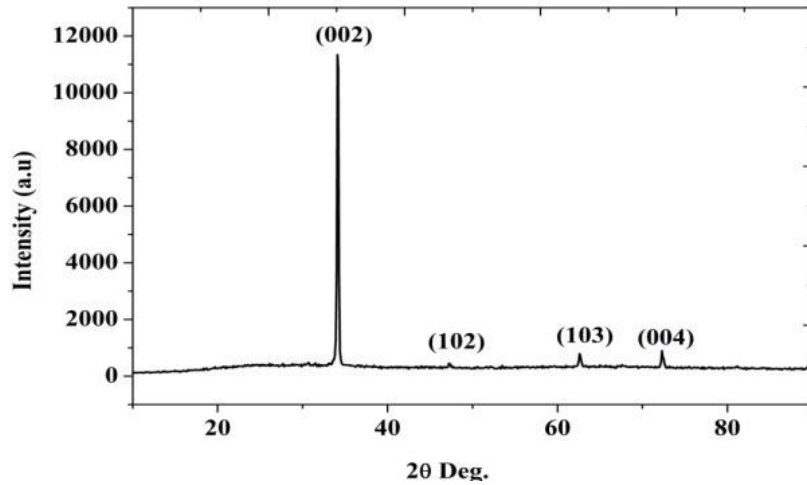


Fig.1. XRD pattern of ZnO thin film.

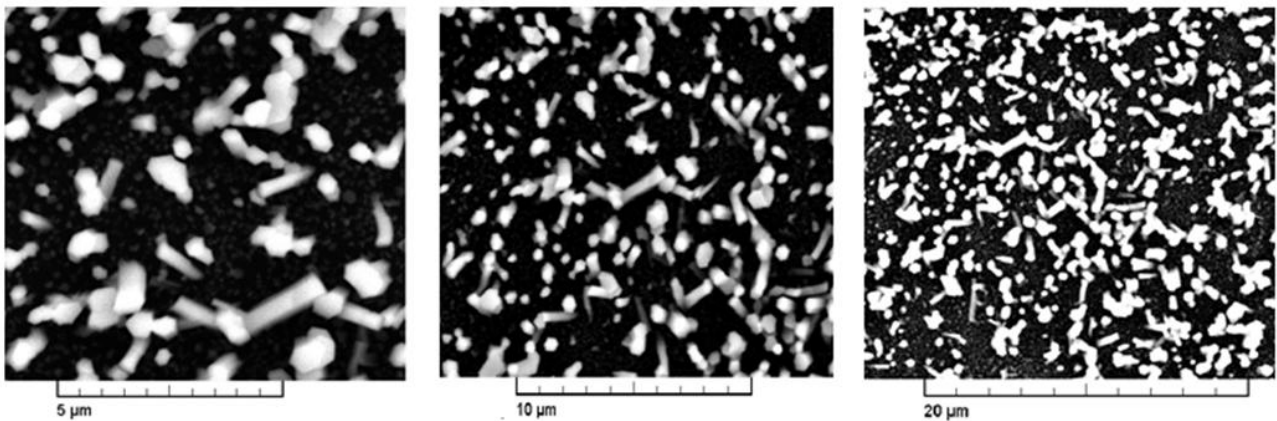


Fig. 2. SEM images of ZnO nanorods.

CONCLUSION

In conclusion, ZnO nanorods have successfully been synthesized on glass substrates by a simple and cost-effective spray pyrolysis. Structural analyses showed that

the nanorods are ZnO hexagonal wurzite crystals. From SEM images, the hexagonal shaped rods were oriented in different directions and this conclusion is in compliance with the XRD results.

-
- [1] H.Bahadur, A.K.Srivastava, D.Haranath, H.Chander, A.Basu, S.B. Samanta, K.N. Sood, R. Kishore, R.K. Sharma, Rashmi, V. Bhatt, P. Pal, S. Chandra. Indian Journal of Pure & Applied Physics. 45, 395-399, 2007.
- [2] F. Cai, L. Zhu, H. He, J. Li, Y. Yang, X. Chen, Z. Ye. Journal of Alloys and Compounds, 2011, 509, 316–320.
- [3] S. Choopun, R.D. Vispute, W. Noch, A. Balsamo, R.P. Sharma, T. Venkatesan, A. Iliadis, D.C. Look. Appl. Phys. Lett., 1999, 75, 3947.
- [4] T. Dedova, M. Krunks, M. Grossberg, O. Volobujeva, I. Acik Oja. A novel deposition method to grow ZnO nanorods: Spray pyrolysis. Superlattices and Microstructures, 2007, 42, 444–450.
- [5] T. Dedova, O. Volobujeva, J. Klauson, A. Mere, M. Krunks. ZnO Nanorods via Spray Deposition of Solutions Containing Zinc Chloride and Thiocarbamide. Nanoscale Res Lett., 2007, 2, 391–396.
- [6] L. Guo, S. Yang, C. Yang, P. Yu, J. Wang, W. Ge, G.K.L Wong. Preparation and optical properties. Appl. Phys. Lett., 2000, 76, 2901.
- [7] S. He, M. Zheng, L. Yao, X. Yuan, M. Li, L. Ma, W. Shen. Preparation and properties of ZnO nanostructures by electrochemical anodization method. Applied Surface Science, 2010, 256, 2557–2562.
- [8] M. Krunks, A. Katerski, T. Dedova, I. Oja Acik, A. Mere. Nanostructured solar cell based on spray pyrolysis deposited ZnO nanorod array. Solar Energy Materials & Solar Cells., 2008, 92, 1016–1019.
- [9] Y. Li, G.W. Meng, L.D. Zhang, F. Phillipp. (2000). Appl. Phys. Lett. 76, 2011.
- [10] K. Ravichandran, P. Philominathan. Comparative study on structural and optical properties of CdS films fabricated by three different low-cost techniques. Applied Surface Science, 2009, 255, 5736–5741.
- [11] K. Ravichandran, G. Muruganantham, B. Sakthivel. 2009. Highly conducting and crystalline doubly doped tin oxide films fabricated using a low-cost and simplified spray technique. Physica B. 404, 4299–4302.
- [12] K. Ravichandran, P. Philominathan. Investigations on microstructural and optical properties of CdS films fabricated by a low-cost, simplified spray technique using perfume atomizer for solar cell applications. Solar Energy, 2008, 82, 1062–1066.
- [13] K. Ravichandran, P. Philominathan. Fabrication of antimony doped tin oxide (ATO) films by an inexpensive, simplified spray technique using perfume atomizer. Materials Letters, 2008, 62, 2980–2983.
- [14] Y. Sawada, C. Kobayashi, S. Seki, H. Funakubo. Highly-conducting indium–tin-oxide transparent films fabricated by spray CVD using ethanol solution of indium (III) chloride and tin (II) chloride. Thin Solid Films, 2002, 409, 46–50.
- [15] T. Serin, N. Serin, S. Karadeniz, Sari, N. Tugluoglu, O. Pakma. Journal of Non-Crystalline Solids, 2006 352, 209-215.
- [16] D. Valerini, A.P. Caricato, M. Lomascolo, F. Romano, A. Taurino, T. Tunno, M. Martino.. Appl Phys A 93, 729–733, 2008.

Received: 15.09.2011

NUCLEAR TRANSPARENCY EFFECT IN THE STRONGLY INTERACTING MATTER

M. AJAZ¹, M.K. SULEYMANOV^{1,2}, O.B. ABDINOV³, ALI ZAMAN¹, K.H. KHAN¹,
Z. WAZIR¹, Sh. KHALILOVA³

¹COMSATS Institute of Information Technology, Department of
Physics, Islamabad 44000, Pakistan

²Veksler and Baldin Laboratory of High Energy Physics, JINR,
Dubna 141980, Russia

³H.M. Abdullayev Institute of Physics NAS Azerbaijan Republic, Baku

The work supported by the Science Development Foundation under the President of the Azerbaijan Republic.

We discuss that the results of study of the nuclear transparency effect in nuclear-nuclear collisions at relativistic and ultrarelativistic energies could help to extract the information on new phases of the strongly interacting matter as well as the *QCD* critical point. The results could provide further confirmation of the existence of the "horn" effect which had initially been obtained for the ratio of average values of K^+ - to π^+ -mesons' multiplicity as a function of the initial energies in the *NA49 SPS CERN* experiment. To observe the "horn" as a function of centrality, the new more enriched experimental data are required. The data which are expected from *NICA/MPD JINR* and *CBM GSI* setups could fulfill the requirement.

Keywords: Nuclear transparency effect, strongly interacting matter

PACS: 539.12/17

INTRODUCTION

Search for the new phases of strongly interacting matter as well as the Quantum Chromodynamics (*QCD*) critical point is one of the main objectives of the modern nuclear physics at high energies. Ultrarelativistic heavy ion collisions provide a unique opportunity to create and study the nuclear matter at high densities and temperatures. The produced state will pass different phases of the strongly interacting matter. The effects of: dilepton production; thermal radiation; strangeness enhancement; J/Ψ suppression; jet suppression; flow are considered as possible signatures on the phases of the strongly interacting matter as well as the *QCD* critical point and Quark Gluon Plasma (*QGP*).

Among all other results on ultrarelativistic heavy ion collisions concerning the states of the strongly interacting matter, the results which were obtained by M. Ga'zdicki [1] were more attractive. The paper [1] discussed that the results [2-3] on the energy dependence of hadron production in central *Pb+Pb* collisions at 20, 30, 40, 80 and 158 *A GeV* coming from the energy scan program at the *CERN SPS* serve as evidence for the existence of a transition to the *QGP* [4].

Thus they are in agreement with the conjectures that at the top *SPS CERN* and *RHIC BNL* energies the matter created at the early stage of central *Pb+Pb* and *Au+Au* collisions is in the state of *QGP* [5-6]. The key results are summarized in Fig.1.

The most interesting effect can be seen in the energy dependence of the ratio $\langle K^+ \rangle / \langle \pi^+ \rangle$ of the mean multiplicities of K^+ and π^+ , produced per event in the central *Pb+Pb* collisions, which is plotted in the top panel of the figure. Following a fast threshold rise, the ratio passes through a sharp maximum in the *SPS*

CERN range and then seems to settle to a lower plateau value at higher energies. Kaons are the lightest strange hadrons and $\langle K^+ \rangle$ is equal to about half of the number of all anti-strange quarks produced in the collisions. Thus, the relative strangeness content of the produced matter passes through a sharp maximum at the *SPS CERN* in nucleus-nucleus collisions. This feature is not observed for proton-proton reactions. A second important result is the constant value of the apparent temperature of K^+ mesons in central *Pb+Pb* collisions at low *SPS CERN* energies as shown in the bottom panel of the figure. The plateau at the *SPS CERN* energies is preceded by a steep rise of the apparent temperature at the *AGS BNL* and followed by a further increase indicated by the *RHIC BNL* data.

Very different behavior is measured in proton-proton interactions. Presently, the sharp maximum and the following plateau in the energy of the $\langle K^+ \rangle / \langle \pi^+ \rangle$ ratio has only been reproduced by the statistical dependence model of the early stage [4] in which a first order phase transition is assumed. In this model the maximum reflects the decrease in the number

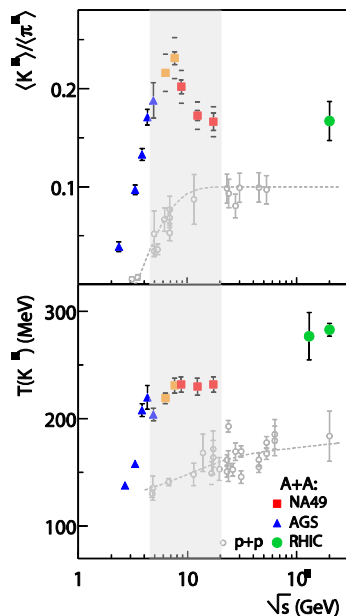


Fig.1. Collision energy dependence of the K^+ -to π^+ -mesons mean multiplicity ratio and the inverse slope parameter of the transverse mass spectra measured in central *Pb+Pb* and *Au+Au* collisions (solid symbols) compared to results from *p+p* reactions (open dots). The changes in the *SPS CERN* energy range (solid squares) suggest the onset of the deconfinement phase

ratio of strange to non-strange degrees of freedom and changes in their masses when deconfinement sets in. Moreover, the observed steepening of the increase in pion production is consistent with the expected excitation of the quark and gluon degrees of freedom. Finally, in the picture of the expanding fireball, the apparent temperature is related to the thermal motion of the particles and their collective expansion velocity. Collective expansion effects are expected to be important only in heavy ion collisions as they result from the pressure generated in the dense interacting matter. The stationary value of the apparent temperature of K^+ mesons may thus indicate an approximate constancy of the early stage temperature and pressure in the *SPS CERN* energy range due to the coexistence of hadronic and deconfined phases, as in the case of the first order phase transition [7-8].

Thus, the anomalies in the energy dependence of hadron production in central $Pb+Pb$ collisions at the low *SPS CERN* energies serve as evidence for the onset of deconfinement and the existence of *QGP* in nature. They are consistent with the hypotheses that the observed transition is of the first order. The anomalies are not observed in $p+p$ interactions and they are not reproduced within hadronic models [9].

These results and their interpretation raise questions which can be answered only by new measurements. The energy region covered by the future measurements at the *SPS CERN* is indicated by the gray band.

THE RESULTS OF THE EXPERIMENTS AT VARIOUS CENTRALITIES

What about the results coming from the experiments at various centralities? Could these experiment indicate the effects same with the Ga'zdicki's key results? Let us now consider some results from these experiments.

During the last several years, some results of the experiments at various centralities (see for example [10]) are discussed. These results demonstrate the point of regime change and saturation on the behavior of some characteristics of the events as a function of the centrality. We believe that such phenomena connected with fundamental properties of

the strongly interacting matter could reflect the changes of its states (phases).

In [11] the variations of average transverse mass of identified hadrons with charge multiplicity have been studied for *AGS BNL*, *SPS CERN* and *RHIC BNL* energies (Fig.2). A plateau was observed in the average transverse mass for multiplicities corresponding to *SPS* energies. It was claimed that it can be attributed to the formation of a coexistence phase of quark gluon plasma and hadrons. So one can say that the central experiments confirm the existence of the plateau for the behaviors of K -mesons' temperature as a function of collisions centrality at the *SPS CERN* energies - the second key result of Ga'zdicki[1].

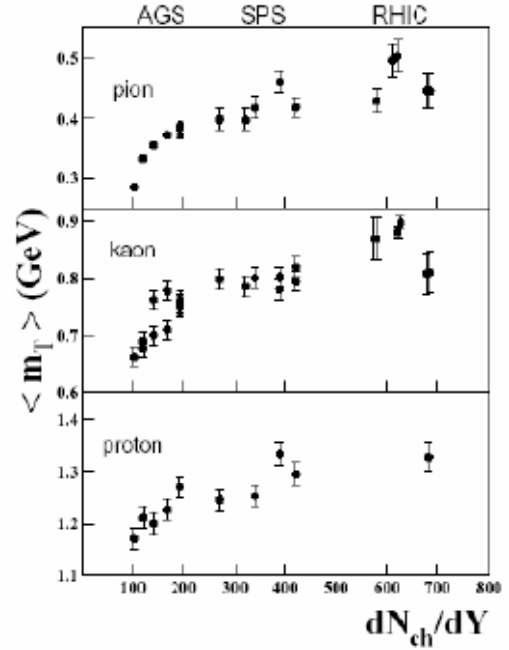


Fig.2. Variation of $\langle m_T \rangle$ with produced charged particles per unit rapidity at mid rapidity for central collisions corresponding to different \sqrt{s} spanning from *AGS BNL* to *RHIC BNL*.

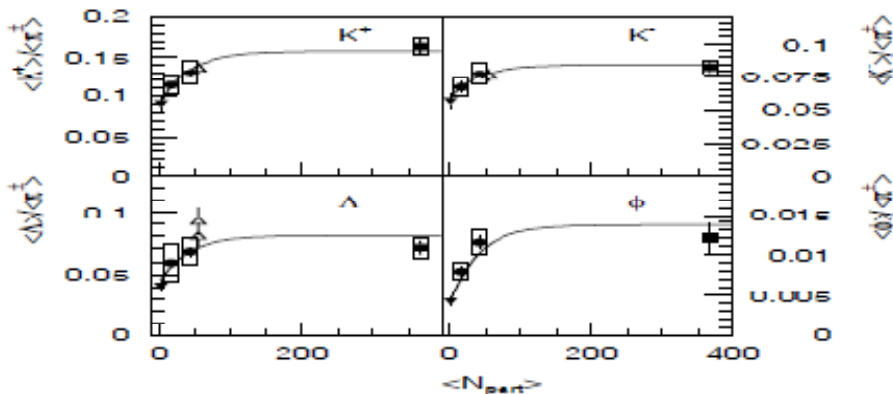


Fig. 3. The experimental ratios of the average values of multiplicity of K^+ , K^- , ϕ -mesons and Λ -hyperons to the average values of multiplicity of π^\pm -mesons as a function of centrality ($\langle N_{part} \rangle$).

Emission of π^\pm , K^\pm , ϕ and Λ was measured in near-central $C+C$ and $Si+Si$ collisions at 158 AGeV beam energy[12]. Together with earlier data for $p+p$, $S+S$ and $Pb+Pb$, the system-size dependence of relative strangeness

production in nucleus-nucleus collisions are shown in Fig.3. Its fast rise and the saturation observed at about 60 participating nucleons can be understood as the onset of the formation of coherent systems of increasing size. So we

could see that the results coming from the central experiments confirmed a fast threshold rise at *AGS BNL* energy range. But these results could not indicate any sharp maximum in the *SPS CERN* range.

So we could say that:

- the experiments at various centralities confirm the existing plateau for the behaviors of *K*-mesons' temperature as a function of collisions centrality at the *SPS CERN* energies - the second key result of Ga'zdziński[1];

- these experiments could indicate the increasing of the ratio $\langle K^+ \rangle / \langle \pi^+ \rangle$ at *AGS BNL* energies - the first key result of Ga'zdziński, but could not show the sharp maximum in the *SPS CERN* range.

We think that the last result could be connected with poorness of the experimental data for the ratio $\langle K^+ \rangle / \langle \pi^+ \rangle$ around of the values $N_{part} \cong 60$. This area could be investigated by increasing the intensity at the points using *NICA/MPD* [13] and *CBM* [14] experiments.

One remark is important that the definition of the centrality is not simple problem because it cannot be defined directly in the experiment. In different experiments the values of the centrality are fixed by different ways. The best way could be to select the events with a maximum number of nucleons - participants in the interaction. To do it, the following criteria are usually used: a number of identified protons, projectiles' and targets' fragments, slow particles, all particles, as the energy flow of the particles with emission angles $\theta \cong 0^\circ$ or with $\theta \cong 90^\circ$. Apparently, it is not simple to compare quantitatively the results on centrality-dependences obtained in literature while on the other hand the definition of centrality could significantly influence the final results. May be this is a reason, why we could not get a clear signal on new phases of strongly interacting matter. That is why it is very important to study the properties of the central collisions and to create some universal criteria to select those events to compare the result coming from different centrality experiments.

NUCLEAR TRANSPARENCY EFFECT TO SEARCH FOR A SIGNAL ON NEW PHASES OF STRONGLY INTERACTING MATTER

New phases of strongly interacting matter (information on the *QCD* critical point) could be identified using the nuclear transparency effect - the behavior of $R = a_{AA}/a_{NN}$ (a_{AA} and a_{NN} are some values of the measured variables in the nuclear-nuclear and proton-proton experiments consequently, for example multiplicity of the charged particles), function at different energies as a function of the centrality. Because the transparency capability of different states of nuclear matter must be different. The investigations could give information on the onset state of the deconfinement as well as on *QCD* critical point.

Using data coming from codes and experimental data on the behavior of R as a function of the centrality it is possible to get information on the appearance of the anomalous nuclear transparency as a signal on changing of the states of strongly interacting matter. Nuclear transparency is one of the effects of nuclear-nuclear collisions from which one may obtain the information about the structure (at low energies), states (at middle energies), properties and phases of the nuclear matter (at relativistic and ultrarelativistic energies). The stated effect is a promising observable to map the transition between the different states/phases of the nuclear medium to the propagation of hadrons.

Transparency depends upon different factors of the events and the collisions:

- (1) Impact parameter of the colliding particles.
- (2) Geometry of projectile and target.
- (3) Mass and size of the projectile and target.
- (4) Diffuseness and density distribution of the projectile and target.
- (5) Energies of the colliding particles.
- (6) Atomic mass number of the target.
- (7) Momentum transfer squared of the projectile.

Now one need to address the important question that how to fix the centrality and how one can study the centrality dependency of the R in the experiment?

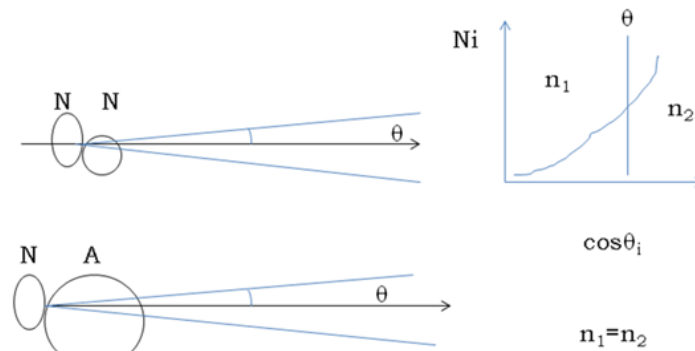


Fig. 4.

In papers [15] the nuclear transparency was used for the analysis of the data coming from the hadron- nuclear experiments. For this aim the authors used the inner cone term which was defined from the *NN* interaction (see Fig.4). The average values of multiplicity of fast particles - *s*-particles (n_s) were defined in the cone with half angle. Then the average values of *s*-particles with emitted angle less then θ were defined in nucleon-nuclear interactions (*NA*) and

studied as a function of the number of the heavy particles - *h*-particles (N_F) emitted in the interactions. The values of the N_F are used to fix the centrality. So there is some possibility to study the properties of the inner cone and outer cone particles produced in an event as a function of the centrality. In this paper they observed that the average multiplicity of inner cone particles did not depend on the centrality. It could be explained as a transparency of the nuclear matter for the

inner particles emitting. The average values of the multiplicity for the outer cone particles increased linearly with N_F . We think that in the boards of different phases of strongly interacting matter the transparency don't change linearly with centrality. This result could be analyzed as a signal on phase transition in the strongly interacting matter. In [16], the effect of "transparency" of nuclear matter in interactions between π^- - mesons and carbon nuclei was investigated at $P_{\pi^-} = 40$ GeV/c. The following are their findings: for all chosen values of the limiting emission angle

$\theta(2.5^\circ, 8^\circ \text{ and } 10^\circ)$ the average multiplicity of the π^- - mesons of the inner cone does not depend on the number of emitted protons (N_p), and for $\theta = 2.5^\circ$ and 8° it coincides with the results for the π^- interactions; the fact that the average multiplicity of the π^+ - mesons of the inner cone is independent of the N_p does not mean total "transparency" of the nucleus to these particles, since their average energy decreases

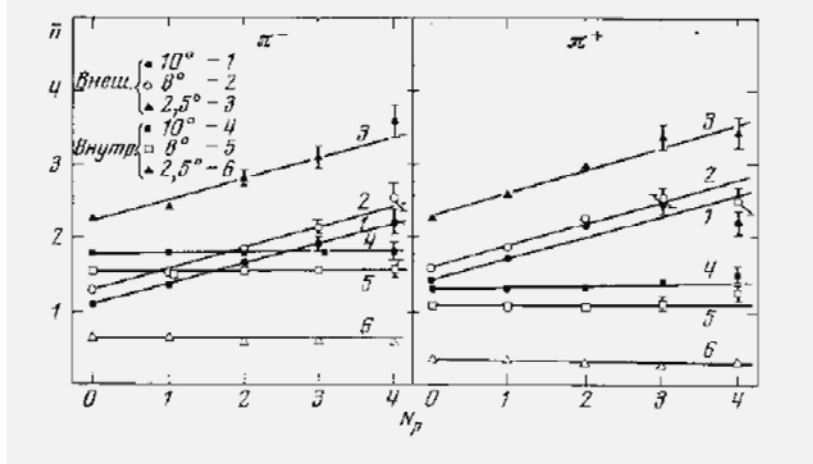


Fig. 5. The average values of multiplicity for π^- (left panel) and π^+ (right panel) - mesons as a function of a number for identified protons in $\pi^{12}\text{C}$ -reactions (lines were drift by hand)

CONCLUSION

The results coming from the central experiments confirm the existing saturation for the behaviors of K -mesons' temperature as a function of collisions centrality at the SPS energies.

These experiments could indicate the increasing of ratio $\langle K^+ \rangle / \langle \pi^+ \rangle$ at AGS energies, but could not show the sharp maximum in the SPS range. The result could be connected

with insufficiency of the experimental points in the region of sharp maximum ($N_{part} \approx 60$).

NICA/MPD and FAIR experiments could get the necessary data to cover the region $N_{part} \approx 60$.

Study of the nuclear transparency effect as a function of the centrality could give an important information of the phases of strongly interacting matter.

We offer to use the inner cone definition to study the nuclear transparency effect as a function of the centrality.

- [1] Marek Gazdzicki. arXiv:nucl-ex/0512034.
- [2] S. V. Afanasiev et al. [The NA49 Collaboration], Phys. Rev. C 66, 054902 (2002).
- [3] M. Ga'zdicki et al. [NA49 Collaboration], J. Phys. G 30, S701(2004).
- [4] M. Ga'zdicki and M. I. Gorenstein, Acta Phys. Polon. B 30, 2705(1999).
- [5] U. W. Heinz and M. Jacob, arXiv:nucl-th/0002042, J. Rafelski and B. Muller, Phys. Rev. Lett. 48, 1066 (1982) [Erratum-ibid. 56, 2334 (1986)], T. Matsui and H. Satz, Phys. Lett. B 178, 416 (1986), F. Becattini, L. Maiani, F. Piccinini, A.D. Polosa and V. Riquer, arXiv:hep-ph/0508188.
- [6] I. Arsene et al. [BRAHMS Collaboration], Nucl. Phys. A 757, 1 (2005), B.B. Back et al., Nucl. Phys. A 757, 28 (2005), J. Adams et al. [STAR Collaboration], Nucl. Phys. A 757, 102 (2005), K. Adcox et al. [PHENIX Collaboration], Nucl. Phys. A 757, 184 (2005).
- [7] M.I. Gorenstein, M. Ga'zdicki and K.A. Bugaev, Phys. Lett. B 567, 175 (2003).
- [8] Y. Hama, F. Grassi, O. Socolowski, T. Kodama, M. Gazdzicki and M. Gorenstein, Acta Phys. Polon. B 35, 179 (2004).
- [9] E.L. Bratkovskaya et al., Phys. Rev. C 69, 054907 (2004), J. Cleymans and K. Redlich, Phys. Rev. C 60, 054908 (1999).
- [10] M.K. Suleymanov et al. Nuclear Physics B (Proc. Suppl.), vol. 177-178, pp. 341-342, 2008.
- [11] B. Mohanty, Jan-e Alam, S. Sarkar, T.K. Nayak, B.K. Nandi. Phys. Rev. C 68, 021901, 2003.
- [12] Alt et al., Phys. Rev. Lett. 94 (2005) 052301.
- [13] <http://nica.jinr.ru/>
- [14] [http://www.gsi.de/fair/experiments/CBM/index\\$_\text{\\\$}_\text{\\\$}.html](http://www.gsi.de/fair/experiments/CBM/index$_\text{\$}_\text{\$}.html)
- [15] P.L. Jain, M. Kazuno, G. Thomas, B. Girard. Phys.Rev.Lett.33,660,1974; J.I.Cohen,E.M. Friedlander et al. Lett.Nuovo Cim., 9,337, 1974.
- [16] A.I. Anoshin et al. Sov. Journal of Nucl. Phys., 27, 5, p.1240-1245, 1978.

Received: 01.09.2011

ON SUPER-HIGH RESOLUTION SPECTROSCOPY OF METASTABLE ATOMS IN ULTRA-THIN GAS CELLS

A.Ch. IZMAILOV^{1*}, Ch.O. QAJAR¹, R.A. KARAMALIYEV²

¹*H.M. Abdullayev Institute of Physics, ANAS, H. Javid av. 33, Baku, Az-1143, Azerbaijan*

²*Baku State University, Z. Khalilov str., 23, Baku, AZ-1148, Azerbaijan*

**e-mail: azizm57@rambler.ru*

We theoretically investigated narrow sub-Doppler resonances in the spectral distribution of a number of atomic particles (atoms or molecules) optically excited in a metastable state in an ultra-thin gas cell with the inner thickness less than or of the order of the wavelength $\lambda \leq 1 \mu\text{m}$ of the monochromatic light wave incident in the normal direction. Thus the regime of coherent Rabi oscillations was considered on the light induced transition from the ground atomic term to the metastable quantum level on the basis of atomic density matrix equations. We analyzed the essential dependence of sub-Doppler resonances (on the center of the optical transition) on the inner thickness and transversal size of a thin gas cell (having the shape of the rectangular parallelepiped) and also on the intensity of the laser radiation. We suggest schemes of possible record of these resonances by methods of absorption, fluorescence and photoionization spectroscopy with use of an additional probe radiation. Investigated resonances may be applied as references in high-accuracy optical frequency standards and for high precision measurements of central frequencies of atomic spectral lines.

Key words: Sub-Doppler resonances, thin gas cell, metastable atoms, frequency stabilization

PACS: 42.62.Fi

1. INTRODUCTION

Development of the high-resolution laser spectroscopy is necessary, in particular, for more detailed analysis of a quantum structure of atoms and molecules [1] and also for creation of more perfect optical frequency standards [2]. Recently non-trivial sub-Doppler resonances have been discovered and investigated, which appear on the central frequencies of the absorption profile of a rarefied atomic sample, contained in a cell with a sufficiently small inner thickness l , when the cell is normally irradiated by a frequency swept monochromatic laser beam with the diameter $D \gg l$ [3-10]. These resonances are the result of the velocity selection of the atoms in definite light-induced quantum states, which are destroyed in the atomic collisions against the cell walls. Thus in papers [3,4], absorption and polarization sub-Doppler resonances were predicted and theoretically investigated, which were caused by the optical pumping of the ground atomic term during transits of atoms in a rarefied gas between walls of a thin gas cell. Later given resonances were detected and analyzed in details at experiments on the precision spectral analysis of cesium atoms in thin cells (with various inner thickness from 10 μm to 1 mm) [5,6]. The paper [7] presents the review of experimentally realized methods of sub-Doppler spectroscopy, which are based on the optical pumping of the ground energetic atomic term in thin gas layer. Quite recently the making of ultra-thin (nanometric) gas cells with the inner thickness much less than the wavelength $\lambda \leq 1 \mu\text{m}$ of the incident optical radiation became possible. Therefore in such cells (with sufficiently rarefied vapors of cesium or rubidium) sub-Doppler absorption and fluorescence resonances, caused by the spectral Dicke narrowing, were detected [8-10].

Mentioned resonances are direct manifestations of the radiative relaxation of the quantum levels and of the corresponding optical coherences. At the same time, it is also important to analyze sub-Doppler spectral structures caused as an effect of velocity selection of atoms (or molecules), when the radiative damping of quantum states is negligible in comparison with their relaxation due to the atomic (or

molecular) collisions with the cell walls. This may take place for many atoms and molecules, if the laser radiation is resonant with a forbidden transition that connects a sublevel of the ground state to a sufficiently long-lived (metastable) level [11]. Very narrow sub-Doppler resonance structures on such quantum transitions may be used as references for high-accuracy optical frequency standards [2].

In paper [12] the theoretical study was conducted on the sub-Doppler resonances in the spectral distribution of a population of metastable atoms excited from the ground atomic term by the monochromatic laser radiation, which is incident (in the normal direction) on a thin cylindrical gas cell. In the subsequent work [13], the possibility was analyzed of using such narrow resonances as references for compact optical frequency standards. Indeed, the total set of excited atoms in a thin gas layer is a compact analog of an atomic beam, the divergence of which is determined by the small ratio l/Q of the internal cell thickness l to its characteristic transversal dimension Q . However, in given theoretical papers [12,13], the fluorescence of atoms was considered only from the narrow paraxial region of a cylindrical cell with a thickness $l \gg \lambda$. Along with this, such fluorescence resonances narrow both with fall of the radiation intensity and decreasing cell dimension ratio l/Q .

Therefore in the present work, we theoretically study narrow sub-Doppler resonances in a spectral distribution of atomic particles excited in a metastable state for the entire volume of an ultrathin gas cell with an internal thickness l less than or of the order of the wavelength $\lambda \leq 1 \mu\text{m}$ of a normal incident monochromatic light wave. It is assumed, that a detection of given resonances is realized by methods of absorption, fluorescence or photoionization spectroscopy by means of an additional probe radiation, connecting the metastable state with other quantum levels of atomic particles. Such narrow sub-Doppler resonances may be applied for the high precision spectral analysis of a quantum structure of atomic particles and also as effective references for high-accuracy optical frequency standards.

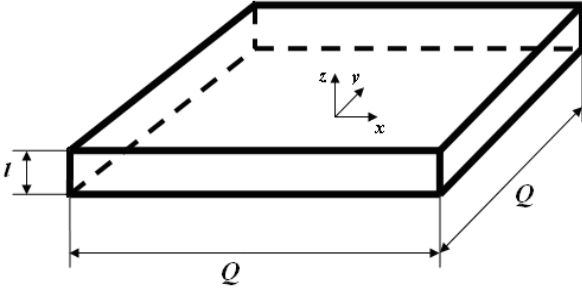


Fig.1. The gas cell having the shape of the rectangular parallelepiped, with the small thickness $l \ll Q$.

In the present work we consider the gas cell having the shape of the rectangular parallelepiped (Fig.1), because analytical and numerical calculations essentially simplify in this case. However, it is obvious that obtained qualitative results are valid also for thin cells of another shapes (for example in case of a cylindrical cell with the diameter $Q \gg l$ and inner thickness l).

2. BASIC RELATIONSHIPS

Let us consider a rarefied gas medium in the cell made to the shape of the rectangular parallelepiped (Fig.1) from a transparent material. The inner thickness l of this cell (along the axis z) is much less than its transversal size Q (along axes x and y). It is assumed, that the following stationary plane monochromatic light wave incidents on the gas cell (Fig.1) along the axis z with the homogeneous intensity on the cell volume:

$$A(z,t) = 0.5E \cdot \exp[i(\omega t - kz)] + \text{c.c.}, \quad (1)$$

where $\mathbf{E} = E\mathbf{e}$, E and \mathbf{e} are, respectively, the amplitude and unit polarization vector of the radiation, ω is the frequency, $k = \omega/c = 2\pi/\lambda$, λ is the wavelength. The radiation frequency ω is close to the center ω_0 of the electric dipole transition $a \rightarrow b$ between the sublevel a of the ground term and the excited long-lived (metastable) state b of atomic particles (atoms or molecules). The sufficiently rarefied gas medium in the cell is considered, when an interaction between particles is negligible. We also do not take into account light pressure effects on atomic particles. We will analyze the situation when the lifetime of the excited level b is much longer than the characteristic transit time Q/u of particles across the cell (Fig.1) with their most probable speed u in the gas. Therefore we will not take into account the radiative relaxation of the excited level b .

Let us consider the linear polarization \mathbf{e} of the wave (1) and neglect an effect of an external magnetic field on optical processes in the cell. Then this wave (1) will interact with a collection of independent electric dipole transitions $am \rightarrow bm$ between Zeeman sublevels am and bm of levels a and b (having total angular momenta j_a and j_b respectively) with an equal momentum projection m on the quantization axis along the polarization vector \mathbf{e} [1]. Under given conditions, we may write the following system of equations for elements of the density matrix of the optical coherence $\rho_{mm}^{(ab)}$ and populations $\rho_m^{(a)}$ and $\rho_m^{(b)}$ of

sublevels am and bm [14] for each possible value of the magnetic quantum number m :

$$\begin{aligned} \rho_m^{(a)} + \rho_m^{(b)} &= \frac{n_a^{(0)}}{(2j+1)} \cdot \tilde{F}(\mathbf{v}), \\ \frac{\partial \rho_m^{(b)}}{\partial t} + \mathbf{v} \cdot \frac{\partial \rho_m^{(b)}}{\partial \mathbf{r}} &= -0.5i g_m \rho_{mm}^{(ab)*} \exp[i(\delta t - kz)] + \text{c.c.}, \\ \frac{\partial \rho_{mm}^{(ab)}}{\partial t} + \mathbf{v} \cdot \frac{\partial \rho_{mm}^{(ab)}}{\partial \mathbf{r}} &= 0.5i g_m (\rho_m^{(b)} - \rho_m^{(a)}) \exp[i(\delta t - kz)] \end{aligned} \quad (2)$$

where $n_a^{(0)}$ is the equilibrium density of atoms in the ground state a (in the absence of the light wave), $\tilde{F}(\mathbf{v})$ is the Maxwell distribution on a velocity \mathbf{v} of particles, j is the minimum among angular momenta j_a and j_b , $g_m = (E d_m)/\hbar$ is the Rabi frequency and d_m is the matrix element of the dipole moment for the transition $am \rightarrow bm$, $\delta = (\omega - \omega_0)$ is the frequency detuning.

Eqs.(2) must be supplemented by boundary conditions, which depend on features of particles collisions with walls of the cell. According to previous investigations for thin gas cells [4-7,12], we may assume that the equilibrium distribution for both particles velocities and populations of their quantum states are established due to such collisions (in particular elements of density matrix $\rho_m^{(b)}$ and $\rho_{mm}^{(ab)}$ vanish).

As a result of solving of Eqs.(2) with mentioned boundary conditions, we obtain the following expression for the population $\rho_m^{(b)}$ of atomic particles on a metastable Zeeman sublevel bm in the gas cell (Fig.1) restricted by 6 walls with coordinates $z = \pm 0.5l$, $x = \pm 0.5Q$ and $y = \pm 0.5Q$:

$$\begin{aligned} \rho_m^{(b)}(\mathbf{r}, \mathbf{v}) &= \eta(0.5l - |z|) \cdot \eta(0.5Q - |x|) \cdot \eta(0.5Q - |y|) \times \\ &\times \sum_{\alpha=\pm 1} \sum_{\beta=\pm 1} \sum_{\sigma=\pm 1} \eta(\alpha \cdot v_x) \cdot \eta(\beta \cdot v_y) \cdot \eta(\sigma \cdot v_z) \times \\ &\times \left\{ \tilde{\rho}_m^{(b)} \left[\frac{0.5Q + \alpha x}{|v_x|} \right] \cdot \eta \left[\frac{(0.5Q + \beta y)}{|v_y|} - \frac{(0.5Q + \alpha x)}{|v_x|} \right] \times \right. \\ &\times \eta \left[\frac{(0.5l + \sigma z)}{|v_z|} - \frac{(0.5Q + \alpha x)}{|v_x|} \right] + \tilde{\rho}_m^{(b)} \left[\frac{(0.5Q + \beta y)}{|v_y|} \right] \times \\ &\times \eta \left[\frac{(0.5Q + \alpha x)}{|v_x|} - \frac{(0.5Q + \beta y)}{|v_y|} \right] \cdot \eta \left[\frac{(0.5l + \sigma z)}{|v_z|} - \right. \\ &\left. \left. - \frac{(0.5Q + \beta y)}{|v_y|} \right] + \tilde{\rho}_m^{(b)} \left[\frac{0.5l + \sigma z}{|v_z|} \right] \cdot \eta \left[\frac{(0.5Q + \alpha x)}{|v_x|} - \right. \right. \end{aligned}$$

$$-\frac{(0.5l+\sigma z)}{|v_z|} \cdot \eta \left[\frac{(0.5Q+\beta y)}{|v_y|} - \frac{(0.5l+\sigma z)}{|v_z|} \right] \Bigg\}, \quad (3)$$

where

$$\tilde{\rho}_m^{(b)}(\xi) = \frac{n_a^{(0)}}{(2j+1)} \tilde{F}(\mathbf{v}) \times \frac{g_m^2 \cdot \sin^2 \left\{ 0.5\xi \cdot [g_m^2 + (\delta - kv_z)^2]^{1/2} \right\}}{[g_m^2 + (\delta - kv_z)^2]}, \quad (4)$$

and $\eta(x)$ is the step function ($\eta(x)=1$ if $x \geq 0$ and $\eta(x)=0$ if $x < 0$).

The total number N_b of particles on the excited (metastable) level b with all possible velocities in the whole volume V of the cell (Fig.1) is determined by the relationship:

$$N_b = \sum_{m=-j}^j \int \left[\int_V \rho_m^{(b)}(\mathbf{r}, \mathbf{v}) d^3\mathbf{r} \right] d^3\mathbf{v}, \quad (5)$$

where the population $\rho_m^{(b)}$ is determined by formulas (3) and (4).

It is assumed that a detection of a spectral distribution of metastable atomic particles $N_b(\delta)$ (5) is carried out by means of an additional probe radiation, which induces transition of given particles from the metastable level b to other quantum states. This stable radiation may be broadband and generated even by a noncoherent source in such a direction in order to irradiate all volume of the gas cell (Fig.1). We also suppose that the given weak probe radiation does not cause nonlinear optical effects. Under these conditions, a spectral distribution $N_b(\delta)$ (5) may be directly recorded in the absorption of the probe radiation and also in the corresponding induced fluorescence or photoionization of atomic particles. Therefore further we will carry out analysis of a number of excited (metastable) particles N_b (5) versus the frequency detuning δ and intensity of the stationary monochromatic light radiation (1) and also versus sizes l and $Q \gg l$ of an ultra-thin gas cell (Fig.1).

3. DISCUSSION OF RESULTS

On the basis of analytical relationships, obtained in the previous section, now we will carry out numerical calculations on example of spectroscopic data of the intercombination transition $^1S_0 - ^3P_1$ (with the wavelength $\lambda = 657$ nm) of calcium atoms from the ground state 1S_0 to the metastable level 3P_1 with full angular momenta 0 and 1 respectively [11].

At the linear polarization of the laser radiation (1), only the light induced transition between two Zeeman states of levels 1S_0 and 3P_1 with the magnetic quantum number $m=0$ are realized.

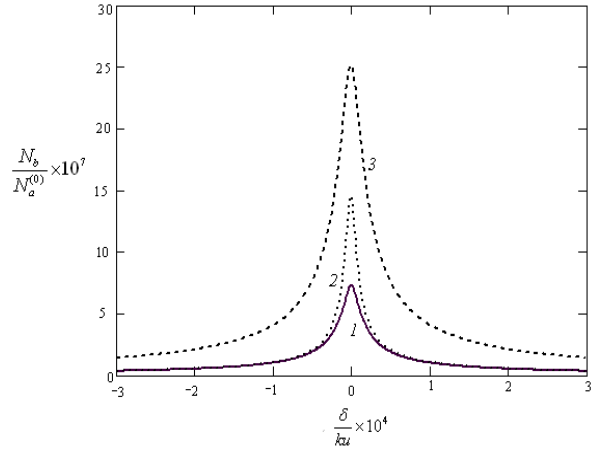


Fig.2. The number N_b of metastable atoms (in the whole volume of the cell) versus the frequency detuning $\delta = (\omega - \omega_0)$ of the monochromatic radiation, when $g/(ku) = (1, 2) 2.8 \cdot 10^{-6}$ and (3) $5.6 \cdot 10^{-6}$, $Q = (1, 3)$ 20 mm and (2) 50mm, $l = 0.5\lambda$, $\lambda = 657$ nm.

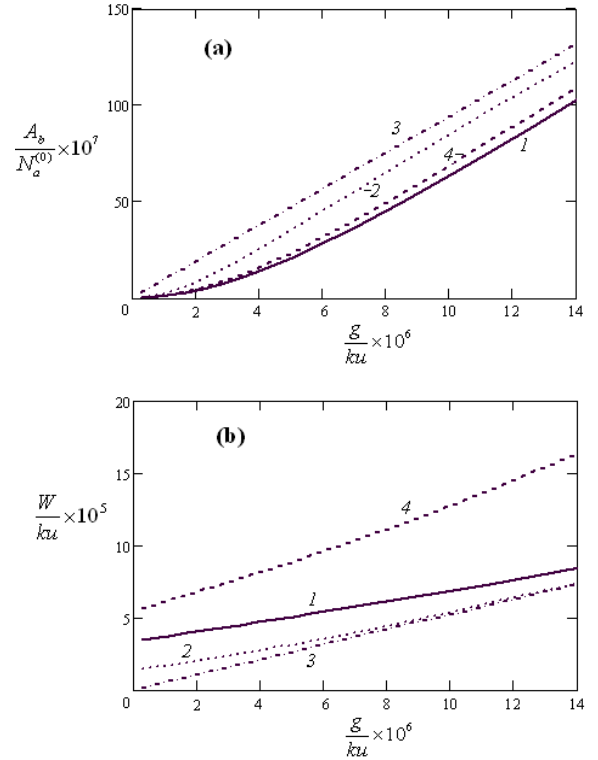


Fig.3. The amplitude A_b (a) and width W (b) of the resonance (Fig.2) versus the Rabi frequency g , when $l = (1-3) 0.5\lambda$ and (4) λ , $Q = (1, 4)$ 20 mm, (2) 50mm and (3) ∞ , $\lambda = 657$ nm.

Therefore further we will use the denotation $g = g_{m=0}$ for the corresponding Rabi frequency in formulas (2)-(4). It will be assumed at numerical estimations, that the most probable speed of calcium atoms $u \approx 545$ m/s, which takes place at the temperature of the calcium vapor about 440°C . Then the characteristic density of calcium atoms $n_a^{(0)} \approx 10^{12}$ atoms/cm³ and the collision free mean path is longer than 1 m [2].

In the regime of coherent Rabi oscillations on the resonance transition $a \rightarrow b$ under consideration, an effective excitation to the metastable state b is realized in the gas cell for atoms whose velocity projections on axes x , y , and z (Fig.1) satisfy conditions:

$$gl > |v_z|, \quad gQ > |v_x|, \quad gQ > |v_y|. \quad (6)$$

Narrow and sharp resonance dependences in Fig.2 with the center in the point $\delta = 0$ present spectral distributions of a number of atoms $N_b(\delta)$ in the excited (metastable) state b for ultra-thin gas layers with the thickness $l=0.5\lambda$. This value N_b is normalized on the number of atoms $N_a^{(0)} = n_a^{(0)} \cdot V$ on the ground quantum level a in the whole volume $V = l \cdot D^2$ of the gas cell (Fig.1) in the absence of the light wave (1). We see that, for sufficiently low intensities of the laser radiation (1), the characteristic width W , defined as the full width at the half maximum, of such a resonance $N_b(\delta)$ is about by five orders of magnitude smaller than the characteristic Doppler broadening ku of the atomic gas in the cell.

Increasing the laser radiation intensity (1) leads to rise both the amplitude $A_b = N_b(\delta=0)$ and the width W of the resonance $N_b(\delta)$ (Figs.2 and 3). Curves 3 in Fig.3 correspond to the limit of the plane one-dimensional gas cell, when its transversal size $Q \rightarrow \infty$. In fact, linear dependences of the amplitude A_b and the width W of the resonance on the Rabi frequency g are characteristic for this case. Indeed, according to conditions (6) for the one-dimensional cell, an effective excitation to the metastable state b takes place for atoms with longitudinal velocity projections $|v_z| \leq gl$. For the Doppler broadened spectral line of the resonance transition $a \rightarrow b$, such an excitation takes place in the interval $|\delta| < 2g(kl)$ of the frequency detuning $\delta = (\omega - \omega_0)$. Thus, for the curve 3 in Fig.3b, the width $W(g) \approx (5/3) g(kl)$. Rise of an excited atoms number with velocity projections $|v_z| \leq gl$ at the increase of the Rabi frequency g leads to the linear dependence also for the corresponding resonance amplitude A_b in the case of the one-dimensional cell (curve 3 in Fig.3a). For an effective excitation of atoms to the metastable state b in a gas cell with real transversal sizes (Fig.1), it is necessary to satisfy simultaneously three conditions (6) for atomic velocity projections. Therefore, a relative number $A_b/N_a^{(0)}$ of excited atoms for real gas cells is essentially less than for the corresponding limit of the one-dimensional cell at sufficiently low Rabi frequencies (Fig.3a). It is important to note, that at the finite transversal cell size Q in the limit of the very low Rabi frequency $g \rightarrow 0$, the width W approaches to a nonzero limitary value (Fig.3b), unlike the amplitude A_b of the resonance (Fig.3a). Indeed in real gas cells, the width W is determined not only by the mentioned light field

broadening $\sim g(kl)$ but also by the time-of flight broadening $\sim (u/Q)$ and by the residual Doppler broadening $\sim ku(l/Q)$. Thus for curves 1, 2 and 4 in Fig.3b, the width W in the limit $g \rightarrow 0$ is sufficiently close to the sum of corresponding broadenings $[2(u/Q) + ku(l/Q)]$. Rise of the laser radiation intensity (1) leads to an amplification of the light field broadening $\sim g(kl)$. As a result, curves 1-3 in Fig.3b, obtained for gas cells with an equal thickness l but with different transversal sizes Q (Fig.1), asymptotically approach to the same linear dependence $W(g) \approx (5/3) g(kl)$ at the growth of the Rabi frequency g .

Fig.4 presents dependences of the amplitude A_b and width W of an sub-Doppler resonance

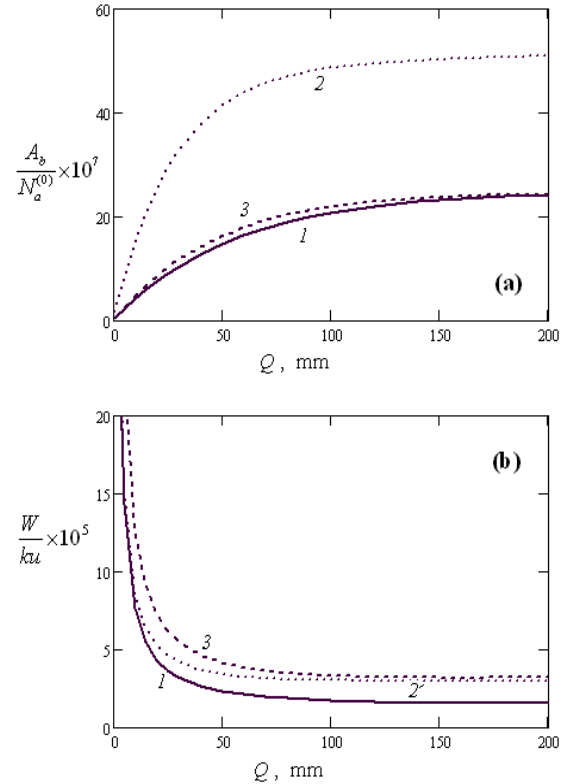


Fig.4. The amplitude A_b (a) and width W (b) of the resonance (Fig.2) versus the transversal size Q of the gas cell (Fig.1), when $g/(ku)=(1,3) \cdot 2.8 \cdot 10^{-6}$ and (2) $5.6 \cdot 10^{-6}$, $l=(1,2) \cdot 0.5 \lambda$ and (3) $\lambda, \lambda=657 \text{ nm}$.

$N_b(\delta)$ (Fig.2) on the transversal size Q of the cell (Fig.1) at its fixed inner thickness l . According to conditions (6), given values A_b and W asymptotically approach to the limit of the plane one-dimensional cell at increase of the size Q when $Q \gg u/g$. In particular, curves 2 and 3 in Fig.4b, obtained for different values of thicknesses l and Rabi frequencies g but at their equal product gl , approach to the same value of the width $W \sim g(kl)$ with rise of the size Q . In the region of relatively small values of $Q \ll u/g$, the width $W \sim Q^{-1}$ (Fig.4b) because then it is determined mainly by the time-of-flight broadening $\sim (u/Q)$ and by the residual Doppler broadening $\sim ku(l/Q)$.

Fig.5 presents dependences of the amplitude A_b and width W of an sub-Doppler resonance $N_b(\delta)$ (Fig.2) on the inner thickness l of the cell (Fig.1) in the nanometric region, when $0 < l < 1 \mu\text{m}$. Narrowing of the gas cell leads to decrease both values A_b and W .

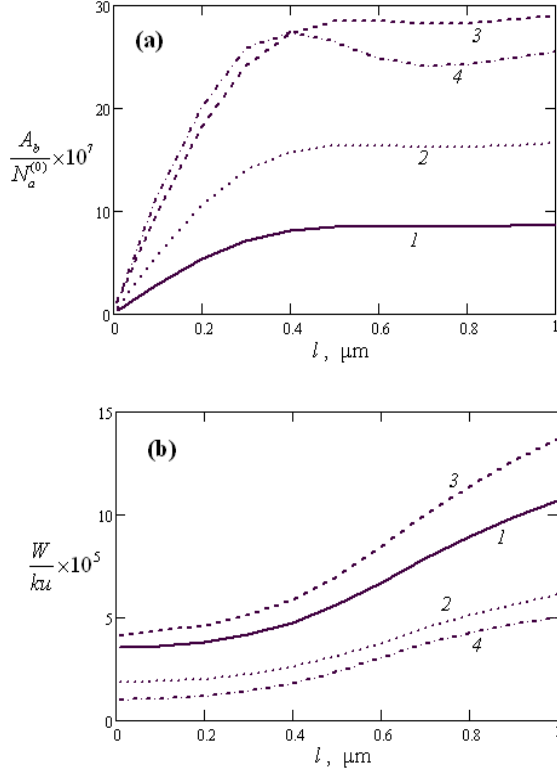


Fig.5. The amplitude A_b (a) and width W (b) of the resonance (Fig.2) versus the inner thickness l of the gas cell, when $g/(ku)=(1,2,4) \cdot 2.8 \cdot 10^{-6}$ and (3) $5.6 \cdot 10^{-6}$, $Q=(1,3) 20 \text{ mm}$, (2) 50 mm and (4) ∞ , $\lambda=657 \text{ nm}$.

However, unlike the amplitude A_b (Fig.5a), in the limit $l \rightarrow 0$, the width W approaches to a nonzero value (Fig.5b) because of the light field broadening and time-of-flight broadening of resonances under study. Thus, in the approximation of the one-dimensional cell, such a limitary width W is caused directly by the light field broadening and is determined by the Rabi frequency g (curve 4 in Fig.5b). We note relatively weak dependence of the width W on the gas layer thickness l at sufficiently small values $l \leq k^{-1}$. However the dependence $W(l)$ amplifies in the region $l > k^{-1}$ (Fig.5b), when the light field broadening is determined by the value $g(kl) > g$ and the residual Doppler broadening $\sim ku(l/Q)$ is essential in comparison with the time-of-flight broadening $\sim (u/Q)$. On the contrary, the relative amplitude $A_b/N_a^{(0)}$ rises (starting from the zero value) at the growth of the cell thickness in the interval $l < k^{-1}$ and tends to saturation when $l \gg k^{-1}$. Indeed, if $l \gg k^{-1}$, then many Rabi oscillations will occur between ground and metastable levels of the resonance transition

$a \rightarrow b$ during transit times of atoms between nearest plane-parallel walls of the gas cell (Fig.1). We note that Rabi oscillations may display also as some variations in dependence of the amplitude A_b on the cell thickness l (curve 4 in Fig.5a).

Thus investigated sub-Doppler resonances (Fig.2) narrow at a fall of the laser radiation intensity (1) and also with rise of the transversal size Q of the cell and with decrease of its inner thickness l (Fig.1). At rise of the transversal size Q , also growth of the resonance amplitude A_b takes place (Fig.4a). However, in practice, the value Q is restricted by a transversal size of a real laser beam and, as a rule, is not more than a few centimeters. Therefore, for detection of the most narrow sub-Doppler resonances under consideration with not too small amplitudes, according to obtained dependences (Figs.2-4), it is reasonable to select such an intensity of the laser beam and thickness l of the gas layer when $g \sim (u/Q)$ and $l \sim k^{-1} = 0.5 \lambda / \pi$.

4. CONCLUSIONS

We have carried out numerical analysis on the example of the intercombination transition $^1S_0 - ^3P_1$ (with the wavelength $\lambda = 657 \text{ nm}$) of calcium atoms. However obtained qualitative results are valid also for any optical transition from the ground quantum term to a metastable level not only atoms but also molecules.

Detection of sub-Doppler resonances under consideration (Fig.2) may be realized by a sufficiently weak stable radiation, which connects the optically excited metastable level with another atomic quantum state, having the negligible population. For example, in the considered case of calcium atoms, following optical transitions may be used for such photoprocesses: $(4s4p)^3P_1 \rightarrow (4s5s)^1S_0$ at 552.1 nm or $(4s4p)^3P_1 \rightarrow (4p2)^3P_0$ at 430 nm [11, 13]. Our sub-Doppler resonances may display both in the absorption of the probe radiation and in a fluorescence of atomic particles induced by this radiation. Indeed, if the sufficiently weak probe radiation irradiates the all volume of the thin cell and does not cause nonlinear optical effects, then corresponding absorption and fluorescence signals will be proportional to the investigated distribution $N_b(\delta)$ (as in fig.2) of metastable atoms versus the scanned frequency detuning $\delta = (\omega - \omega_0)$ of the monochromatic pumping radiation (1). For detection of given resonances, also methods of photoionization spectroscopy may be used, which are based on a resonance ionization of atoms (or molecules) at successive absorption of several photons [15]. Such photoionization methods are characterized by the extremely high sensitivity (up to single atoms or molecules) which may combine with the high spectral resolution. For realization of corresponding spectral measurements in our case, it is necessary to use probe radiation with a frequency sufficient for the photoionization of atomic particles from the excited (metastable) state b but not from the ground energetic level a .

For an effective detection of relatively weak sub-Doppler resonances under study on a possible noise background (connected, for example, with a scattering of the probe radiation), it is better to record directly the difference between (absorption, fluorescence or photoionization) signals

with monochromatic laser radiation (1) and without this radiation. Moreover, the removal of an influence of a relatively broadband noise background is possible by means of the frequency modulation technique [1,2] for the monochromatic radiation (1), when narrow resonances of frequency derivatives of corresponding dependences $N_b(\delta)$ (Fig.2) are recorded.

A cell standard based on forbidden transitions (in particular for various alkali-earth atoms *Ca*, *Mg*, *Ba* and *Yb*) would be of great relevance, because these transitions are the most promising as references for optical atomic clocks now under development [2]. The sub-Doppler resonances in ultra-

thin gas cells, investigated in the present work, may be used as such effective references for compact high-accuracy optical frequency standards. Moreover, on the basis of given most narrow resonances, it is possible to raise the measurement precision of central frequencies of Doppler broadened spectral lines. This may lead to a more accurate determination of fundamental constants in atomic physics, connected with such measurements [1].

This work was supported by the Science Development Foundation under the President of the Republic of Azerbaijan (grant EIF-2010-1(1)-40/02-1).

-
- [1] *W. Demtröder*, Laser Spectroscopy: Basic Concepts and Instrumentation (Springer, Berlin, 2003).
 - [2] *F. Riehle*, Frequency Standards-Basics and Applications (Wiley-VCH, Berlin, 2004).
 - [3] *A.Ch. Izmailov*, Laser Phys. 2(5), 762-763 (1992).
 - [4] *A.Ch. Izmailov*, Opt. and Spectrosc. 74(1), 25-29 (1993).
 - [5] *S. Briaudeau, D. Bloch, and M. Ducloy*, Europhys. Lett. 35(5), 337-342 (1996).
 - [6] *S. Briaudeau, D. Bloch, and M. Ducloy*, Phys. Rev. A59(5), 3723-3735 (1999).
 - [7] *A.Ch. Izmailov*, Proc. of SPIE 6727, 67270B (2007).
 - [8] *G. Dutier, A. Yarovitski, S. Saltiel, A. Papoyan, D. Sarkisyan, D. Bloch*, Europhys. Lett. 63(1), 35-41, (2003).
 - [9] *K. Vaseva, P. Todorov, S. Cartaleva, D. Slavov and S. Saltiel*. Acta Physica Polonica. 116(4), 573-575 (2009).
 - [10] *S. Cartaleva, S. Saltiel, A. Sargsyan, D. Sarkisyan, D. Slavov, P. Todorov and K. Vaseva*. J. Opt. Soc. Am. 26(11), 1999-2006 (2009).
 - [11] *A.A. Radtsig and B.M. Smirnov*. Reference Data on atoms, molecules and ions (Springer, New York, 1985).
 - [12] *N. Beverini, A.Ch. Izmailov*. Optics Commun. 282, 2527-2531 (2009).
 - [13] *N. Beverini, A.Ch. Izmailov*. Proc. EFTF-IFCS 2009 Joint Conference, 1030-1034 (Besanson, 2009).
 - [14] *S.G. Rautian and A.M. Shalagin*. Kinetic Problems of Nonlinear Spectroscopy (North-Holland, 1991).
 - [15] *V.S. Letokhov*. Laser Photoionization Spectroscopy (Academic Press, Orlando, 1987).

Received: 07.07.2011

LIFETIME OF POLARON EXCITED STATE IN SINGLE-SHELL NANOTUBE

O.Z. ALEKPEROV, S.M. SEID-RZAYEVA, S.S. GUSEYNOVA

*H.M. Abdullayev Institute of Physics of Azerbaijan National Academy of Sciences
AZ-1143, G.Javid ave., 33, Baku, Azerbaijan*

The task about energy relaxation of nonequilibrium electrons in single-shell semiconductor nanotube (NT) with radiation of optical phonon at low temperatures has been solved. The general analytical expressions of energy relaxation time (polaron lifetime in excited state) for ratio arbitrary value of NT radius to polaron radius r_0/r_p . The theoretical calculation of polaron lifetime in excited state with taking into consideration intrasubband and intersubband transitions of dimensional quantization for semiconductor NT has been carried out.

Key words: Nanotube, electron-phonon interaction, polaron, relaxation.

PACS: 539.29;539.216.1

1. INTRODUCTION

Nowadays the big attention is given to creation and investigation of low-dimensional systems. The nanotubes (NT): carbonic NT or folded quantum wells of semiconductor compounds A^3B^5 obtained on Prince technology is of big interest among the investigation objects in the given field [1]. The modern technologies allow us to obtain the perfect NT of different sizes from different materials [2,3].

The electron properties of NT are the object of intensive investigation in the physics of low-dimensional systems. The interaction of electrons with long-wave optical (LO) phonons plays the dominating role in the definition of electron, optical and acoustic properties of semiconductor NT.

The task solution about energy relaxation of nonequilibrium electrons put into higher subbands is connected with electron-phonon interaction. The energy losses by electron being in excited state are known as electron energy relaxation. Moreover, energy losses are defined by both the velocity with which the energy is lost by electron because of LO-phonon emission and the velocity with which the electron has the energy because of phonon absorption.

At low temperatures the velocity of electron energy loss in polar semiconductor is mainly defined by the velocity with which the energy is lost by electron because of LO-phonon emission without absorption one. The frequency of their transitions into lower states with radiation of optical phonon is the main parameter defining the energy relaxation velocities of nonequilibrium electrons.

The transition frequency with optical phonon radiation is calculated in quantum wells for nonequilibrium electrons in [4,5,6]. The time necessary for energy relaxation of nonequilibrium electrons is calculated in semiconductor quantum point in [7]. In generated semiconductor InAs the experimentally

obtained value of polaron lifetime [8] approximately is equal to 0,53ps and this value coincides with results of theoretical calculations.

In order to define the peculiarities of energy relaxation processes of nonequilibrium electrons in NT at low temperatures, one need to carry out the theoretical calculation of transition frequency of nonequilibrium electrons with taking into consideration both the intrasubband and intersubband transitions of dimensional quantization.

The obtaining of general analytical expressions for both intrasubband and intersubband transitions at arbitrary value of NT radius ratio to polaron radius r_0/r_p .

2. THE POLARON ENERGY RELAXATION TIME IN EXCITED STATE

Let's consider the energy relaxation processes of nonequilibrium electrons at low temperatures because of radiation of LO-phonon in NT (in hollow cylinder). Let's the two-dimensional gas of nonequilibrium excited electrons formed by the way of injection or photo-excitation exists on the surface of hollow cylinder. The electron transition from excited high-energy state to low-energy ones can be carried out: a) in the limits of the given subband which are intrasubband transitions or b) from the given subband taking into consideration the transitions to neighbor subbands which are intersubbands ones.

Moreover, for the definition of energy relaxation velocity of nonequilibrium electrons one needs to calculate the frequency of intrasubband and intersubband transitions.

According to [5,7] the transition frequency $1/\tau_{n,k}$ for electron with wave vector \vec{k} of upper excited level n with LO-phonon radiation is defined by the expression:

$$\frac{1}{\tau_{n,k}} = \frac{2\pi}{\hbar} \sum_{n',q} |M_{nk, n'k-q}|^2 \delta(\varepsilon_{n,k} - \varepsilon_{n',k-q} - \hbar\omega_L). \quad (1)$$

Here matrix element $M_{nk, n'k-q}$ on excitation energy $(-e \sum_{\vec{q}} \Phi_{\vec{q}})$ corresponds to electron-phonon interaction [9] with limit frequency ω_L . According to results of work [9] the quantum energy spectrum $\varepsilon_{n,k}$ and electron normalized wave function $\psi_{nk}(z, \varphi)$ is given in the form:

$$\varepsilon_{n,k} = \frac{\hbar^2 k^2}{2m} + \frac{\hbar^2 n^2}{2mr_0^2}, \quad (2)$$

$$\psi_{nk}(z, \varphi) = \frac{1}{\sqrt{2\pi L}} e^{i(kz + n\varphi)}. \quad (3)$$

In (2) and (3) m is electron effective mass, r_0 is cylinder radius, φ and z are cylinder coordinates, L is cylinder height, $n = 0, \pm 1, \pm 2, \dots$ are numbers of subband dimensional quantization. The quasi-impulse $\hbar \vec{k}$ corresponds to electron movement on the cylinder surface along z axis. Taking into consideration the expression for scalar potential $\Phi_{\vec{q}}$ [9] and using (2), (3) after

integration on φ и z for matrix element $M_{n-n', \vec{q}}$ we obtain:

$$M_{n-n', \vec{q}} = i \hbar \omega_L \sqrt{\frac{4\pi\alpha r_p}{V}} \frac{J_{n-n'}(q_{\perp} r_0)}{\sqrt{q_{\perp}^2 + q_z^2}},$$

where $J_{n-n'}(q_{\perp} r_0)$ is Bessel function with index $n-n'$; q_{\perp} , q_z are transversal and longitudinal projections of phonon wave vector $\vec{q}(q_{\perp}, q_z)$, the bond constant of electron-phonon interaction α and polaron radius r_p is defined by expressions:

$$\alpha = \sqrt{\frac{m}{2\hbar\omega_L}} \frac{e^2}{\hbar} \left(\frac{1}{\varepsilon_{\infty}} - \frac{1}{\varepsilon_0} \right), \quad r_p = \sqrt{\frac{\hbar}{2m\omega_L}},$$

where ε_0 and ε_{∞} are static and high-frequency dielectric constants.

Transiting from summation to integration in (1) in cylinder coordinates q_{\perp} , q_z , φ and making the integration on polar angle φ we obtain:

$$\frac{1}{\tau_{n,k}} = \frac{2\alpha}{\hbar} (\hbar\omega_L)^2 r_p \int_0^{\infty} \int_{-\infty}^{\infty} \sum_{n'} \frac{|J_{n-n'}(q_{\perp} r_0)|^2}{(q_{\perp}^2 + q_z^2)} \delta \left(\frac{\hbar^2 q_z^2}{2m} + \frac{\hbar^2}{m} q_z k - \frac{\hbar^2 (n^2 - n'^2)}{2mr_0^2} + \hbar\omega_L \right) q_{\perp} dq_{\perp} dq_z. \quad (4)$$

Introducing the following dimensionless variables: $x = r_p q_{\perp}$, $z = r_p q_z$, $\kappa = r_p k$, $a = r_0/r_p$ and also taking into consideration the designation $b_{nn'} = \sqrt{1 - (n^2 - n'^2) a^{-2}}$ we obtain for (4) the following expression:

$$\frac{1}{\tau_{n,\kappa}} = 2\alpha\omega_L \sum_{n'} \int_0^{\infty} \int_{-\infty}^{\infty} \frac{|J_{n-n'}(xa)|^2}{(x^2 + z^2)} \delta(z^2 + 2z\kappa + b_{nn'}^2) x dx dz. \quad (5)$$

The integration in (5) on variable x gives the following result:

$$\frac{1}{\tau_{n,\kappa}} = 2\alpha\omega_L \sum_{n'} \int_{-\infty}^{\infty} I_{n-n'}(az) K_{n-n'}(az) \delta(z^2 + 2z\kappa + b_{nn'}^2) dz, \quad (6)$$

here $I_{n-n'}(az)$, $K_{n-n'}(az)$ are modified Bessel functions of first and second order [10], correspondingly.

Making the integration in (6) on z for polaron lifetime we obtain the analytical expression of the following form:

$$\frac{1}{\tau_{n,\kappa} \alpha \omega_L} = \sum_{n'} \frac{\theta(\kappa^2 - b_{nn'}^2)}{\sqrt{\kappa^2 - b_{nn'}^2}} [I_{n-n'}(a|z_1|) K_{n-n'}(a|z_1|) + I_{n-n'}(a|z_2|) K_{n-n'}(a|z_2|)] \quad (7)$$

Here $z_{1,2} = -\kappa \pm \sqrt{\kappa^2 - b_{nn'}^2}$ are the roots of the argument of Dirac function $\delta(z^2 + 2z\kappa + b_{nn'}^2)$, $\theta(\kappa^2 - b_{nn'}^2)$ is stepped Heaviside function.

For graphical image of dependences of polaron lifetime on NT radius one can carry out the numerical calculation for private cases.

Let's calculate the polaron lifetime in excited state $\{n = 2, \kappa = 0\}$. In this case the polaron being in $\{n = 2, \kappa = 0\}$ changes its energy state by two ways:

1) firstly it can transition in state $\{n' = \pm 1, \kappa = 0\}$, further in the state $\{n' = 0, \kappa = 0\}$; 2) or directly transitions into state $\{n = 0, \kappa = 0\}$. Though for generated states $\{n = \pm 1, \kappa = 0\}$ the energy values are

similar ones, but possibilities of transitions for them are different ones.

Taking into consideration the above mentioned from (7) we obtain the following expression for polaron lifetime in excited state $\{n = 2, \kappa = 0\}$:

$$\frac{1}{\tau_{2,0} \alpha \omega_L} = \sum_{n'=-1}^1 \frac{\theta((4-n'^2)a^{-2}-1) I_{|2-n'|} \left(\sqrt{4-n'^2-a^2} \right) K_{|2-n'|} \left(\sqrt{4-n'^2-a^2} \right)}{\sqrt{(4-n'^2)a^{-2}-1}} \quad (8)$$

The results of carried investigations on the base of expression (8) are presented fig.1.

The resonance curves of corresponding transitions from $\{n = 2, \kappa = 0\}$ in the state $n' = \pm 1$ и $n' = 0$ are given on this figure from the left to the right.

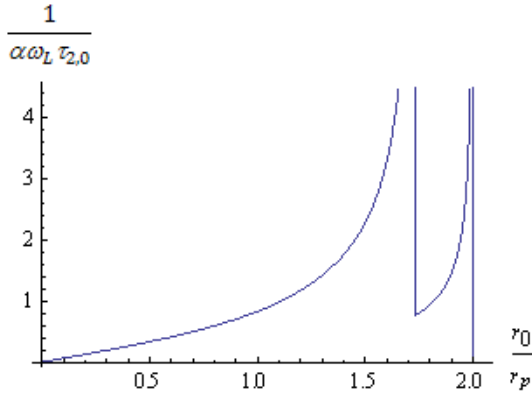


Fig. 1. The dependences of polaron lifetime on r_0/r_p ratio for excited state $\{n = 2, \kappa = 0\}$. The resonance curves are given on the figure from the left to the right of corresponding transitions in the state $n' = \pm 1, n' = 0$.

The presence of the resonances on the figure corresponds to the condition of equality of LO-phonon

energy to intersubband distances, i.e. we obtain the following condition:

$$\hbar \omega_L = \frac{\hbar^2 k^2}{2m} + \frac{\hbar^2 (n^2 - n'^2)}{2m r_0^2} \quad \text{or} \quad a = \sqrt{\frac{n'^2 - n^2}{\kappa^2 - 1}}. \quad (9)$$

As it is seen from the fig.1 two resonances which correspond to transitions $\{n = 2, \kappa = 0\} \rightarrow \{n' = \pm 1, \kappa = 0\}$, $\{n = 2, \kappa = 0\} \rightarrow \{n' = 0, \kappa = 0\}$ are observed with increase of parameter value r_0/r_p . The resonance position of corresponding transitions $\{n = 2, \kappa = 0\} \rightarrow \{n' = 1, \kappa = 0\}$ and $\{n = 2, \kappa = 0\} \rightarrow \{n' = -1, \kappa = 0\}$ on r_0/r_p coincide that is expected in the case of taking into consideration the transitions into generated subbands.

Now we calculate the polaron lifetime in $\{n = 0, \kappa = 1.1\}$ state for intrasubband transition $\{n = 0, \kappa = 1.1\} \rightarrow \{n = 0, \kappa = 0\}$ providing for the possible intermediate intersubband transitions to $n' = \pm 1, \pm 2, \pm 3, \pm 4, \pm 5$ states. In this case the expression for polaron lifetime has the following form:

$$\frac{1}{\tau_{n,\kappa} \alpha \omega_L} = \sum_{n'=-5}^5 \frac{\theta(\kappa^2 - a_{n'})}{\sqrt{\kappa^2 - a_{n'}}} \left[I_{|n'|} \left(\left| \kappa + \sqrt{\kappa^2 - a_{n'}} \right| a \right) K_{|n'|} \left(\left| \kappa + \sqrt{\kappa^2 - a_{n'}} \right| a \right) + \right. \\ \left. + I_{|n'|} \left(\left| \kappa - \sqrt{\kappa^2 - a_{n'}} \right| a \right) K_{|n'|} \left(\left| \kappa - \sqrt{\kappa^2 - a_{n'}} \right| a \right) \right], \quad (10)$$

where $a_{n'} = 1 + n'^2 a^{-2}$.

The results of such calculations carried out on the base of (10) are presented on the fig.2.

The resonance curves corresponding to transitions in state $n' = \pm 1, \pm 2, \pm 3, \pm 4, \pm 5$ are given on the figure from the left to right.

As it is seen from the fig.2 if for transition $\{n = 0, \kappa = 1.1\} \rightarrow \{n = 0, \kappa = 0\}$ we take into consideration the possible intersubband transitions in state

$n' = \pm 1, \pm 2, \pm 3, \pm 4, \pm 5$, then with $a = r_0/r_p$ parameter increase up to 20 one can observe all 5 radiuses. Such situation is connected with the fact that the distance between subbands decreases with NT radius increase and at the given value $a = r_0/r_p$ such transitions are possible.

As a example we give the plots of dependences $\tau_{0,1.1}^{-1}$ on κ for $\{n = 0, \kappa = 1.1\} \rightarrow \{n = 0, \kappa = 0\}$ transition.

The resonance position for $\{n=0\} \rightarrow \{n'=0\}$ transition related to κ are defined from ratio $\kappa = \sqrt{1 - ((n^2 - n'^2)/a^2)}$ which occurs from the condition (9).

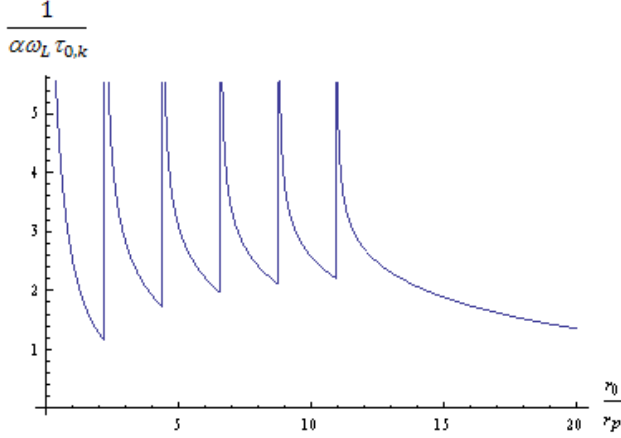


Fig. 2. The dependence of polaron lifetime in excited state $\{n=0, \kappa=1.1\}$ for transition $\{n=0, \kappa=1.1\} \rightarrow \{n=0, \kappa=0\}$ from r_0/r_p ratio with taking into consideration the intermediate transitions.

Below the plot of dependence of $\tau_{0,1.1}^{-1}$ on κ at value $a=5$ is given below.

As it is seen from the fig.3 at value $a=5$ when κ changes from 1 to 2, we have two resonance curves. Such situation means that at $a=5$ the existing distance between subbands gives the possibility in order to include all intermediate subbands into resonance.

From above mentioned figures of dependences $1/\alpha\omega_L\tau_{n,\kappa}$ on a and κ follows that at investigation of polaron relaxation time is necessary to take into

consideration the intersubband transitions. $\tau \approx 1.27 \text{ ps}$. gives the evaluation of lifetime τ at parameter values for GaAs: $\alpha = 0.068$, $\hbar\omega_L = 421 \text{ K}$.

The obtained value is character for LO-phonon lifetime. For example, the measurement results of decay time of nonequilibrium LO-phonons in GaAs is 7ps at temperature 77K [11].

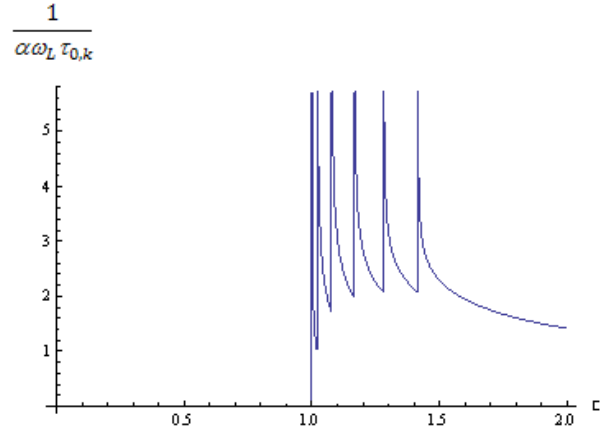


Fig. 3. The plot of dependence of polaron excited state life time on κ at $a=5$ for transition $\{n=0, \kappa\} \rightarrow \{n=0, \kappa=0\}$ with taking into consideration of intermediate transitions in states $n' = \pm 1, \pm 2, \pm 3, \pm 4, \pm 5$.

In conclusion the authors are thankful to prof. F.M. Gashimzade for many discussions of the work during its carrying out.

- [1] V.Ya.Prinz, A.V. Chekhovskiy, V.V. Preobrazhenskii, B.R. Semyagin and A.K. Gutakovsky. Nanotechnology, 13, 231-233, 2002.
- [2] V.Ya. Prinz, V.A. Seleznev, A.K. Gutakovsky, A.V. Chekhovskiy, V.V. Preobrazhenskii, M.A. Putyato, T.A. Gavrilova. Physica E, 6, 828-831, 2000.
- [3] V.Ya. Prinz, V.A. Seleznev and A.K. Gutakovsky. In Proc.24-th Inter. Conf. on the Phys. of Semiconductors, Ed.: World Scientific, Singapore. The Physics of Semiconductors (1999).
- [4] L.I. Magaril, A.A. Romanov, A.Ya. Shik. FTP, 1967, t.21, n 3, 404-409.
- [5] P.J. Price. Ann.Phys., 133, 217-239, 1981.
- [6] N.M. Guseinov, K.A. Rustamov and S.M. Seyid-Rzayeva. Modern Physics Letters B, 1991, Vol. 5, n. 2, 139-149.
- [7] O. Verzelen, R. Ferreira, G. Bastard, S. Hameau, E. Deleporte, Y. Guldner, H. Sakaki, T. Inoshita. Physica B 316-317, 1-7 (2002).
- [8] D.C.Tsui. Phys.Rev. B, 1974, Vol.10, n.12, 5088-5090.
- [9] N.M. Guseinov, O.Z. Alekperov, S.S. Guseynova. Modern Physics Letters B, 20, No.27, 1771-1776, 2006.
- [10] I.S. Gradshteyn, I.M. Ryzhik. Tablitsi integralov i summ, ryadov i proizvedeniy. Izd. "Nauka", Moskva, 1971, 1108 s.

Received: 22.06.2011

THE INFLUENCE OF Ge ATOMS ON THIN FILM $\text{TiGaS}_2(\text{Se}_2, \text{Te}_2)$ FORMATION

E.Sh. ALEKPEROV

*Institute of Physics of Azerbaijan National Academy of Sciences**E-mail: aeldar@hotmail.ru*

The conditions of $\text{TiGa}_{1-x}\text{Ge}_x\text{S}_2(\text{Se}_2, \text{Te}_2)$ thin film formation doped by germanium have been investigated by high-energy electron diffraction (HEED) method. The influence of impurity concentration on substructure and formation temperature of different phases of $\text{TiGa}_{1-x}\text{Ge}_x\text{S}_2(\text{Se}_2, \text{Te}_2)$ films with thickness 30 nm has been established by nanotechnology methods. The orientation relations taking place between epitaxial film and substrate have been also established.

Keywords: thin films, phase formation.

PACS: 544.344; 538.97; 539.216.2; 539.23

INTRODUCTION

The new materials with the given properties are the bases to create new devices or improvement of the existing ones which must satisfy modern requirements.

The investigation of structural characteristics of nano-thickness semiconductor films of $A^{\text{III}}B^{\text{III}}C_2^{\text{VI}}$ type during last twenty years is actual one in modern optoelectronics [1-6].

$\text{TiGaS}_2(\text{Se}_2, \text{Te}_2)$ compounds are the typical representatives of recently opened incomplete valence semiconductor compounds of $A^{\text{III}}B^{\text{III}}C_2^{\text{VI}}$ type having the specific structure of crystal lattice. From this point of view the use of the elements of fourth group in the capacity of impurities for the above mentioned compounds presents the interest.

The experiments to study of semiconductors doped by impurities are divided on two groups.

The works, in which the change of band structure mainly caused by distortion of semiconductor crystal lattice is studied, belong to first group. The investigation of the state density tail propagating in forbidden band depth belongs to first group.

Note that the semiconductor doping level, at which practically there is no any interactions between impurity atoms, is called the weakly doped one. The investigated thin films one can obtain with the help of molecular-beam epitaxy, metal-organic vapor-phase epitaxy and hybrid vapor-phase epitaxy and etc [7]. The method of thermal evaporation from tungsten crucibles is used by us for film preparation. In the given work the influence degree of small additions of Ge impurities on crystal structure of $\text{TiGaS}_2(\text{Se}_2, \text{Te}_2)$ thin film is investigated with the help of electron-diffraction analysis, and the orientation relations taking place between epitaxial film and substrate are also established.

EXPERIMENTAL PART

$\text{TiGa}_{1-x}\text{Ge}_x\text{S}_2(\text{Se}_2, \text{Te}_2)$ ($x=0.01\div0.05$ at.%) films with 30 nm thickness are prepared by the evaporation of synthesized

substance in vacuum at the residual pressure $\sim 10^{-4}$ Pa on substrates consisting of NaCl, KJ fresh cleavages and celluloid (the deposition rate ~ 5 nm/sec). The substrate temperature T_s varies in interval 230-570 K. The content of Ge impurity in $\text{TiGaS}_2(\text{Se}_2, \text{Te}_2)$ compounds varies in the limits $x=0.01\div0.05$ at.%. The obtained films are studied by the method of fast electron diffraction under stipulation that the acceleration voltage is equal to 75 kV.

THE RESULTS AND DISCUSSION

$\text{TiGa}_{0.96}\text{Ge}_{0.04}\text{S}_2(\text{Se}_2, \text{Te}_2)$ films deposited on the above mentioned substrates have the amorphous structure with the values $S=4\pi\sin\theta/\lambda=23.63, 36.52, 56.06 \text{ nm}^{-1}; 21.51, 34.24, 45.16 \text{ nm}^{-1}$ and $21.06, 32.88, 49.73 \text{ nm}^{-1}$ correspondingly, i.e. there are three maximums on the curve of electron scattering intensity in the dependence on scattering angle (fig. 1, a,b,c). The given short-range order parameter of gives the definite information about three coordination spheres. Here θ is scattering angle of diffracted beams, λ is electron wave length. The amorphous phase of $\text{TiGa}_{0.96}\text{Ge}_{0.04}\text{S}_2(\text{Se}_2)$ forms up to $T_s=390(423) \text{ K}$ and for $\text{TiGa}_{0.96}\text{Ge}_{0.04}\text{Te}_2$ films forms up to $T_s=240 \text{ K}$.

For oxidation prevention $\text{TiGa}_{1-x}\text{Ge}_x\text{Te}_2$ films are put into carbonic capsule with thickness 3-5 nm. The crystallization of amorphous films leads to formation of polycrystalline $\text{TiGa}_{0.96}\text{Ge}_{0.04}\text{S}_2$ with lattice parameters of monoclinic syngony $a=1.093; c=1.564 \text{ nm}, \beta=100^\circ, Z=16$, SPS C_{2h}^6 , $\text{TiGa}_{0.96}\text{Ge}_{0.04}\text{Se}_2$ film forms with lattice parameters $a=1.120; c=1.606 \text{ nm}, \beta=100^\circ 6', Z=4$, SPS of C_s^4 and C_c monoclinic syngony, and $\text{TiGa}_{0.96}\text{Ge}_{0.04}\text{Te}_2$ film forms with lattice parameters $a=0.897; c=0.713 \text{ nm}, Z=4$, SPS I4/mcm of tetragonal syngony. The lattice parameters are defined by method [8,9]. The values of elementary cell parameters obtained by us are bigger than analogous ones obtained in [10,11], i.e.

$$\begin{aligned} \text{TiGa}_{0.96}\text{Ge}_{0.04}\text{S}_2 & - \frac{a}{a_{\text{с.н}}} = 1.051 \sim 5.1\%; & \frac{c}{c_{\text{с.н}}} = 1.031 \sim 3.1\%, \\ \text{TiGa}_{0.96}\text{Ge}_{0.04}\text{Se}_2 & - \frac{a}{a_{\text{с.н}}} = 1.040 \sim 4.0\%; & \frac{c}{c_{\text{с.н}}} = 1.027 \sim 2.7\%. \end{aligned}$$

$$\text{TlGa}_{0.96}\text{Ge}_{0.04}\text{Te}_2 - \frac{a}{a_{\delta.n}} = 1.064 \sim 6.4 \% ; \quad \frac{c}{c_{\delta.n}} = 1.038 \sim 3.8\%.$$

Here $a_{\delta.n}, c_{\delta.n}$ are elementary cell parameters of triple compounds without impurities.

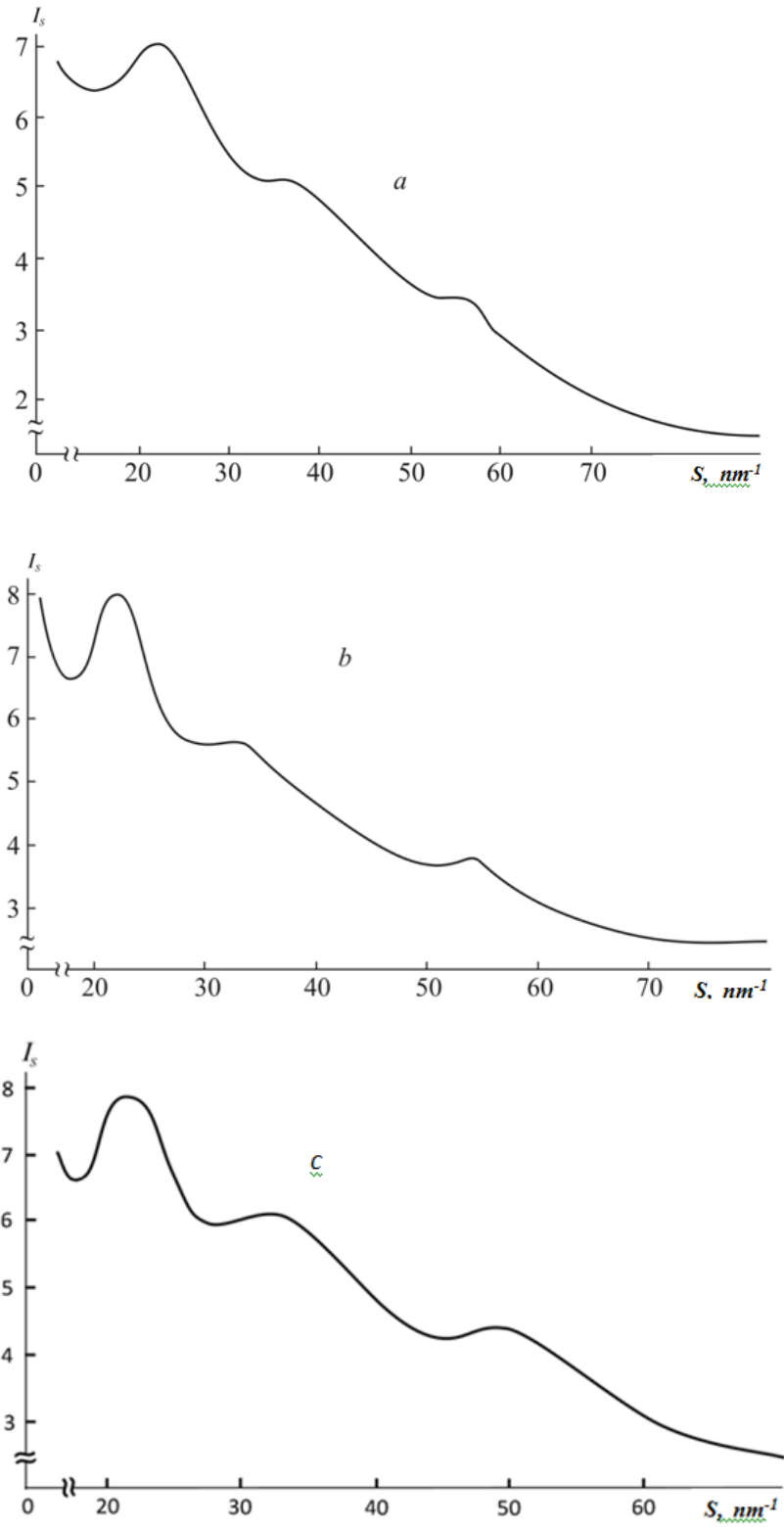
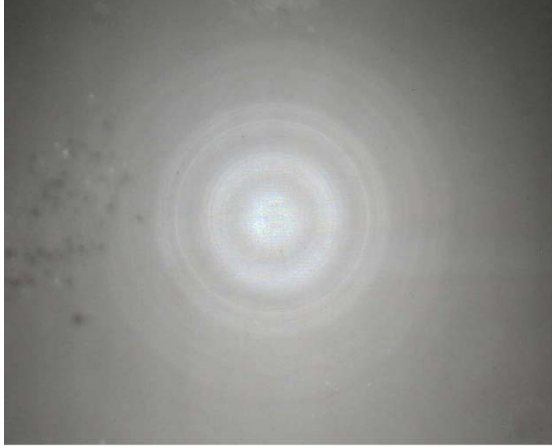
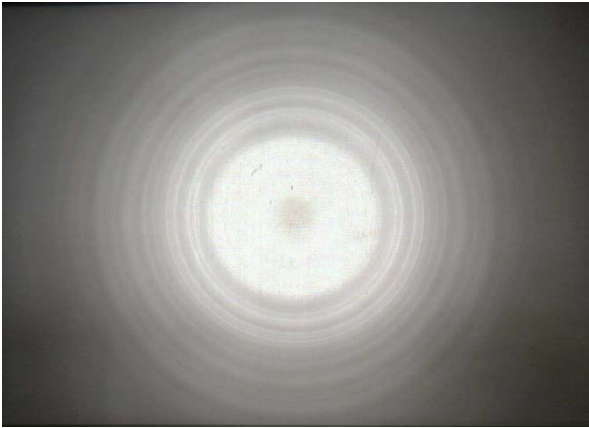


Fig.1. The intensity curve of electron scattering for amorphous films:
a - $\text{TlGa}_{1-x}\text{Ge}_x\text{S}_2$, *b* - $\text{TlGa}_{1-x}\text{Ge}_x\text{Se}_2$, *c* - $\text{TlGa}_{1-x}\text{Ge}_x\text{Te}_2$

These relations show that impurity atoms influence on the formation of crystal structure. This fact is discussed in [12]. The polycrystalline films $\text{TlGa}_{0.96}\text{Ge}_{0.04}\text{S}_2$, $\text{TlGa}_{0.96}\text{Ge}_{0.04}\text{Se}_2$ and $\text{TlGa}_{0.96}\text{Ge}_{0.04}\text{Te}_2$ form on the substrates (NaCl, KCl) at temperature intervals $T_s=400\div 433$ K, $T_s=430\div 453$ K and $T_s=365\div 390$ K correspondingly (fig.2a,b,c).



a



b

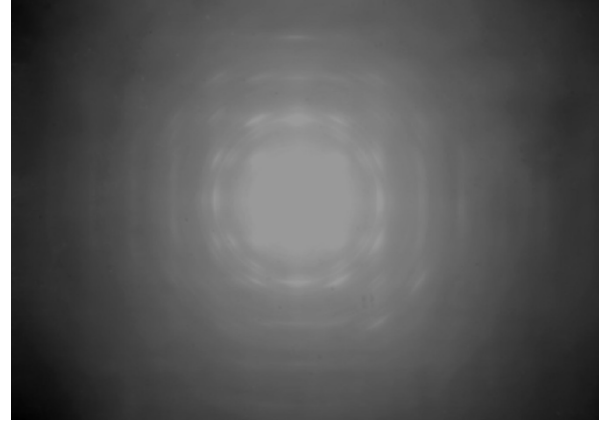


c

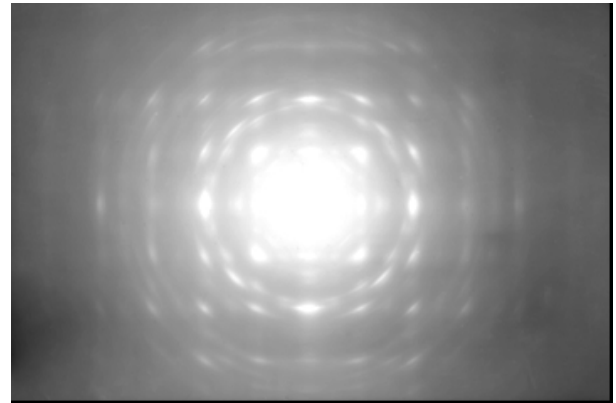
Fig.2. The electron diffraction patterns of polycrystalline phase:
a - $\text{TlGa}_{1-x}\text{Ge}_x\text{S}_2$, *b* - $\text{TlGa}_{1-x}\text{Ge}_x\text{Se}_2$,
c - $\text{TlGa}_{1-x}\text{Ge}_x\text{Te}_2$

The monoclinic syngony undergoes the temperature irreversible phase transformation and transits into tetragonal one with crystal lattice parameters: $a=b=0.764$, $c=3.083$ nm, $Z=16$, space group of symmetry $I4/\mu m$ and $a=b=0.837$, $c=0.659$ nm, $Z=4$, space group of symmetry $I4/mcm$ with

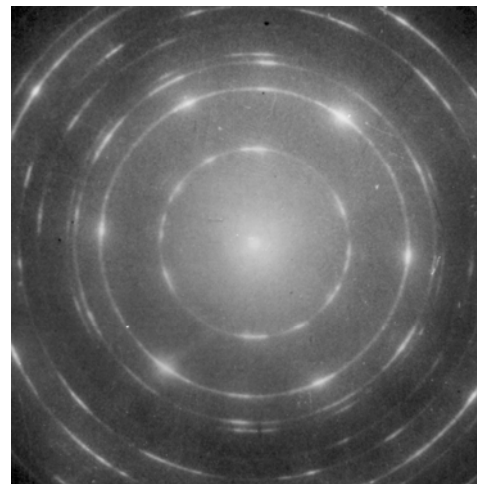
increase of substrate temperature up to $T_s=443$ K for $\text{TlGa}_{0.96}\text{Ge}_{0.04}\text{S}_2$ and up to $T_s=463$ K for $\text{TlGa}_{0.96}\text{Ge}_x\text{Se}$. The co-existence of these two structures caused by phase transition process is accompanied by strong change of atom coordination and bond characteristics between them. At the further increase of substrate temperature (for $\text{TlGa}_{1-x}\text{Ge}_x\text{S}_2$ up to $T_s=453$ K, for $\text{TlGa}_{1-x}\text{Ge}_x\text{Se}_2$ up to $T_s=513$ K and for $\text{TlGa}_{1-x}\text{Ge}_x\text{Te}_2$ up to $T_s=413$ K) the obtained films are already consist of oriented small crystals. However, as diffraction shows, the formed texture is imperfect one. Besides, it is established that $\text{TlGa}_{1-x}\text{Ge}_x\text{S}_2(\text{Se}_2, \text{Te}_2)$ small crystals form the texture with “*c*” axis perpendicular to substrate (fig.3a,b,c).



a



b



c

Fig.3. The electron diffraction patterns from textured films:
a - $\text{TlGa}_{1-x}\text{Ge}_x\text{S}_2$, *b* - $\text{TlGa}_{1-x}\text{Ge}_x\text{Se}_2$, *c* - $\text{TlGa}_{1-x}\text{Ge}_x\text{Te}_2$

The further increase of NaCl, KCl substrate temperature for $\text{TlGa}_{1-x}\text{Ge}_x\text{S}_2$ up to $T_s=480$ K, for $\text{TlGa}_{1-x}\text{Ge}_x\text{Se}_2$ up to $T_s=530$ K and for $\text{TlGa}_{1-x}\text{Ge}_x\text{Te}_2$ up to $T_s=435$ K leads to formation of mosaic monocrystal. At the further temperature growth the increase of point reflex intensity is observed on electron diffraction patterns, that evidences the formation of monocrystalline blocks with different perfect degree. The reflex intensities which are characteristic once for polycrystals decrease and slowly disappear. At the increase of NaCl, KCl substrate temperature up to ~ 503 K, ~ 563 K and ~ 453 K the more perfect monocrystalline films $\text{TlGa}_{1-x}\text{Ge}_x\text{S}_2$, $\text{TlGa}_{1-x}\text{Ge}_x\text{Se}_2$ and $\text{TlGa}_{1-x}\text{Ge}_x\text{Te}_2$ form. The indexing of diffraction pattern of crystal phase taken under direct angle shows well coincidence with parameters of above mentioned tetragonal cell. The electron diffraction pattern taken under angle $\varphi=30\div 60^\circ$ allows us the definition of "c" crystal lattice period which is shown by us above. The obtained epitaxial films $\text{TlGa}_{1-x}\text{Ge}_x\text{S}_2(\text{Se}_2)$ are oriented by (100) plane and $\text{TlGa}_{1-x}\text{Ge}_x\text{Te}_2$ film is oriented by (001) plane parallel to substrate edge [100]. Note, that the inclusion distribution in crystal volume obeys definite crystallographic orders: in many cases the planes (111) are the ones of primary impurity segregation.

CONCLUSION

Thus, the phases with different substructures with increased parameters of crystal lattice elementary cells changing the syngony form at $\text{TlGa}_{1-x}\text{Ge}_x\text{S}_2(\text{Se}_2, \text{Te}_2)$ ($x=0.01\div 0.05$ at.%) film precipitation on the substrates of monocrystalline NaCl, KCl and amorphous celluloid by the thermal evaporation method at different temperatures. The addition of few quantities of impurities leads to increase of temperature interval of amorphous phase formation and for all rest obtained substructures leads to decrease of film formation temperature. It is established that the variation of lattice parameters is the one of obtaining methods of homogeneous high-oriented monocrystalline films with minimal defect level.

Nowadays, in the connection of lack of material data, there is no possibility to formulate the clear interaction between formation conditions of thin epitaxial films and influence degree on this process of few additions of different impurities.

The author is thankful to head of the laboratory D.I. Ismaylov for useful notes.

-
- [1] A.N. Georgobiani, A.X. Matiev, B.M. Xamxoev, A.M. Evloev. Neorgan. materiali. 2005. T. 41. № 1.S. 148-152. (In Russian).
 - [2] A.E. Baxishev, A.A. Lebedev, Z.D. Xalafov, M.A. Yakobsan. FTP. 1978. T. 12. № 3. S. 580-583.(In Russian).
 - [3] J.S. Johannessen, W.E. Spicer, J.F. Gibbons, J.D. Plummer. J.Appl. Phys. 1978. V. 48. P. 4453-4458.
 - [4] R. Durny, A.E. Hill, R.D. Tomlinson. Thin Solid Films. 1980. V. 69. № 1. P. L11.
 - [5] D.M. Ismailov, M.F. Alieva, E.Sh. Alekperov, F.I. Aliev. FTP. 2003. T. 37. № 7. S. 772-776. (In Russian).
 - [6] Ax.U.Malsagov i dr.Obzor literaturi po poluprovodnikovim soedineniyam tipa $\text{A}'\text{B}'''\text{C}_2^{\text{IV}}$, $\text{TlB}'''\text{C}_2^{\text{IV}}$. Nalchik EL-FA, 2007. 694 s. (In Russian).
 - [7] Molekulyarno – lucheovaya epitaksiya I geterostrukturi. Pod red. L.Cenga, K. Ploga Per. S angl. Pod red. Alferova J.I.M.: Mir, 1989. 582 s. (In Russian)
 - [8] B.K. Vayneshteyn. Strukturnaya elektronografiya.M.:AN SSSR, 1956. 313 s.(In Russian).
 - [9] A.S. Avilov, R.M. Imamov, S.A. Semiletov. RTE. 1976. № 3. S. 214-215. (In Russian).
 - [10] D.I. Ismailov, E.Sh. Alekperov, M.F. Alieva. Surface Investigation, 2000. V. 15. P. 1897.
 - [11] D.Müller, H. Hahn. Zur struktur des TlGaSe_2 Zeitsch. Anorg. Allgem. Chem. 1978. V. 438. № 1. P. 258-262.
 - [12] E.Sh. Alekperov, A.K. Sharifova, D.I. Ismailov. Kristallografiya. 2009. T. 54. № 3. S.550-553.(In Russian).

Received: 01.07.2011

OPTICAL PROPERTIES OF MnGa_2Se_4 IN THE REGION OF SELF-ABSORPTION EDGE

B.G. TAGIYEV¹, T.G. KERIMOVA¹, O.B. TAGIYEV^{1,2},
I.A. MAMEDOVA¹, S.G. ASADULLAYEVA¹

¹*H.M. Abdullayev Institute of Physics of Azerbaijan National Academy of Sciences
AZ 1143, G.Javid ave., 33, Baku*

²*The branch of the Institute of M.V. Lomonosov MSU*

Optical absorption spectra of MnGa_2Se_4 (S_4^2 ph. gr.) single crystals have been investigated in 110-295K temperature range. By the using of group-theoretical analyses for compounds crystallized in S_4^2 space group and by comprising with izoelectron analogies it was shown that the minimal optical transitions localize in the centre of Brillouin zone $\Gamma(000)$. Features in low energy region at 2,31 and 2,43 eV are connected with intracenter transitions from splitting by crystal field states 6A_1 , (${}^6A_1^{(1)}$, ${}^6A_1^{(2)}$) to $\Gamma_2(G)$ state. It was shown the contribution to the crystal splitting what is due to difference of pseudopotentials of cation sublattice atoms privileges the contribution due to tetragonal distortion.

Keywords: intracenter transitions, self-absorption edge

PACS: 535.343.2

MnGa_2Se_4 belongs to the group of compounds of $A^2B^3_2C^6_4$ (A-Mn, B-Ga, In, C-S, Se, Te) type and is the semimagnetic semiconductor compound. This compound firstly had been synthesized by authors [1]. As a result of rentgenographic investigations it is shown that MnGa_2Se_4 is crystallized in tetragonal structure (space group S_4^2) with lattice parameters $a=5,674\text{\AA}$, $c=10,757\text{\AA}$, $c/a=1,895$. Further, this compound had been obtained by authors [2,3]. The semimagnetic semiconductor compounds take the significant interest in the use in semiconductor instrument engineering, in particular, in spintronics and etc. That's why the comprehensive investigation of physical properties of such compounds is the one of actual problems of solid state physics.

In spite of the fact that magnetic properties of this compound have been investigated in detail, however, the optical properties haven't been investigated properly. The optical properties of MnGa_2Se_4 are investigated in [4,5]. However, the conclusions about the character of optical transfers in this compound are different ones. By the opinions of the authors [4] the self-absorption edge of MnGa_2Se_4 forms by the indirect optical transfers. The observable peculiarity at 2,43eV is connected with intracenter transitions in Mn atoms. Later in [5] the investigations of self-absorption edge in MnGa_2Se_4 in magnetic fields up to 20 GPa also have been carried out. At 146GPa the phase transition in NaCl structure is observed. The authors confirm that self-absorption edge in MnGa_2Se_4 forms by the direct optical transitions. For the forbidden band width the value 2,7 eV is given. Note that in these works the authors don't show in which point of Brillouin band has the least energy gap and which irreducible representations the valence band and conduction one are described.

In present work the results of temperature dependences of absorption coefficient of MnGa_2Se_4 in 110-293K interval are given (fig.1). The single crystals MnGa_2Se_4 are obtained by the gas-transport reaction method. The crystalline iodine is used in the capacity of carrier. The lattice parameters defined by roentgenographic method $a=5.671\text{\AA}$, $c=10.754\text{\AA}$, $c/a=1,9$ agree with results [1]. The measurements are carried out on the samples with thickness 70-100 μm . On the fig.1 it is seen that at 295K the dependence of absorption coefficient on incident radiation energy gradually increase with bendings at

2,31 eV and 2,42eV. The maximums are observed with temperature decrease up to 110K on the bending places. At temperature decrease up to 110K the maximum at 2,45 eV is observed on bending place at 2,42eV. In high-energy region the absorption coefficient increases up to $7\cdot 10^2\text{cm}^{-1}$.

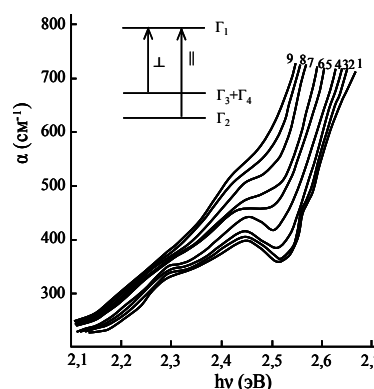


Fig.1. The dependence of absorption coefficient on the incident radiation energy in MnGa_2Se_4 at different values temperatures T, K: 1- 110 K, 2- 135 K, 3- 159, 4- 184, 5- 217, 6- 240, 7- 259, 8- 277, 9- 295. The scheme of optical transfers in $\Gamma(000)$ of Brillouin zone MnGa_2Se_4 is given in insertion.

Nowadays the calculations of band structure MnGa_2Se_4 are absent. However, one can make the specified conclusions about band structure in the region of self-absorption edge of this compound using the results of theoretical-group investigations carried out for the compounds crystallizing in space group S_4^2 [6]. MnGa_2Se_4 is also as the compounds of $A^2B^3_2C^6_4$ (CdGa_2S_4 , CdGa_2Se_4 , ZnGa_2Se_4) type crystallizes in space group S_4^2 . The compounds crystallizing in space group S_4^2 have two types of atoms in cation sublattice, ordered cation vacancy and lattice tetragonal compression along C axis.

In [6] the symmetry of electron states in compounds crystallizing in space group S_4^2 is investigated by group-theoretical method. The state ratio forming the valence band top and conduction band bottom is established, the selection rules for optical transitions in high-symmetrical points of Brillouin zone are obtained. The optical transitions in $A^2B^3_2C^6_4$ (CdGa_2S_4 , CdGa_2Se_4 , ZnGa_2Se_4) compounds realize in the center of Brillouin zone by the means of the

analysis of experimental results towards with results of group- theoretical investigations and the comparison them with isoelectron analogues of A^3B^5 , $A^3B^4C^5$ (GaAs, GaP, ZnGeP₂, ZnGaAs₂) compounds. As $MnGa_2Se_4$ is the isoelectron analogue of $ZnGa_2Se_4$ and crystallizes in space group S_4^2 one can confirm that in this compound also as in $ZnGa_2Se_4$ the self-absorption edge localizes in the center of Brillouin band, the top of valence band and the bottom of conduction band in dipole approximation form by the states $(\Gamma_3+\Gamma_4)^v$, $(\Gamma_2)^v$ and Γ_1^c . The top of the valence band is splitted by crystalline field. As it is above mentioned in $MnGa_2Se_4$ the presence of two types of atoms in cation sublattice and lattice compressing $c/a=1,9$ along tetragonal axis which occur the excitation, takes place. The last one leads to the splitting of valence band top. That's why two factors make the contribution in crystalline splitting: pseudopotential difference of cation sublattice atoms and tetragonal compressing.

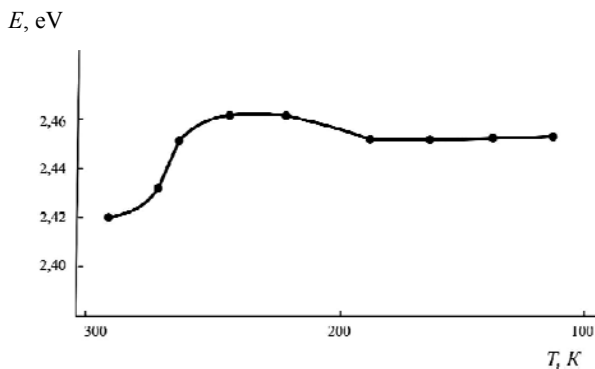


Fig.2. The dependence of maximum position on temperature at 2,42eV.

Following from above mentioned one can suggest the scheme of optical transitions in $MnGa_2Se_4$ in the center of Brillouin zone (fig.1 insertion). The optical transitions $\Gamma_3+\Gamma_4 \rightarrow \Gamma_1$ realize in polarization $E \perp c$ and $\Gamma_2 \rightarrow \Gamma_1$ into $E \parallel c$. The temperature coefficient of displacement of self-absorption edge in high-energy region $\frac{dE}{dT} = 6 \cdot 10^{-4}$ eV. The self-absorption edge of $MnGa_2Se_4$ at 295K is equal to ~2,5eV. In interval 295-110K the self-absorption edge changes by linear law that evidences about the fact that in this temperature region the main contribution in temperature coefficient of displacement of forbidden band width gives the electron-phonon interaction. The peculiarities at 2,31eV and 2,42 eV reveal the weak temperature dependence. The dependence of maximum position at 2,42eV on temperature is shown on fig.2. It is seen that with temperature decrease in

interval 295-220K the maximum position at 2,42eV weakly increases with temperature and further doesn't depend on temperature.

The presence of two closely situated peculiarities evidences about splitting of the line by crystalline field. The difference in energy position of peculiarities at 2,31eV and 2,45eV at 110K is equal to 0,14eV that one can consider as crystalline splitting Δ_{cr} . That's why according to [4] it is followed to suppose that these lines are connected with intracenter transitions in Mn^{2+} (${}^6A_1 \rightarrow {}^4T_2({}^4G)$) and (${}^6A_1 \rightarrow {}^4T_2(G)$) (fig.3). The $Mn {}^6A_1$ level is splitted by crystalline field.

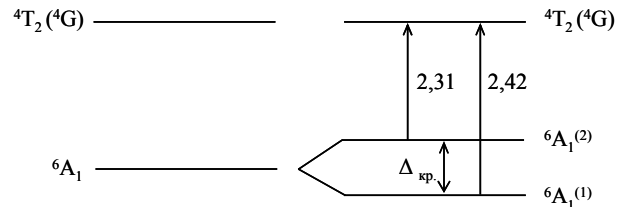


Fig.3. The scheme of intracenter transitions in Mn atoms.

The crystalline splitting connected with lattice compressing along tetragonal axis one can evaluate by the formulae [7] $\Delta_{cr} = -\frac{3}{2}b(2-\frac{c}{a})$ if we consider the triple compound $MnGa_2Se_4$ as isoelectron analogue of A^3B^5 compound compressed up to the value of tetragonal compressing of triple compounds. In this formulae a and c are lattice parameters, b is the value of deformation potential of the top of valence band of isoelectron analogue of A^3B^5 . GaAs for which the value $b = 1,7$ eV [8] is isoelectron analogue of $MnGa_2Se_4$ [8]. The calculated value $\Delta_{cr}=0,25$ eV. This value is bigger than observable splitted peculiarities at 2,31eV and 2,45 eV (at 110K) ($\Delta_{cr}=0,14$). Such difference can be explained by the following way. It is above mentioned that in triple semiconductors in crystalline splitting the two factors make the contribution. There are lattice compressing along tetragonal C axis and difference of pseudopotentials in cation sublattices. In $MnGa_2Se_4$ cation sublattice there is also ordered cation vacancy Mn besides two types of atoms. The last one forms the significant difference of pseudopotentials. It is known that [9] the lattice compressing along tetragonal axis and the difference of pseudopotentials of cation sublattices form the similar values by the order and opposite values by splitting sign. Consequently, the difference of experimentally definite value Δ_{cr} on calculated by the formula one is connected with the influence of difference of pseudopotentials of cation lattice atoms on tetragonal compressing.

- [1] K.I. Range, H. Hubner J. Naturforschung, 316 (1976) 886.
- [2] R. Rimet, S.Schleneer, D. Fuchart, J. Physique 43 (1982) 1759.
- [3] R. Tovar, M. Quintero, E. Quintero et al. Materials Research Bulletin, 37 (2002) 1011-1022.
- [4] G.H. Niftiyev, E.Z. Zeynalov. FTP, 1991, t.25, v.4. s. 704-705.
- [5] I. Consales, R.J. Licos Caldera, M. Quintero, M. Maracoima, Phys. Stat. Sol. 1999, v. 211, N1,

- pp. 45-49.
- [6] D.A. Guseinova, T.G. Kerimova, R.Kh. Nani. FTP, 1977, t.11, v.2, s.1135-1142.
- [7] F.M. Polak, M. Cardona, Phys. Rev., 1968, v.172, p.816-837.
- [8] I.D. Willey, Solid State Communications 1970, v.8, N12, p.1865-1868.
- [9] A.S. Poplovnoy, G.F. Kapavayev. Izv. AN SSSR, Neorganicheskie materialy, 1968, t.4, №2, s.196-199.

Received: 01.06.2011

THE ROLE OF EIGEN COMPONENTS AT ENERGY SPECTRUM IN Ag_2Te

F.F. ALIYEV, A.A. SADDINOVA, R.A. GASANOVA, N.A. VERDIYEVA

H.M. Abdullayev Institute of Physics Azerbaijan National Academy of Sciences,

H. Javid ave., 33, Baku, Az-1143, Azerbaijan

farzali@physics.ab.az.

The temperature dependences of electric conduction σ , Hall coefficient R and thermo-e.m.f. α_0 in p- and n- Ag_2Te in temperature interval 4,2-300K have been investigated. The obtained experimental data are interpreted in the framework of two-band model of charge carrier dispersion law. It is established that peculiarities of kinetic parameters in p- and n- Ag_2Te are connected with complex band structures of charge carrier energy spectrum.

Key words: mobility, interelectron interactions, point defects, sublattice, effective mass.

PACS: 72.15.Jf; 72.25.Pa

The deficiency of $\text{Ag}_{2-x}\text{B}^{\text{VI}}$ (B-Te, Se, S) compounds which significantly influences on kinetic coefficients is their peculiarity. The defect concentration increases with temperature growth that leads at structural phase transitions (PhT) at definite temperature. The heat and electrophysical properties of samples of Ag_2Te , which is the one of $\text{Ag}_{2-x}\text{B}^{\text{VI}}$ compounds, change unevenly at PhT.

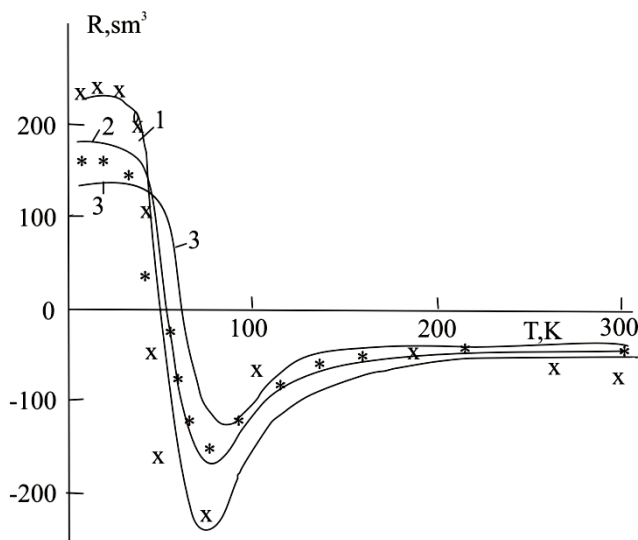


Fig. 1. Temperature dependences of Hall coefficient $R(T)$ in p- Ag_2Te : experimental points with Te excess; x-0.75 at. %, *-1.0 at.%. The total curves are calculated at different values of forbidden band width: E_g : 1-0.025 eV, 3-0.07 eV.

As it is shown in [1] the excess of Te in Ag_2Te homogeneity region leads to p-type conduction and the excess of Ag leads to n-type one. Ag atom excess in Ag_2Te forms the small donor levels [2], and Te-acceptor atom excess [3] situated from on the bottom of conduction band on the distance $(0.002-7 \cdot 10^{-5})$ eV. The information about Ag_2Te forbidden band width (E_g) is different: 0.006 eV [3]; 0.035 eV [4]; 0.058 eV [5]; 0.113 eV [6]; 0.19 eV [7]; 0.7 eV [8] in dependence of defect level.

The present paper is dedicated to establishment of reasons of forbidden band width different obtained values in Ag_2Te .

The investigations are carried out on the sample series Ag_2Te with Te atom excess up to ~1 at.% and Ag atom

excess up to ~0.25 at.%, obtained on unique technology [9] in temperature interval 4,2-300K. Analysis shows that excess of Te up to ~1 at.% and Ag up to ~0.25 at.%, don't cause the second phase appearance and any changes in crystal structure. At this it is revealed that hole concentration is proportional to Te content [1,4,11] and beginning from the lack of $\text{Ag} \geq 0.01$ at.% in stoichiometric content of Ag_2Te n-type conduction takes place [2]. Experimental data on temperature dependences of Hall coefficient $R(T)$, electric conduction $\sigma(T)$ and thermo-e.m.f. $\alpha_0(T)$ are presented on figures 1-3. The temperature behavior of R , σ and α_0 for hole concentration $p = 6.25 \cdot 10^{16} \text{ cm}^{-3}$ and electron one $n = 1 \cdot 10^{18} \text{ cm}^{-3}$ is presented in [2,4]. As it is seen, Hall coefficient doesn't depend on T up to inversion point, further it decreases with temperature growth and at $T = 55\text{K}$, 65K , 78K changes the sign on negative one, achieves maximum at $T = 75\text{K}$, 80K , 85K , then $|R|(T)$ slowly decreases and the decrease of $|R|$ slows down in temperature interval ~200-300K. This fact that inversion points R and α_0 shifts to high temperatures pays attention.

As it is seen from $R(T)$ at temperature increase starting from the inversion point the hole gas degeneracy disappears and the intrinsic conductivity begins (Fig. 1).

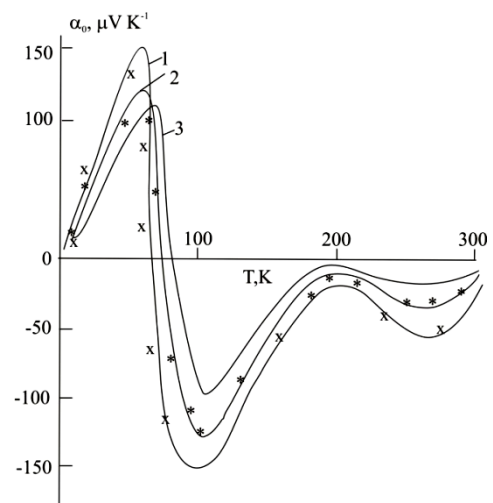


Fig. 2. Temperature dependences of thermo-e.m.f. $\alpha_0(T)$ in p- Ag_2Te . The designations are the same that on the fig. 1

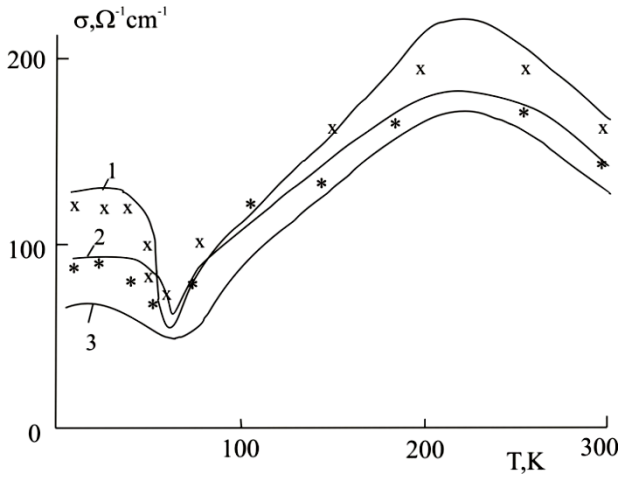


Fig. 3. Temperature dependences of electric conduction $\sigma(T)$ in p-Ag₂Te. The designations are the same that on the fig.1.

In the region of intrinsic conduction $R(T)$, $\sigma(T)$ and $\alpha_0(T)$ values in slow magnetic for two types of charge carriers field are obtained by following formulae [12]:

$$R = \frac{1}{N_a e} \frac{(1-c)(1-b^2 c)}{(1+bc)^2} \quad (1)$$

$$\sigma = \frac{1}{N_a e} \frac{1+bc}{b(1-c)} \quad (2)$$

$$\alpha_0 = \frac{\sigma_p \alpha_{0p} - \sigma_n \alpha_{0n}}{\sigma_p + \sigma_n} \quad (3)$$

where $N_a = p(1-c)$ is acceptor concentration, U_n/U_p –hole and electron mobility ratio, $c = n/p$ is ratio of electron concentration to hole concentration, $\sigma_p, \sigma_n, \alpha_{0p}, \alpha_{0n}$ are electric conduction and thermo-e.m.f. of holes and electrons correspondingly

Temperature dependences of $U_n(T)$ and $U_p(T)$ mobilities for dispersion on impurity ions and acoustic phonons are calculated by methods [2,4]. At sign inversion the of Hall coefficient R the mobility ratio is equal to $b = 1/c^2$ and at minimum $|R(T)| = |R_{min}|$, the ratio is as follows: $b = 1/c$ [12].

$$|R_{min}| = \frac{(1-b)^2}{4beN_a}$$

The value «b» is chosen so that calculated R values coincide with experimental data ($R > R_{min}$). Temperature dependence $c(T)$ is calculated by the formula:

$$c = \frac{n_i}{N_a + p_i}$$

where

$$n_i = p_i = 4,9 \cdot 10^{15} \left(\frac{m_n m_p}{m_0} \right)^{3/4} T^{3/2} \exp(-\varepsilon_g / 2k_0 T),$$

$$m_n (m_n = 0,022 m_0) \text{ and } m_p (m_p = 0,12 m_0 [4]), \quad \varepsilon_g = \varepsilon_{g0} - \partial \varepsilon_g / \partial T, \quad \partial \varepsilon_g / \partial T = 7 \cdot 10^{-5} \text{ TeV} \cdot \text{K}^{-1} [2,4].$$

Taking under consideration «b» and «c» in (1) $R(T)$ (fig.1) and $c(T)$ at different ε_{g0} values are calculated. As it is seen, the shift of inversion point of $R(T)$ corresponds to different ε_g values as it increases with growth of hole or Te atom concentrations (the contribution of acceptor concentration blurring isn't taken under consideration, i.e. at $R(T)$ inversion the conditions $p \gg n$ and $U_n > U_p$ should be satisfied). At this $pU_p^2 < nU_n^2$ and $R < 0$ (n sign dominates).

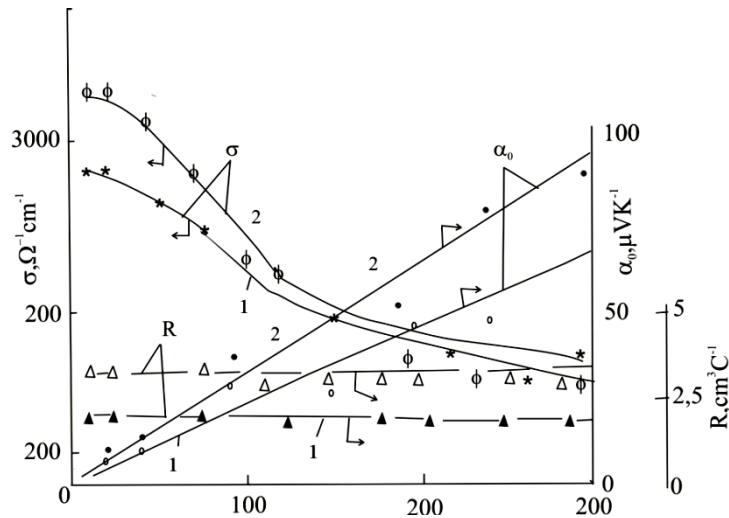


Fig. 4. Temperature dependences of Hall coefficient $R(T)$ (Δ, \blacktriangle), thermo-e.m.f. $\alpha_0(T)$ (\circ, \bullet) and electric conduction $\sigma(T)$ ($\phi, *$) in n-Ag₂Te with excess of Ag: $\Delta, \circ, \phi, 0,01$ at.%, $\blacktriangle, \bullet, *, 0,05$ a.t.%. The total calculated lines at different forbidden band width E_g ; 1-0,025eV, 2-0.05 eV.

Such behavior of $R(T)$ in n-Ag₂Te isn't observed (fig.4). Here the electrons play the main role in conduction and the gas degeneracy removal with temperature growth up to phase transition isn't observed. Moreover, Hall coefficient $R=1/en$ weakly changes with temperature. The authors [1-4] show that electron dispersion law in n-Ag₂Te is obeyed to Kein model and electron concentration is defined according to [11]:

$$n = \frac{(2m_n k_0 T)^{3/2}}{3\pi^2 \hbar^3} I_{3/2}^0(\mu_n^*, \beta) \quad , \quad (4)$$

where $I_{3/2}^0(\mu_n^*, \beta)$ is Fermi two-parametric integral, $\mu_n^* = \mu_n / k_0 T$, μ_n is chemical potential, $\beta = k_0 T / \varepsilon_g$ is parameter characterizing the band irregularity. From formula (2) it is seen that n depends on two parameters ε_g and μ_n . That's why one can't clearly say about correlation between $R(T)$ and ε_g . The relatively high value (0.058, 0.19 eV) is obtained for ε_g at investigation of n-Ag₂Te optical properties [5,7]. It is seen that authors don't take under consideration Burshtein shift at definition of ε_g value. As it is established in [2], Ag atoms in Ag₂Te create the donor levels situated from conduction band bottom on distance $(0,002-7 \cdot 10^{-5} T \cdot K^{-1})$ eV.

Thus, taking under consideration the calculated data about ε_g obtained by us can be analyzed by following way: in Ag₂Te the edges of conduction and valency bands have different structures [13]. The one electron is on the Ag valence shells and the electrons of d-shell of Ag play the significant role in formation of chemical bond. That's why d-electrons of Ag take part in formation of valency bands in Ag₂Te with S-bands of Te. As a result of this one can suppose the presence of two valent subbands in Ag₂Te: one band connected with d-electrons of Ag and second one caused by S states of Te.

Obviously, P and S bands of Ag in Ag₂Te situate closer to each other that leads to less value of forbidden band width in Ag₂Te. Here one can note that Coulomb interaction between Ag and Te atoms depends on the number of surrounding atoms, as a result of which the forbidden width band ε_g forms in Ag₂Te as Te atoms play the big rol in ε_g formation because of big ion radius of tellurium [14]. Insignificant forbidden band width leads to the fact that Hall coefficient and thermo-e.m.f. are totally defined by electron even at intrinsic conduction. The material is considered as hole one and Hall coefficient is negative one when hole concentration is bigger in several times than electron concentration. This and some other consequences are results of big value of matrix element of interaction ($P_I=5,4 \cdot 10^8$ eV·cm) [15].

-
- | | |
|---|--|
| <p>[1] S.A. Aliev, F.F. Aliev. Izv.AN SSSR, Neorg. mater., 25(2), 241 (1989). (In Russian).</p> <p>[2] F.F. Aliev, M.B. Jafarov. FTP, 42 (11), 1297 (2008). (In Russian).</p> <p>[3] A.S. Koroleva, V.U. Martinov, P.P. Petrov, Tez. 2-y Vses. Konf. CQU "Materialovedenie xalkogenidnix kislorodsoderjaushix poluprovodnikov". t.11, 47 (1986). (In Russian).</p> <p>[4] F.F. Aliev, E.M. Kerimova, S.A. Aliev, FTP, 36 (8), 932 (2002). (In Russian).</p> <p>[5] R. Dalven, R. Gill. Energy Gap in β- Ag₂Te. Phys. Rev., 143 (2), 666 (1966).</p> <p>[6] A. Addel, S. Gromb. Proprietes electroniques et electrogalvaniques du tellurure d'ϕкпыте β domaine d'existence . J. Phys. Chem. Sol., 44 (2), 95 (1983).</p> | <p>[7] T.G. Kerimova, S.A. Aliev, G.A. Axundov, FTP, 4 (2), 400 (1970). (In Russian).</p> <p>[8] I.A. Drabkin, B.Y. Moyjes. FTP, 21 (9), 1715 (1987). (In Russian).</p> <p>[9] V.M. Glazov, N.M. Maxmudova. Izv.AN SSSR, Neorg. mater., 6(8), 1409 (1970). (In Russian).</p> <p>[10] S.A. Aliev, F.F. Aliev, G.P. Pashayev. Neorg.mater., 29, (8), 1073 (1993). (In Russian).</p> <p>[11] F.F. Aliev, M.B. Jafarov, G.Z. Askerova, E.M. Gojaev. FTP, 44(8), 1042 (2010). (In Russian).</p> <p>[12] K. Xilsum, A. Rouz-Ins. Poluprovodniki tipa $A^{III}B^V$ (M., IL, 1963). (In Russian).</p> <p>[13] C.M.Fang, R.A.de Groot, G.A.Wigers. J. of Phys. and Chem. of Sol. 63, 457 (2002).</p> <p>[14] S.A. Aliev, F.F. Aliev. Izv.AN SSSR, Neorg. mater., 21 (II), 1869 (1985). (In Russian).</p> |
|---|--|

Received: 20.06.2011

THEORETICAL AB INITIO STUDY THE HYDROGEN BONDING NATURE OF THE A:T BASE PAIR

MOHANNED JASEM AL-ANBER

Department of Physics, College of Science, Basrah University, Basrah, Iraq

E-mail: mohanadalanbar@yahoo.com

The effect of applied external electric field on DNA occurs mostly at high field intensity. The results of the theoretical ab initio study on the applied electric field on A:T base pair components are reported. The geometries of the local minima were optimized at DFT level (B3LYP). The 6-31G(d,p) basis set was used. The geometrical parameters, relative stability, interaction energies and nature of hydrogen bonding energy are reported. Also, focus on the range of hydrogen bonding energy and the flexibility of the rotation angle between the A:T base pair. So that the electric field mutation may be able to be classified as multi-point mutation.

Keywords: DFT, DNA, ab initio calculation, electric field effect, mutating.

Pacs:

1. INTRODUCTION

After accurately describing the structure of DNA, Watson and Crick suggested that the effects of spontaneous mutations on DNA [1]. DNA can be damaged by many different sorts of mutagens. These include oxidizing agents, alkylating agents and also high-energy electromagnetic radiation such as ultraviolet light and X-rays. The type of DNA damage produced depends on the type of mutagen. For example, UV light mostly damages DNA by producing thymine dimers, which are cross-links between adjacent pyrimidine bases in a DNA strand [2]. On the other hand, oxidants such as free radicals or hydrogen peroxide produce multiple forms of damage, including base modifications, particularly of guanosine, as well as double-strand breaks [3]. It has been estimated that in each human cell, about 500 bases suffer oxidation damage per day [4,5]. The most serious damage of these oxidative lesions are the double-strand breaks, as these lesions are difficult to repair and can produce point mutations, insertions and deletions from the DNA sequence, as well as chromosomal translocations [6]. Chemically induced or exogenous methylation occurs as a result of exposure to chemical agents such as nitrosamines, di-methyl sulfate, and 1,3-bis(2-chloroethyl)-1-nitrosourea. Recently, attention has been given to the nitrosamines, which are a principle alkaloids found in tobacco smoke (they make methylation base pairs) [7]. However, partly due to its influence on hydrogen bonding, methylation is the most pro-mutagenic methyl adducts formed and can both silence gene expression and cause point mutations [8]. Epigenetic methylation occurs at the guanine and cytosine of CpG islands in DNA and is regulated by an organism's methyltransferases and other enzymes. These enzymes interact with DNA by flipping the target base out of the double helix and into its active site [9]. The term base flipping is commonly used to describe the rotation of single base out of the double helix as a result of attractive and repulsive forces imparted by enzyme's active site constituents.

The aim of this theoretical investigation is to use ab initio approaches [10] to characterize the nature of changes in the interaction energy and the molecular structure in A:T base pairs under the applied external electric field. To accomplish this, we analyzed the

changes in the molecular geometry and the interaction energy components [11].

2. COMPUTATIONAL DETAILS

Theoretical calculations are used to bridge gaps in the understanding of experimental results. In many cases the results of the experimental methods are unable to describe accurately the small complex components. The molecular quantum methods can be used to investigate properties beyond the scope of the crystallographic methods. Where they allow to study the physical and chemical properties, which are not easily measured systems in the micro and nano dimensions. Also they can examine the interaction energies that are not provided by the X-ray and NMR experiments. The predictive power of the theoretical computational methods for DNA has been confirmed in the recent investigation of experiments, which concluded that the amino groups in the cytosine and the adenine are non-planar form [12]. This was postulated and predicted by the ab initio calculations over 10 years ago [13]. First geometries for all cases were optimized at Restricted Hartree-Fock (RHF) method with basis set 6-31G(d, p) and then optimized using B3LYP method to include correlation corrections with basis set 6-31G(d,p). Density functional are used, the Becke's three-parameter hybrid functional using the LYP correlation functional which defines the exchange functional as the linear combination of Hartree-Fock, local and gradient-corrected exchange terms. The B3 hybrid functional was used in combination with the correlation functionals of Lee, Yang and Parr and non-local correlation expression provided by the LYP [14]. Some previous calculations [15-17] suggested that the B3LYP/6-31 G(d,p) results gave good agreement. All geometries for each case were performed using the Gaussian98 [18]. To examine the effect of applied electric field on the adenine, thymine, the A:T base pair and the hydrogen bonding between A:T base pair, the electric field were varied from 0.00 au to 0.002 au in step 0.0005 au. The external electric fields have been applied in x , y and z direction respectively.

3. RESULTS AND DISCUSSION

3.1 STABILITY OF THE ADENINE, THYMINE AND THE SINGLE A:T BASE PAIRS

The geometry optimized without electric field of the adenine, thymine and the single A:T base pair using

B3LYP level are shown in figure 1. The change in optimized total energies ($\Delta E_t = E_t(\text{field-off}) - E_t(\text{field-on})$) of the adenine, thymine and the single A:T base pairs as a function of the considered applied electric field in this study are collected in figures 2,3 and 4, respectively. The minimize energy calculation for the adenine, thymine and the A:T base pair (in gas phase) appeared changes in their stabilities. As the electric field increases in the x and y direction respectively the adenine stability increases with note that x direction shown more effected. While the applied electric field in the z direction, which is perpendicular to the plane of the adenine molecule, shows very low effect compared with the x and y directions, see figure 2. In figure 3 shown the effect of applied electric field on the thymine, where the y direction shows more increases in the stability of thymine compare with the case of adenine. Also the applied electric field in x

direction shows more effect than the y direction, see figure 3. The results of applied electric field in the z direction for thymine appear to be the same as for the adenine. When the electric field was applied in the x direction, which is parallel to the two hydrogen bonds between the adenine and thymine in base pair, the stability of the single A:T base pair increases as the electric field increases, see figure 4. While the applied electric fields in the y direction shows the increase in the stability of the A:T base pair. The applied electric field in the z direction to the A:T base pair, which is perpendicular to the plane of A:T base pair, does not show interested effect on the its stability compared with the x and y directions. For that, the enzyme of helicase, which unwinding DNA, will response hardly in the operation of separating the double helix of DNA due to applied electric field in the x or y directions.

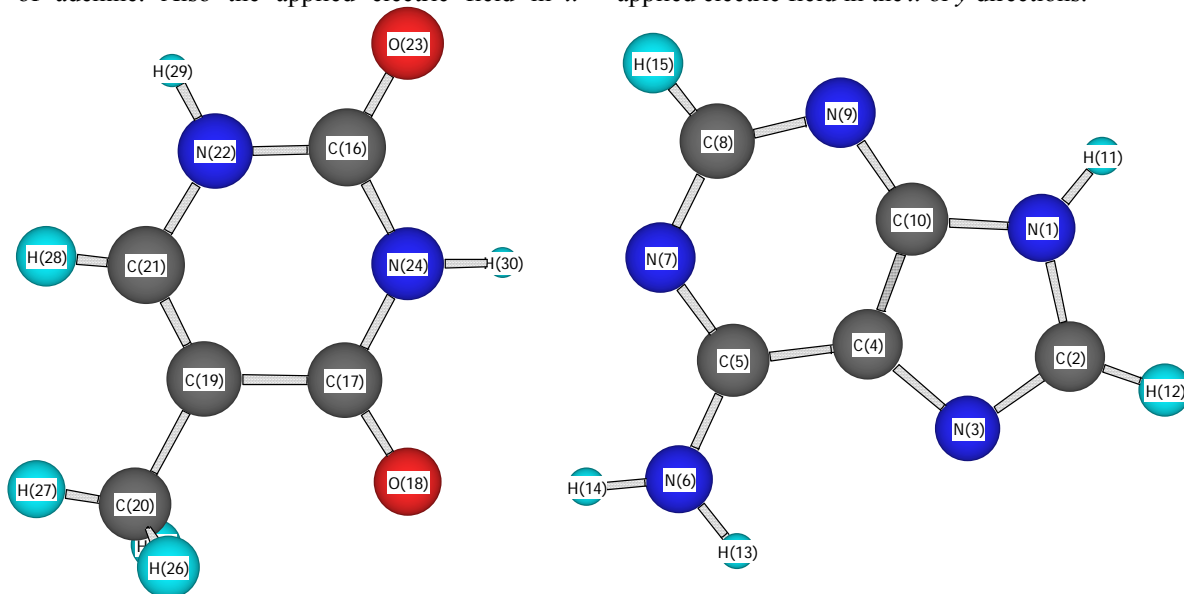


Fig.1. The optimized normal A:T base pair at B3LYP/6-31G(d,p) level.

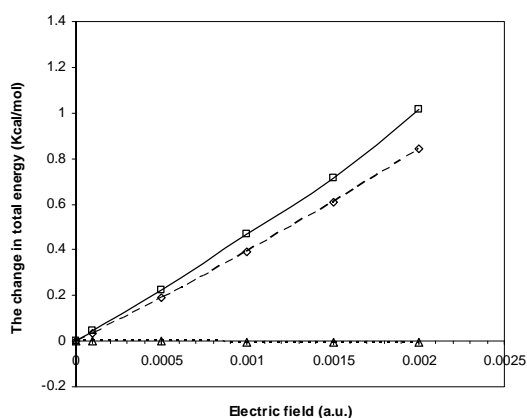


Fig.2. The change in total energies of adenine as a function of the electric field in x: \square , y: \diamond and z: \triangle direction respectively at B3LYP/6-31G(d,p) level.

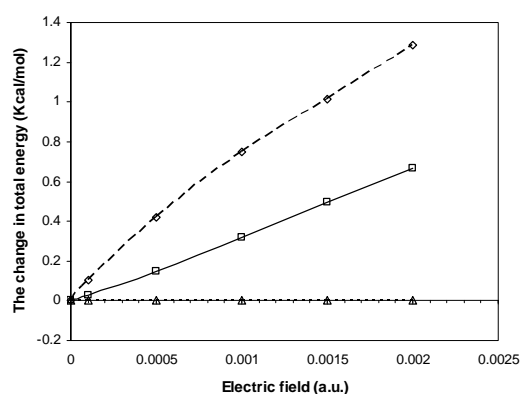


Fig.3. The change in total energies (in Kcal/mol) of thymine as a function of the electric field in x: \square , y: \diamond and z: \triangle direction respectively at B3LYP/6-31G(d,p) level.

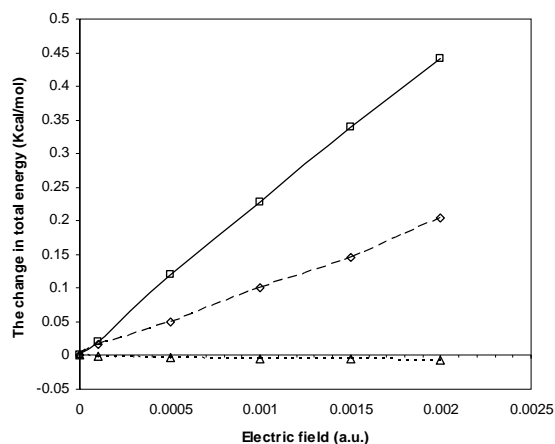


Fig.4. The change in total energies (in Kcal/mol) of A:T base pairs as a function of the electric field in x: □, y: ◇ and z:△ direction respectively at B3LYP/6-31G(d,p) level.

3.2 NATURE OF HYDROGEN BONDING ENERGY OF THE A:T BASE PAIRS

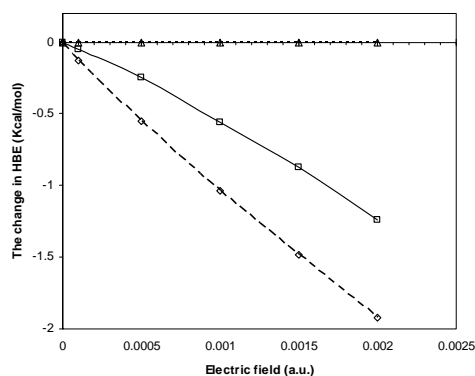


Fig.5. The change in hydrogen bonding energies of A:T base pairs as a function of the electric field in x: □, y: ◇ and z:△ direction respectively at B3LYP/6-31G(d,p) level.

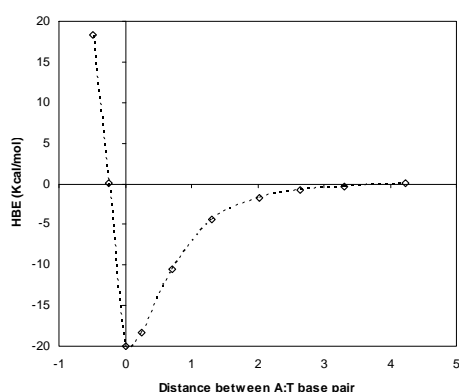


Fig.6. The hydrogen bonding energy as a function of the change in the distance (in Å) between the A:T base pair at B3LYP/6-31G(d,p) level.

The less computationally expensive for the B3LYP/6-31G (d,p) method, which describes hydrogen bonding interactions in A:T and G:C base pairs, was in good agreement with higher-level MP2 calculations

[15,16]. In order to examine the nature of hydrogen binding between the adenine and the thymine which form the A:T base pair, we adopted only a single A:T base pair in this work. The optimized of the single A:T base pairs, without electric field, which considered in this study are shown in figure 1. The hydrogen bonding energy (HBE) in the A:T base pair, $HBE = E_{A:T} - (E_{Adenine} + E_{Thymine})$, and the change in hydrogen bonding energy, $\Delta HBE = HBE(\text{field-off}) - HBE(\text{field-on})$, as a function of applied electric field shows in figure 5. Where the applied field in the y direction is shown more lower in the hydrogen bonding energy compare with the effect of applied electric field in x direction. The applied electric field in the z direction, which is perpendicular to the plane of the two hydrogen bonds in the A:T base pair, is shown significantly different from the other two directions. It shows little decreasing in the hydrogen bonding energy and then few increasing due to field increasing. According to this result, when the electric field applied in the x or y direction may be not difficult the role of enzyme to separate the DNA sheets, which lead to be easy in the processing of the DNA copy. In general we hypothesize that the genes at the electric field may be not silenced as in the case of G:C base pair [17], because of the ability of bases to flip out of the double helix into the active site of enzymes due to the relative lower in the hydrogen binding interactions under electric field. In order to more explore the nature of the two hydrogen bonding lengths without an applied electric field, we calculate the hydrogen bonding energy as a function of the distance between the adenine and thymine in the A:T base pair using B3LYP/6-31G(d,p), see figure 6. Whereby the distance between the adenine and thymine in the A:T base pair increase from the optimized distance, or equilibrium point, the hydrogen bonding energy shows repaid decreases beyond few angstroms, and with 3Å distance from the equilibrium point the hydrogen bonding energy finish, approximately. Also if the adenine and thymine as base pair closed once from another, then the hydrogen bonding energy exchanges into the repulsion item. The energy equal to 0.798eV enough to dispersion the hydrogen bonding energy in the A:T base pair so that each one from the adenine and thymine in the A:T base pair will be alone. To examine the nature of flexibility the two hydrogen bonds by doing rotation between the adenine and thymine in the A:T base pair with step 10°, see figure 7, using B3LYP/6-31G(d,p). It shows that the hydrogen bonding energy at the rotation angle equal to 10° will dropped to 10.9%, while at 20° the hydrogen bonding energy will dropped to 18.8%. This may be giving theoretical investigation about the limited of the rotation flexibility in arrangement 20±10°. Also, the enzyme of helicase may be need to rotating the two hydrogen bonds in the A:T base pair by angle 20±10° to flip it out of the double helix.

3.3 GEOMETRY ANALYSIS OF THE A:T BASE PAIRS

The change in the optimized of the two hydrogen bonds lengths between the adenine and thymine in A:T base pair, $\Delta r = r(\text{field-off}) - r(\text{field-on})$, is shown in figures 8 and 9 respectively. Calculations using B3LYP/6-

31G(d,p) are made on the A:T base pair in order to see the effect of the electric field on lengths of these two hydrogen bonds between the adenine and thymine in base pair. The applied electric field in x and y directions respectively, produce compression of the hydrogen bond length $\Delta r(\text{H30-N7})$ as the electric field increase. Note that the effect of the field on the bond in x direction is more than the y direction. The applied electric field in z direction, which is perpendicular to the plane of A:T base pair, shown uninterested effect on the hydrogen bond lengths, see figure 8. The electric field effects on the hydrogen bond length, $\Delta r(\text{H14-O18})$, shown behavior, approximately, opposite to the case of $\Delta r(\text{H30-N7})$ under the electric field, see figure 9. Where the electric field extensions the $\Delta r(\text{H14-O18})$ length. At electric field in x and y directions respectively shown effects differ on the A:T base pair comparison with the case without electric field, in two ways: first, the change of the hydrogen bond length between adenine (H14) and thymine (O18) atoms, extension. Second, there is an closing of the hydrogen bond length between adenine (N7) and thymine (H30) atoms more than the normal case. This indicates an closing of the hydrogen bond at the middle site of the pair and opening at the down site. In other words, the aberrant A:T base pair under the electric field at (O18) atom, the electric field acts on the hydrogen bond so that it causing to lose its ability to participate in one of two hydrogen bonds, leaving it susceptible to mis-pairing with bases pair, which untypical for two hydrogen bonds such as A:T base pair. The effect of the electric field give the same results to that of mutagenic by methylate effect on the A:T base pair [15,16]. From the geometrical data it should be noted that the geometrical factors of all the electric fields effects differ significantly from each other with respect to intermolecular bond lengths. The effect of the electric field on the hydrogen bond lengths is excessive when the external electric field is applied perturbs in the same directions of the plane of A:T base pair. In other words, the applied high electric field in the direction that coincident with molecule of A:T pair is significant enough to disrupt one of the two hydrogen bonds in the A:T base pair. The molecule of adenine and thymine of the A:T base pair still in the same plane of the normal A:T base pair under all fields.

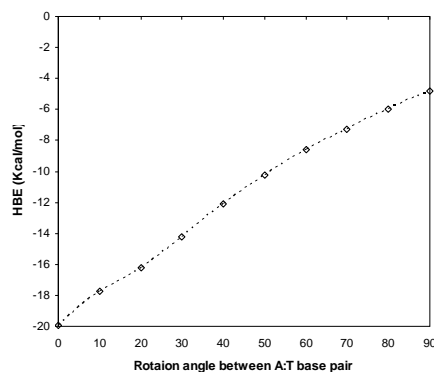


Fig.7. The hydrogen bonding energy as a function of the rotation angle (in degree) between the A:T base pair at B3LYP/6-31G(d,p) level.

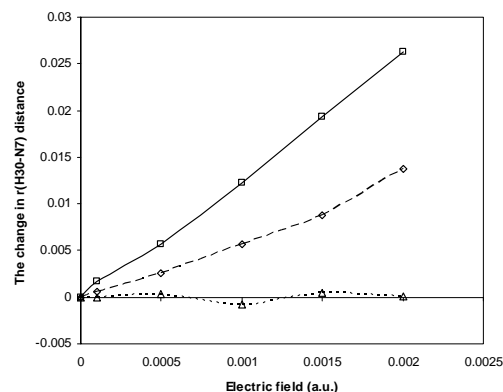


Fig. 8. The change in the hydrogen bond distance (\AA), Δr , as a function of the electric field in x : \square , y : \diamond and z : Δ direction respectively at B3LYP/6-31G(d,p) level.

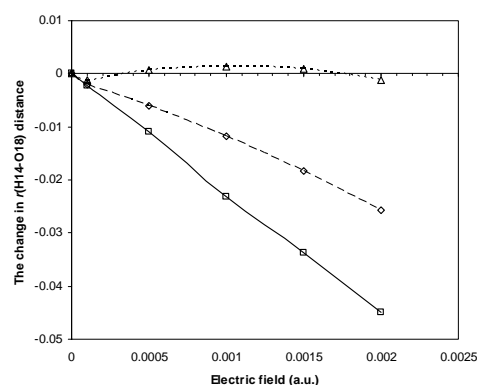


Fig. 9. The change in the hydrogen bond distance (\AA), Δr , as a function of the electric field in x : \square , y : \diamond and z : Δ direction respectively at B3LYP/6-31G(d,p) level.

4. CONCLUSION

In summary, the results of our calculations show that the applied electric field on A:T base pairs causes significant changes in the interaction between adenine and thymine compared to the Watson-Crick hydrogen-bonding pattern. This probably is a result of inductive and steric effects. As a result of changes in the A:T hydrogen bonding energies, the energy required for base flipping may not exceed to that which is provided by the enzyme which is responsible for this process. Our results are summed up by the following:

- Based on our data, the increases in the electric field may be introducing significant changes in the geometrical parameters of the A:T base pairs. In the case of $\Delta r(\text{H14-O18})$, which is known to cause base transitions, it is shown that one of the hydrogen bonds is lost.
- We have found that changes in interaction energies in the A:T base pairs (with applied electric field) do directly correlate to adduct pro-mutagenicity.
- Additionally, our data reveals that electrostatic contributions predominate in interactions of all investigated complexes.
- The order of stability of adenine, thymine and the A:T base pair is a function of electric field intensity and direction.

- The applied high electric field on the A:T base pair decreasing intermolecular bonding energies.
- The electric field may be able to produce the multi-point mutations.
- The range of the hydrogen bonding energy in the A:T base pair was lower than the optimized distance by $\sim 0.24 \text{ \AA}$ and higher than by $\sim 3 \text{ \AA}$ approximately.
- The rotation flexibility in the A:T base pair was limited as $20^\circ \pm 10^\circ$ approximately.
- Finally, some results of applied external electric field on the A:T base pair same to the results of C:G base pair and other differ [18].

-
- [1] *J. Watson and F. Crick*. Nature, 171, 1953, 737.
 - [2] *T. Douki, A. Reynaud-Angelin, J. Cadet and E. Sage*. Biochemistry, 42, 2003, 9221.
 - [3] *J. Cadet, T. Delatour, T. Douki, D. Gasparutto, J. Pouget, J. Ravanat and S. Sauvaigo*. Mutat. Res., 424, 1999, 9.
 - [4] *M. Shigenaga, C. Gimeno and B. Ames*. Proc. Natl. Acad. Sci. USA, 86, 1989, 9697.
 - [5] *R. Cathcart, E. Schwieters, R. Saul and B. Ames*. Proc. Natl. Acad. Sci. USA, 81, 1984, 5633.
 - [6] *K. Valerie and L. Povirk*. Oncogene, 22, 2003, 5792.
 - [7] *S. Hecht*. Chem. Res. Toxicol., 11, 1998, 560.
 - [8] *B. Singer and D. Grunberger*. Molecular Biology of Mutagens and Carcinogens, (Plenum Press, New York 1983).
 - [9] *R. Roberts*. Cell, 82, 1995, 9.
 - [10] *J. Sponer, J. Leszczynski and P. Hobza*. J. Phys. Chem., 100, 1996, 1965.
 - [11] *W. Sokalski, S. Roszak and K. Pecul*. Chem. Phys. Lett., 153, 1988, 153.
 - [12] *F. Dong and R. Miller*. Science, 298, 2002, 1227.
 - [13] *J. Leszczynski*. Int. J. Quantum. Chem., Quantum Biol. Symp., 19, 1992, 43.
 - [14] *R. Ditchfield, W. J. Hehre and J. A. Pople*. J. Chem. Phys., 54, 1971, 724.
 - [15] *G. Forde, A. Flood, L. Salter, G. Hill, L. Gorb and J. Leszczynski*. J. Bio. Struc. Dynam., 20, 2003, 811.
 - [16] *A. Flood, G. Forde, L. Salter, G. Hill, L. Gorb and J. Leszczynski*. J. Bio. Struc. Dynam., 21, 2003, 297.
 - [17] *M. J. Al-anber, Z. S. Abdalla and A. A. Salih*. Fizika, 17, 2008, 151.
 - [18] *M. J. Frisch, G. W. Trucks, H. B. Schlegel, G. E. Scuseria, M. A. Robb, J. R. Cheeseman, V. G. Zakrzewski, J. A. Montgomery, Jr., R. E. Stratmann, J. C. Burant, S. Dapprich, J. M. Millam, A. D. Daniels, K. N. Kudin, M. C. Strain, O. Farkas, J. Tomasi, V. Barone, M. Cossi, R. Cammi, B. Mennucci, C. Pomelli, C. Adamo, S. Clifford, J. Ochterski, G. A. Petersson, P. Y. Ayala, Q. Cui, K. Morokuma, N. Rega, P. Salvador, J. J. Dannenberg, D. K. Malick, A. D. Rabuck, K. Raghavachari, J. B. Foresman, J. Cioslowski, J. V. Ortiz, A. G. Baboul, B. B. Stefanov, G. Liu, A. Liashenko, P. Piskorz, I. Komaromi, R. Gomperts, R. L. Martin, D. J. Fox, T. Keith, M. A. Al-Laham, C. Y. Peng, A. Nanayakkara, M. Challacombe, P. M. W. Gill, B. Johnson, W. Chen, M. W. Wong, J. L. Andres, C. Gonzalez, M. Head-Gordon, E. S. Replogle, and J. A. Pople*. Gaussian. Inc., Pittsburgh PA, 1998.

Received: 20.06.2011

CALCULATION THE DIFFERENTIAL CROSS SECTION OF $d\mu + T_2$ IN MUON CATALYZED FUSION WITH USING OF MORSE POTENTIAL

HEYDAR IZADNESHAN

Department of Physics , Marvdasht Branch , Islamic Azad University, Marvdasht , Iran

izadneshan@gmail.com

We present results for calculating the differential and total cross section of elastic $d\mu + T_2$ with using of morse potential. The calculations are performed in the framework of the adiabatic representation of the three-body problem. This is done by calculating the excitation, ionization, and charge-transfer cross sections for the this collision and scaling the results. The spin-flip processes of the muonic atoms are also considered. The differential and total cross section calculated for centre-of-mass collision energies $\varepsilon \leq 30 \text{ eV}$, are needed for a correct description of many experiments in Muon catalyzed fusion and cold fusion physics.

1. INTRODUCTION

A scattering cross section into which particles are scattered during the collision with the force field of another particle was first developed by Ernest Rutherford. The idea behind the scattering cross section is that a mathematical relationship can be derived which will relate the probability that particles will be scattered into a given angle[1]. In the absence of dissipative forces the total energy of the system must also be conserved:

$$E = T + U = \text{constant} \quad (1)$$

and

$$E = \frac{1}{2} \mu (\dot{r}^2 + r^2 \dot{\theta}^2) + U(r) \quad (2)$$

where

$$\psi_{sc} = f(\theta) \frac{e^{ikr}}{r}, \quad (3)$$

And cross section with harmonic potential defined as [2]:

$$\sigma(\psi) = \sigma(\theta) \cdot \frac{\left[x \cos \psi + \sqrt{1 - x^2 \sin^2 \psi} \right]^2}{\sqrt{1 - x^2 \sin^2 \psi}} \quad (4)$$

The Morse potential, named after physicist Philip M. Morse, is a convenient model for the potential energy of a diatomic molecule in a given electronic state. It is a better approximation for the vibrational structure of a molecule than the quantum harmonic oscillator. The Morse

potential may be described by many equivalent or nearly equivalent forms[2]. We shall explicitly use the form :

$$V(r) = D_e \left[1 - e^{-a(r-r_0)} \right]^2 \quad (5)$$

Where D_e is the depth of the well, r_0 is the equilibrium separation, and a is an additional parameter related to the strength of the bond. Notice the brackets [] are squared. Note that $(r-r_0)$ corresponds to the displacement from the equilibrium separation fig (1).

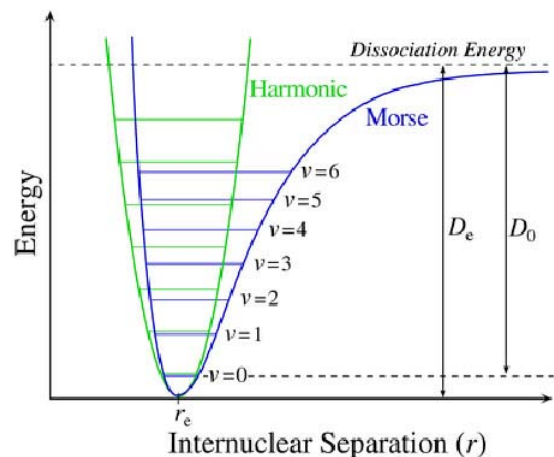


Fig. 1: Morse potential versus harmonic potential.

From math, we know that any reasonable function can be expanded in a Taylor series about a point (in this case the equilibrium separation):

$$f(r) = \sum_0 \frac{1}{n!} \left. \frac{\partial^n f}{\partial r^n} \right|_{r_0} (r - r_0)^n = f(r_0) + \left. \frac{\partial f}{\partial r} \right|_{r_0} (r - r_0) + \frac{1}{2} \left. \frac{\partial^2 f}{\partial r^2} \right|_{r_0} (r - r_0)^2 + \dots \quad (6)$$

where expressions for the 0th , 1st, and 2nd order terms have been written out and we can expand the Morse potential in Taylor series too.

A Muonic hydrogen atom $d\mu$ can be approximately treated as a small neutron-like particle. Therefore, the methods derived for the description of neutron scattering in condensed matter can be applied to $d\mu$ scattering in dense hydrogenic targets. Below, this is adapted to the

calculation of the differential cross sections for $d\mu$ scattering in the hydrogenic crystals[3]. In this formalism, the cross sections are expressed in terms of the response function S , which depends solely on properties of a given target for fixed momentum and energy transfers. A definition of this function involves both quantum-mechanical and statistical averaging over the target states at temperature T . It is assumed that there is no coupling

between the translational and collective motions of the molecules in the condensed target and the molecular rotations and vibrations. The internal molecular degrees of freedom are already included in a single-molecule process [4] and, therefore, do not enter into the response function. It is assumed that a bulk dense target is kept at a sufficiently low pressure, so that distortions of a single bound molecule due to the interactions with neighbors can be neglected. This assumption is fulfilled in the case of low-pressure ($\ll 10$ kbar) solid hydrogenic targets [5,6]. The mean distance between the neighboring molecules in such targets is several times greater than the diameter of these molecules. The Van der Waals force between the molecules is weak. As a result,

the rotational and vibrational numbers remain good quantum numbers, although small broadening of certain excited molecular levels takes place [7]. This broadening is not taken into account in the presented calculations.

Low-pressure hydrogenic solids are quantum molecular crystals, which are characterized by a large amplitude of the zero-point vibrations of the molecules in the lattice. The standard lattice dynamics can be applied to these crystals, after certain renormalization of the molecule-interaction potential [5,6]. Also, the Debye model of a solid can be used as a reasonable approximation. The wavelength of a very slow (~ 10 meV) muonic hydrogen atom is comparable to the nearest-molecule distance of about 3.5 \AA [5,6]. Therefore, strong interference effects can be observed at such energies. These effects are described using a conventional separation of 3 the total differential cross sections on the incoherent and coherent fractions.

2- METHOD

The coherent scattering takes place only if specific geometrical conditions are fulfilled. Analogous to the neutron coherent scattering [8], the coherent cross section for $a\mu$ scattering in a solid single-isotope hydrogenic target can be written down in the form:

$$\left(\frac{\partial^2 \sigma}{\partial \Omega \partial \varepsilon'} \right)_{coh} = N_{mol} \frac{k'}{k} \sigma_{coh} S(k, \omega) \quad (7)$$

Where N_{mol} is the number of molecules in the target. The energy transfer ω and the momentum transfer K to the lattice are, respectively, equal to

$$\omega = \varepsilon - \varepsilon' - \Delta E \quad \kappa = K - K' \quad (8)$$

where ε and ε' denote the initial and final kinetic energies of the scattered muonic atom and ΔE is the sum of the internal-energy changes of $a\mu$ and of the target molecules. Vectors k and k' stand for the initial and final momenta of $a\mu$. These momenta and collision energies are connected by the relations

$$\varepsilon = \frac{1}{2} \kappa^2 / Ma\mu \quad \text{and} \quad \varepsilon' = \frac{1}{2} \kappa'^2 / Ma\mu \quad (9)$$

in which $Ma\mu$ denotes the $a\mu$ mass. The function σ_{coh} in Eq. (7) is expressed by the amplitude F_{mol} for $d\mu$ scattering from an isolated molecule [9]

$$\sigma_{coh} = \left| \overline{F_{mol}} \right|^2 \quad (10)$$

The horizontal bar stands here for averaging over a random distribution of the total spin J of the $d\mu$ -molecule system and over a distribution of the initial rotational states of the molecules. It is assumed that there is no correlation between the direction of the molecular spin I and the lattice site. Incoherent scattering does not include interference effects from different molecules in the lattice. The incoherent cross section takes a general form [8].

Where :

$$\left(\frac{\partial^2 \sigma}{\partial \Omega \partial \varepsilon'} \right)_{inc} = N_{mol} \frac{\kappa'}{\kappa} \sigma_{inc} S_i(\kappa, \omega) \quad (11)$$

$$\sigma_{inc} = \overline{\left| F_{mol} \right|^2} - \left| \overline{F_{mol}} \right|^2 \quad (12)$$

and the incoherent response function $S_i(k, \omega)$ is a fraction of the total response function $S(k, \omega)$. In the limit of large momentum transfers, the coherent processes disappear, so that $S(k, \omega) \approx S_i(k, \omega)$. The total differential cross section $\partial^2 \sigma / \partial \Omega \partial \varepsilon'$ is a sum of the coherent (7) and incoherent (11) cross sections. The inelastic scattering processes which change the internal state of $d\mu$ or that of the target molecule (such as the spin-flip and isotopic-exchange reactions and the rotational-vibrational transitions) are fully incoherent processes. No averaging over the states of the different target molecules is performed and, therefore, in this case σ_{inc} reduces to the single molecule squared amplitude

$$\sigma_{inc} = \left| F_{mol} \right|^2 \quad \text{and} \quad \sigma_{coh} = 0 \quad (13)$$

When the states of the muonic atom and molecule are not changed during collision,

σ_{coh} and σ_{inc} are equal to the coherent and incoherent fractions of the elastic cross section for $a\mu$ scattering from a single molecule. Their values depend on a given choice of the hydrogen isotopes, the total spin F of $d\mu$, the population of the molecular rotational levels, and the collision energy. In particular, when F^{mol} does not depend on the spin J and only one rotational state is populated, the scattering is fully coherent

$$\sigma_{coh} = \left| \overline{F_{mol}} \right|^2 = \overline{\left| F_{mol} \right|^2} \quad \text{and} \quad \sigma_{inc} = 0 \quad (14)$$

For example, such a situation takes place in the case of elastic scattering $d\mu + T_2$ in the ground rotational state

$K=0$ of the T_2 molecule. In general, both σ_{coh} and σ_{inc} can have nonzero values.

At $\varepsilon \leq \text{eV}$, molecular-binding and electron-screening effects are very important [10]. In this energy region (molecular regime), the scattering from hydrogenic molecules is well described by the method presented in Ref. [11], with the use of the harmonic potential for interaction between the molecular nuclei.

At intermediate energies between the molecular and nuclear regimes (crossover region), where the centrifugal distortions and anharmonicities of highly-excited rotational-vibrational states play an important role and dissociation of the molecule during collision is possible, a

better approach is necessary. This has been deduced from the experimental investigation of $d\mu$ atom diffusion and thermalisation in low-pressure T_2 targets [12]. Also, in the case of deep-inelastic neutron scattering from T_2 molecules, discrepancies between the experiment and theory using the harmonic approach have been observed in the crossover region [13].

A solution to this problem is to use a more realistic potential for description of the internuclear interaction in the hydrogenic molecules, e.g., the Morse potential [14]. The differential cross section $d\sigma_{0n}(\varepsilon)/d\Omega$ (without the electronscreening corrections) takes the following form in CMS:

$$\frac{d\sigma_{0n}(\varepsilon)}{d\Omega} = 4 \left(\frac{M}{\mu} \right)^2 \overline{|F_{ff'}(k, k')|^2} \frac{k_n}{k_0} \sum w_{k'/lk} D_{vl}^2(q) \quad (15)$$

in the case of three identical hydrogen-isotope nuclei in the scattering process [11]. In this relation the label $0 \equiv (K, M_k, v=0)$ denotes the set of initial rotational and vibrational quantum numbers. Since temperatures of hydrogenic targets used in experiments do not exceed a few thousands kelvins, it is assumed that the molecule is initially in the ground vibrational state $v=0$. The label $n \equiv (K', M'_k, v')$ stands for the set of final rotational and vibrational numbers, if the molecule is finally in the discrete-energy state. When the dissociation takes place in the collision process, the label $n \equiv (K', M'_k, v')$ represents the final molecular state with the continuous energy E' . The reduced masses for muonic atom scattering from a molecule and from a free nucleus are denoted by M and $d\mu$, respectively. The function $F_{ff'}$, introduced in Ref. [11], is a linear combination of the nuclear scattering amplitudes for fixed values of the initial F and final F' total spin of the muonic atom. Since the symmetric molecule T_2 have definite parities for even and odd rotational numbers, the function $F_{ff'}$ also depends on K and K' . The horizontal bar in Eq. (15) denotes averaging over the total spin of the system and over the initial molecular spin. The quantities K_0 and K_n are the values of initial and final momentum of the atom, respectively, and $q = |K_n - K_0|$ is the value of momentum transfer. The initial ε and final ε' kinetic energies in CMS are expressed in the formulae $\varepsilon = k_0^2 / 2M$ and $\varepsilon' = k_n^2 / 2M$ by the respective

momenta K_0 and kn . The coefficients $w_{k'/lk}$ are defined in Ref. [11]. The molecular form factor D_{vl} in Eq. (2) is given as:

$$D_{vl}(q) = \int_0^\infty u_v(R) j_l(qR/2) u_0(R) dR \quad (16)$$

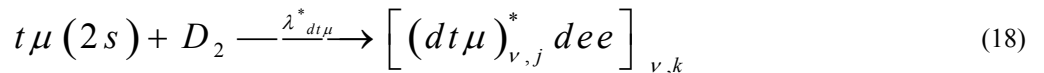
Where u_0 and u_v are the initial and final radial wave functions of the molecule. The l th spherical Bessel function is denoted by j_l . The cross section (15) is averaged over the initial angular momentum projection M_k and summed over the respective final projections M'_k .

3. RESULTS

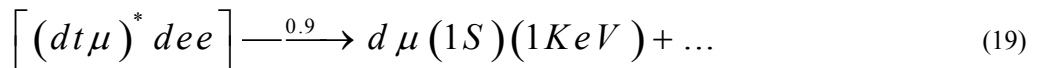
The differential cross sections $d\sigma/d\Omega$ presented below are calculated for fixed values of the initial rotational number K and summed over the final quantum numbers

$$\frac{d\sigma_0}{d\Omega} = \sum_{k', v'} \frac{d\sigma_{0n}}{d\Omega} + \sum_{k'} \int \frac{d\sigma_{0n}}{d\Omega} dE' \quad (17)$$

It is widely accepted that a $dt\mu$ molecule can be regarded as being resonantly formed in a two-body collision between $t\mu$ and $[1]$.



And then:



In this reaction, the collisional energy and the binding energy of $dt\mu$ molecule are absorbed by the rotational and vibrational energy of the $[(dt\mu)dee]$

complex, as shown in relation (18). This resonant formation mechanism has succeeded to explain a high muon cycling rate, which is predominantly determined by

the $d\mu$ formation rate. It was natural that a theoretical calculation based on this mechanism [15], predicted the $d\mu$ formation rate to decrease steeply with decreasing temperature below 100 K, at which the collisional energy did not reach the lowest resonance level. However, this was not consistent with the experimental results [16,17], and even in liquid and solid D-T mixture, high fusion rate was observed. From equation (19) we can see that fusion reaction from $d\mu$ branch is very important.

A role of the discrete or continuous energy spectrum as a function of collision energy ε can be visualized by its contribution to the total cross section σ_0

$$\sigma_0 = \sum_{k',v'} \sigma_{0n} + \sum_{k'} \int \sigma_{0n} dE' \quad (21)$$

which is expressed by the total cross section σ_{0n} for a fixed final state

$$\sigma_{0n} = \int \frac{d\sigma_{0n}}{d\Omega} d\Omega \quad (22)$$

The numerical calculations have been performed for several lowest rotational levels. The analogous differential cross sections for $d\mu$ scattering from the excited deuterium molecule T_2 ($K = 1$) are presented in fig.2. Also Total cross sections for $d\mu$ scattering with morse potential (bold line) versus its total cross section with harmonic potential (dashed line) for scattering the from the excited deuterium molecule T_2 ($K = 1$) are presented in fig. 3. The contributions from discrete and continuous spectra to the cross sections σ_0 for this processes are shown in this figure.[18]

4- CONCLUSION

We have considered the problem of highly accurate calculations of bound states in the three-body muonic molecular $[(d\mu)dee]$ complex. Note that all muonic molecular ions can easily be created in real experiments and their various properties can be measured quite accurately. From a certain point of view, theoretical and experimental study of these ions is more interesting and informative than the traditional analysis of atomic three-

body systems. Cross section of the formation of mesic molecular complex in the reactions $d\mu(F=0) + T_2(K=0) \rightarrow d\mu(F'=0) + T_2$ is calculated at low energies ($E < 30$ eV). We assume the Morse potential energy dependence of the cross section. Accounting for the Morse potential modifies considerably both the energy dependence and the value of the Muonic Molecule Complex formation cross section. From fig (3) and (4) we can see that cross section of $d\mu + T_2$ is greater than $d\mu + D_2$ reaction, that's according to relations (18) and (19).

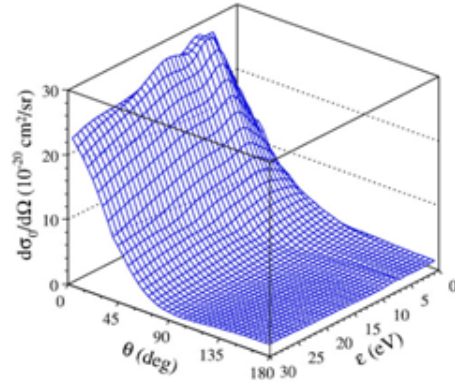


Fig. 2. Differential cross section for the scattering $d\mu(F=0) + T_2(K=0) \rightarrow d\mu(F'=0) + T_2$ versus scattering angle θ and collision energy ε .

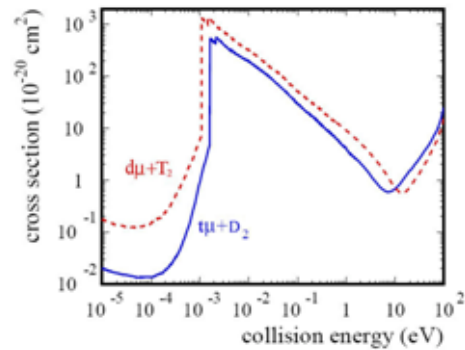


Fig. 3. Total cross sections for $d\mu + T_2$ scattering with morse potential in compare with total cross section $t\mu + D_2$ reaction

- [1] Chow, Tai L., California State University, Stanislaus, Classical Mechanics, John Wiley & Sons, Inc. pg. 336-341, 216-218.
- [2] H. Taseli, J. Phys. A: Math. Gen. 31, 1998, 779-788.
- [3] L. Van Hove, Phys. Rev. 95, 249, 1954.
- [4] A. Adamczak, Phys. Rev. A 74, 042718, 2006.
- [5] P. C. Souers, Hydrogen Properties for Fusion Energy University of California Press, Berkeley, 1986.
- [6] F. Silvera, Rev. Mod. Phys. 52, 393, 1980, and references therein.
- [7] J. Van Kranendonk, Solid Hydrogen (Plenum Press, New York and London, 1983).
- [8] S. W. Lovesey, Theory of Neutron Scattering from Condensed Matter, Clarendon Press, Oxford, 1984.
- [9] R. Pohl et al., Phys. Rev. Lett. 97, 193402, 2006.
- [10] F. Kottmann, W. Amir, F. Biraben, et al., Hyperfine Interact. 138, 2001, 55.
- [11] A. Adamczak, Phys. Rev. A 74, 2006, 042718.
- [12] S.S. Gershtein, Zh. Eksp. Teor. Fiz. 34, 1958, 463, Sov. Phys. JETP 7, 1958, 318.
- [13] S.S. Gershtein, Zh. Eksp. Teor. Fiz. 40, 1961, 698, Sov. Phys. JETP 13, 1961, 488.
- [14] R. Pohl, Ph.D. thesis, ETH, Zurich, 2001.
- [15] M.R. Eskandari et al., Nucl. Sci. J., 38, 4, 219-229, 2001.
- [16] M.R. Eskandari, S.N. Hosseini, B. Rezaie, Can. J. of Phys., 80, 1099-1114, 2002.

CONTENTS

1.	Solution of generalization of principal chiral field problem M.A. Mukhtarov	3
2.	Vibrational frequencies and structural investigation of $[M(CN)_4]^{2-}$ (M = Cd, Hg and Zn) ions Gürkan Keşan, Cemal Parlak, Tomáš Polívka, Mustafa Şenyel	7
3.	ZnO nanorods by simplified spray pyrolysis Serdar Aydın, Güven Turgut, Mehmet Yilmaz and Mehmet Ertuğrul	14
4.	Nuclear transparency effect in the strongly interacting matter M. Ajaz, M.K. Suleymanov, O.B. Abidinov, Ali Zaman, K.H. Khan, Z. Wazir, Sh. Khalilova	17
5.	On super-high resolution spectroscopy of metastable atoms in ultra-thin gas cells A.Ch. Izmailov, Ch.O. Qajar, R.A. Karamaliyev	21
6.	Life time of polaron excited state in single-shell nanotube O.Z. Alekperov, S.M. Seid-Rzayeva, S.S. Guseynova	27
7.	The influence of Ge atoms on thin film $TlGaS_2(Se_2, Te_2)$ formation E.Sh. Alekperov	31
8.	Optical properties of $MnGa_2Se_4$ in the region of self-absorption edge B.G. Tagiyev, T.G. Kerimova, O.B. Tagiyev, I.A. Mamedova, S.G. Asadullayeva	35
9.	The role of eigen components at energy spectrum in Ag_2Te F.F. Aliyev, A.A. Saddinova, R.A. Gasanova, N.A. Verdiyeva	37
10.	Theoretical ab initio study the hydrogen bonding nature of the A:T base pair Mohanned Jasem Al-Anber	40
11.	Calculation the differential cross section of $d\mu + T_2$ in muon catalyzed fusion with using of morse potential Heydar Izadneshan	45



www.physics.gov.az